SEMI-INCLUSIVE PRODUCTION OF LIGHT MESONS BY HIGH ENERGY PHOTOPRODUCTION

A Dissertation
Presented for the
Doctor of Philosophy
Degree
The University of Tennessee, Knoxville

By
Gavin R. Blackett
May 1993

AA 60357

Dedication

This work is dedicated to the memory of my father
Frank Elliott Blackett
who was fond of saying *"Don't let the bastards get you down."*
Well sir, to the best of my abilities, I have not.

Acknowledgements

As with any large science project, this work could not have been completed without the help of several people. The E687 Collaboration as a whole deserves recognition, though only a few people are mentioned here. Joel Butler, the collaboration's spokesperson, worked diligently during the data taking phase to ensure the experiment was run properly. Joel and Paul LeBrun initiated the data reduction scheme, which was taken over by Gary Grim and Luca Cinquini and finished off by fellow Pass1-ers: Rodney Greene, Matt Nehring, Barbara Caccianiga, Murali Pisharody and Joe Swiatek. Jim Wiss and Ray Culbertson provided much of the ground work for the Monte Carlo simulation and tracking, and John Luigi Boca helped in the vector meson aspect of the simulations. John Cumalat, Will Johns, Carlo Dallapiccola, Peter Garbincius, Zeyuan Wu and Brian O'Reilly were instrumental in helping to understand the detector.

I wish to thank Bill Bugg for providing a research position and funding under DOE contract DE-AS05-76ERO3956, even after changing thesis advisors and research topics. George Condo has provided important and stimulating conversations over a broad range of material, and has been both a friend and advisor. It is also refreshing to find a person of similar social and economic views in a university environment. To him I am forever indebted. Thomas Handler has provided perhaps the most important of all contributions: he was responsible for UT joining the E687 Collaboration. Without his efforts, this dissertation would not exist. I also wish to thank Jess Poore for being a member of my committee, though computer science may be more of an application than an actual part of my research.

Much of the computing for this dissertation, as well as the LaTeX used for this thesis, has come either from the computing division at Fermilab, or from the University of Tennessee Computing Center. Most of the final analysis was run on a Silicon Graphics 4D/240GTX Power Station operated by the High Energy Physics group at the University of Tennessee. The Physics Analysis Workstation (PAW) environment from CERN was instrumental in this analysis. All fitting was done with MINUIT (included in PAW) and supplemented with a fitting package from the High Energy Group at the University of Tennessee. Finally, the solid model images in this thesis were produced by the author using AutoCad and 3D-Studio.

On a private note, my time at the University of Tennessee could not have been accomplished without tremendous support. I am indebted to my mother Patti for providing financial and emotional support. In spite of several personal tragedies (including living through a major earthquake and the loss of her home to the 1991 Oakland fire) she has managed to find the resources to help me finish. She is a remarkable woman. I also wish to thank my Aunt Dolores and Uncle Ellis who more or less adopted me as their own. My brother Brent helped to initiate me to the world of computers and computer graphics while my sister Laurel helped me to keep a balanced perspective on life. I wish to thank John and Pamela Foster for allowing me to vent frustrations and for encouragement throughout my life as a graduate student – I hope my godson Jack will be as good a man as his father. I also wish to thank Joseph Dellwo who has had to deal with my many idiosyncrasies perhaps more than anyone else since I became a graduate student.

Finally, to Kathy, I want to express my extreme gratitude for everything you have done, from reading through countless "rough" drafts to taking care of the dog while I was busy pursuing some triviality. Hopefully, as we proceed with our lives, we can put this dismal time behind us (at least until you start your dissertation!). I doubt I have been very caring during this time, and I want you to know I love you very much...

Abstract

Photoproduction experiments have been an effective and efficient method for examining vector mesons. FERMILAB provided to E687 a high energy bremsstrahlung photon beam in order to perform this experiment. The primary purpose of E687 was to study charm quarks, principally through D mesons. The amount of non-charm production greatly exceeded that of charm (roughly 10^{-4} charm events per event). The 500 million triggered events written to tape by the detector provide an ample source of data to investigate photoproduced light quark mesons.

The purpose of this work is to study the following production reactions:

$$\begin{aligned} \gamma N &\rightarrow \pi^+ \pi^- N' \\ \gamma N &\rightarrow K^+ K^- N' \\ \gamma N &\rightarrow \pi^+ \pi^- \pi^\pm N' \end{aligned}$$

where N and N' are nucleons appropriate for charge conservation.

The semi-inclusive dipion channel shows the skewed structure of a photoproduced $\rho(770)$. Evidence is also found for the dipion decay of the $\rho'(1600)$. The K^+K^- channel is used to verify the expected ratio of $\rho(770)/\phi(1020)$ production. The data also show a $J/\psi(3097)$ (presumably through $J/\psi(3097) \rightarrow \mu^+\mu^-$). The light mesons found in these channels follow previous lower energy results. The charge exchange processes containing three pions in the final state are examined for their resonant substructure. The neutral dipion spectrum shows a $\rho(770)$, $f_2(1270)$ and a $\rho_3(1690)$. Evidence is found for the production of the $a_2(1320)$ and the $a_3(2050)$. In addition, this channel presents the possibility of an isovector meson with a mass of $\sim$ 3600 MeV, decaying via $J/\psi(3097)\pi^\pm$.

Contents

1 Introduction to High Energy Physics 1

2 Meson Production 4

2.1 The Vector Dominance Model (VDM) 4

2.2 Charge Exchange Scattering Versus Double Regge Processes 13

2.3 The Kinematics for Experimental Analysis 14

3 Experimental Setup of E-687 17

3.1 Fermilab Supplied Beams 18

3.2 The Target 22

3.3 Detector 23

3.4 Triggers 37

3.5 Data Acquisition 39

4 Data Analysis 46

4.1 The Beam and Its Characteristics 46

4.2 Mass Errors 49

4.3 Final Sample Selection 50

4.4 The $\pi^+\pi^-$ Channel 52

4.5 The K^+K^- Channel 59

4.6 The $\mu^+\mu^-$ Distribution 62

4.7 The $\pi^+\pi^-\pi^\pm$ Channel 65

5 Monte Carlo and Detector Simulation 80
5.1 The ROGUE Monte Carlo 80
5.2 ROGUE Results 83

6 Yields and Cross-Sections 90

7 Concluding Remarks 94

Bibliography 96

Vita 103

List of Tables

1 The naming convention for the light mesons based upon quark content and observable quantum numbers. These states have no admixture of u or d with strangeness or other heavy flavors. The J of the mesons are generally included as a subscript, as with the $f_2(1270)$ or $\rho_3(1690)$. 2

2 Previous experimental results for the cross-section of various vector mesons at different interaction energies. 9

3 Silicon Strip Detector Parameters. 27

4 PWC configuration parameters. Note: P4 wires have an x separation of 2 mm , while y and U have 3 mm separations. 31

5 Čerenkov Particle Identification Information for reconstructed data. 32

6 The various cuts used for the event selection. The table lists the number of events in the 1990 and 1991 data runs. 43

7 Final data sample of skimmed events (the final entry of the previous Table) for the $\rho(770)$, $\phi(1020)$, $\rho'(1600)$ and the $a_2(1320)$, $a_3(2050)$ samples. 43

8 Final cuts for the data sample. 52

9 Fit results for the $\rho(770)$. The lower table only shows the values of the acceptance corrected data. 55

10 Fit values for the $\phi(1020)$. 59

11 Fit values for $J/\psi(3097) \rightarrow \mu^+\mu^-$. 65

12 Fit parameters for the $a_2^{\pm}(1320)$ without the $t'_{\gamma;3\pi}$ requirement. . . 70

13 Fit results for the dipion spectrum of the $\pi^+\pi^-\pi^\pm$ channel. The upper table is for the fit without a t' restriction while the lower is for the data surviving a $0.015 \leq t'_{\gamma;3\pi} \leq 0.2$ GeV^2 requirement. . . 70

14 Fit results for the $\rho(770)\pi^\pm$ spectrum for all events and for those for which satisfy $0.015 \leq t'_{\gamma;3\pi} \leq 0.2$ GeV^2. 72

15 Fit results for the $\rho_3(1690)\pi^\pm$ spectrum before (upper) and after (lower) the $t'_{\gamma;3\pi}$ cut. 76

16 Acceptance corrected yields and cross-sections for various mesons. The upper table lists the yields while the lower shows cross-sections. 92

List of Figures

1 The diagram on the left shows a schematic representation of OZI forbidden transitions while the right represents allowed transitions. 3

2 The (u, d, s) mesons below 2.5 GeV in a Chew-Frautschi plot. The mesons are ordered to show their relative angular momentum L versus their mass squared. 5

3 The Bethe-Heitler dimuon background. 7

4 The variations in cross-sections for the $\rho(770)$ (upper graph) and $\phi(1020)$ (lower graph) for various photon energies. 10

5 (A) The Breit-Wigner Resonance term for $\rho(770) \rightarrow \pi\pi$. (B) The Drell term for the Söding description of the photoproduced $\rho(770)$. 11

6 The effects of the three individual scattering terms which combine to produce the Söding mass shift. The + points represent the Monte Carlo data points. For a comparison to the experimental data, see Chapter 4. 12

7 (A) The direct production process in charge exchange. (B) The double Regge (or double peripheral) production process. 14

8 The helicity angles θ and ϕ for the $\pi^+\pi^-$ decays where $\hat{\pi}$ is chosen as the direction of the π^+ in the dipion rest frame. 16

9 The E687 magnets are shown with a e^+e^- pair traced through the detector. The first magnet opens up the pair in the vertical (bend) direction while the second magnet (run with opposite polarity) closes the trajectories. The H×V hodoscope (not shown) is located at the final focus. 18
10 A plan view of the E687 detector and a 3D view. The target and SSD have been removed in the 3D view for clarity. 19
11 Schematic of Fermilab Beam Lines, and the Wide Band Photon Beam Line (*Not to scale*). 20
12 EGS result showing multiple γ production. 22
13 The Beam Tagging detector planes, located between the two dipoles of the double dog-leg for the electron beam. 24
14 Schematic of the Recoil Electron Shower Hodoscope (RESH). Once a tagged electron passed through the lead radiator, it was swept into the RESH, which registered the hit in one of the ten fingers. 25
15 E687 Target and Silicon Strip Detectors. The first figure shows the orientation of the target and SSD, while the second shows the projection onto the x-y plane (z is coming out of the page). 27
16 Typical SSD multiplicities. These are taken from various runs over the 1990 and 1991 run periods. 28
17 Typical PWC multiplicities. 29
18 PWC Detectors, showing reconstructed tracks. The left shows a 3D view, while the right shows a projection onto the x-y plane (the beam direction, z, is coming out of the page). The solid straight lines in the second figure show the PWC wires of one plane registering hits. The track projections from the figure on the left are also shown in this figure. 31

19 Momentum distribution for different levels of Čerenkov particle identification. This plot shows $\approx$ 50k events of all possible topologies. Refer to Table 4 for a description of ISTATP. 33
20 Schematic of Hadron Calorimeter, showing rings and segmentation of detector. 36
21 First Level (Master Gate) Trigger. 37
22 Event reconstruction using SCMD on FNAL UNIX farms. 41
23 Schematic of the Silicon Graphics (SGI) and IBM 6000 (IBM) farms, indicating the number of nodes on each farm. 41
24 The quantities used to measure the beam energy: A) The energy of the Tagged e^-. B) The recoil energy of the e^- as measured by the RESH. C) The noninteracting energy measured by the BGM/BCAL. D) The energy of the Interacting γ. 47
25 The sum of the residuals from a run by run basis. The values of the correction are $\theta_\gamma = 0.913$ mrad and $\phi_\gamma = 3.943$ rad. 48
26 The mass errors in the $\pi^+\pi^-$, the K^+K^- and $\pi^+\pi^-\pi^\pm$ channels from the final event selection. 51
27 The mass spectrum of the $\gamma N \rightarrow \pi^+\pi^-N$ (left) and $\pi^+\pi^-\pi^\pm$ (right) channels. The unhatched histograms show all the data, while the hatched histograms show those events that satisfy the opening angle requirement. 53
28 The $\gamma N \rightarrow \pi^+\pi^-N$ channel, exhibiting the $\rho(770)$ enhancement in the 0.7-0.8 GeV range. Note the skewed $\rho(770)$, a peak around 1.02 GeV ($\phi(1020) \rightarrow \mu^+\mu^-$ misidentified as $\pi^+\pi^-$), the $\rho'(1600)$, and the $J/\psi(3097)$ (from $J/\psi(3097) \rightarrow \mu^+\mu^-$ with μ's misidentified as π's). 54

29 The decay angular distribution for the $\rho(770)$ in its helicity frame. The left histogram contains uncorrected events while the histogram on the right shows the same events corrected for detector acceptance. The smooth curve shows the $\sin^2\theta$ distribution of a $J^{PC} = 1^{--}$ meson with relatively little background. 55
30 The t' distribution of the $\rho(770)$. 56
31 The $\gamma N \rightarrow \pi^+\pi^- N$ channel, exhibiting the $\rho'(1600)$ enhancement in the 1.450-1.700 GeV range. The mass is 1.498 GeV with a width of 0.198 GeV. 57
32 The $\rho'(1600) \rightarrow \pi^+\pi^-$ helicity angle distribution. 58
33 The K^+K^- mass distribution. The events are restricted to those for which both Kaons are positively identified. These events are also restricted to the t' region $0.015 \leq t' \leq 0.2$ GeV^2. 60
34 The polar decay angular distribution for the $\phi(1020)$ in its helicity frame. The histogram has been corrected for acceptance. 61
35 The t' distribution of the $\phi(1020) \rightarrow K^+K^-$. 61
36 The $J/\psi(3097) \rightarrow \mu^+\mu^-$ mass spectrum. The unhatched histogram shows events with at least one μ positively identified, while the hatching indicates events with both tracks positively identified as μ's. A t' cut of $0.015 \leq t' \leq 0.2$ GeV^2 has been placed on these events. 63
37 The $J/\psi(3097) \rightarrow \mu^+\mu^-$ mass spectrum. The fit shown is with a Gaussian superposed with the Bethe-Heitler background and a decaying exponential. 64
38 The $\gamma N \rightarrow \pi^+\pi^-\pi^\pm N'$ channel showing the $a_2^\pm(1320)$ enhancement. The hatched histogram corresponds to those events surviving a $0.015 \leq t' \leq 0.2$ GeV^2 cut. Note that the $a_2(1320)$ is clearly seen near 1.30 GeV. 66

39 "Triangle" plot of $\pi^+\pi^-$ combinations. Note the presence of the $\rho(770)$, the $f_2(1270)$ and the $\rho_3(1690)$, as evident by the dark bands through these respective masses. The events from the $J/\psi(3097)$ also form a band along the 3.1 GeV bin. 67
40 The neutral dipion combinations in the $\gamma N \rightarrow \pi^+\pi^-\pi^\pm N'$ channel. 68
41 The neutral dipion combinations in the $\gamma N \rightarrow \pi^+\pi^-\pi^\pm N'$ channel subjected to a $0.015 \leq t'_{\gamma;3\pi} \leq 0.2$ GeV^2 cut. 69
42 The $\rho(770)\pi^\pm$ combinations in the $\gamma N \rightarrow \pi^+\pi^-\pi^\pm N'$ channel. The $\rho(770)$ mass region is defined to be 0.60 GeV $\leq \rho(770) \leq$ 0.90 GeV. 73
43 The $f_2(1270)\pi^\pm$ combinations in the $\gamma N \rightarrow \pi^+\pi^-\pi^\pm N'$ channel. The mass of the $f_2(1270)$ is taken to be 1.10 GeV $\leq f_2(1270) \leq$ 1.40 GeV. 74
44 The $\rho_3(1690)\pi^\pm$ combinations in the $\gamma N \rightarrow \pi^+\pi^-\pi^\pm N'$ channel. The $\rho_3(1690)$ mass is taken to be 1.50 GeV $\leq \rho_3(1690) \leq$ 1.80 GeV. 75
45 The $\rho(770)\pi^\pm$, $f_2(1270)\pi^\pm$ and $\rho_3(1690)\pi^\pm$ combinations with a $0.015 \leq t' \leq 0.2$ GeV^2 cut applied. 77
46 The $J/\psi(3097)\pi^\pm$ combinations. 78
47 The SROGUE results showing the derivation of the photon energy. A) The tagged e^- energy. B) The RESH energy. C) The BGM energy. D) The interacting photon energy. 84
48 The SROGUE results showing the photon flux reaching the BGM. 85
49 The mass acceptance curve for the 2π channel. These are the events that have passed all the analysis cuts, including the $0.015 \leq t' \leq$ 0.2 GeV^2 cut. 85
50 The Monte Carlo acceptance for the $\phi(1020) \rightarrow K^+K^-$ channel. . . 86

51 The HC and CHC energy response for the μ's passing through those detectors. The histogram on the left is from the Monte Carlo; the shaded region indicates those events having an energy less than 5 GeV. The histogram on the right is the HC and CHC energy from the data. 87

52 The mass acceptance curve for the 3π channels. The curve shows the efficiency of the 3π events passing all analysis cuts. 88

53 The diffractive $J/\psi(3097)$ (left) and $J/\psi(3097)\pi^{\pm}$ (right) events from the Monte Carlo generation of diffractive $J/\psi(3097)$ events with embedded electron pairs. 89

Chapter 1

Introduction to High Energy Physics

Particle physics is the study of the fundamental constituents of matter and has its origin in the 1930's when several important discoveries changed our understanding of the physical world. In 1932 the neutron was discovered by Chadwick[1], in 1933 the positron was identified by Anderson[2], in 1934 the first field theoretic model of β decay was developed by Fermi[3], and in 1937 the μ-meson was found by Neddermeyer and Anderson[4] and confirmed by Street and Stevenson[5]. These discoveries showed that the atom itself could no longer be regarded as a fundamental constituent of matter but that it was composed of smaller elements. By the late 1950's many more particles had been recorded than could be explained by any contemporary theories. Examination of these particles showed that they exhibited interactions amongst themselves which scaled much stronger than the gravitational and electromagnetic forces, as well as stronger than β decay (now known as the weak interaction). These strongly interacting particles became known as hadrons.

As experimentation continued, a vast array of different particles were discovered. In 1969 SLAC's ep scattering experiments gave evidence for an underlying

Table 1: The naming convention for the light mesons based upon quark content and observable quantum numbers. These states have no admixture of u or d with strangeness or other heavy flavors. The J of the mesons are generally included as a subscript, as with the $f_2(1270)$ or $\rho_3(1690)$.

	$J^{PC} =$	0^{-+}	1^{+-}	1^{--}	0^{++}
		2^{-+}	3^{+-}	2^{--}	1^{++}
		$\vdots$	$\vdots$	$\vdots$	$\vdots$
$q\bar{q}$ content	$^{2S+1}L_J =$	$^1(L\,\text{even})_J$	$^1(L\,\text{odd})_J$	$^3(L\,\text{even})_J$	$^3(L\,\text{odd})_J$
$u\bar{d}$, $d\bar{u}$	$(I=1)$	π	b	ρ	a
$u\bar{u} - d\bar{d}$, $d\bar{d} + u\bar{u}$ &/or $s\bar{s}$	$(I=0)$	η, η'	h, h'	ω, ϕ	f, f'
$c\bar{c}$		η_c	h_c	ψ	χ_c
$b\bar{b}$		η_b	h_b	Υ	χ_b
$t\bar{t}$		η_t	h_t	θ	χ_t

structure for the nucleon[6, 7]. This result was later corroborated by CERN neutrino experiments[8]. By the early 1970's this nucleon substructure, originally called partons, was realized to be essentially the same as contained in the quark model, which had been introduced independently by Zweig and Gell-Mann[1].

A principal feature of the quark model, as it has been developed over the years, is that hadrons are composed of point-like fermions, with fractional charge and an additional degree of freedom called color. A fundamental tenet of the quark model is the existence of six quarks, or flavors, although the crucial observations required to establish the existence of the top quark have not been made. Exploitation of the symmetries in the quark model yields $q\bar{q}$ states (mesons) with integer spin and qqq states (baryons) with half integer spin. The naming scheme as presented by the Particle Data Group[9] for most of the light mesons is given in Table 1.

[1]Gell-Mann gave the name *quark* in a now famous quote (at least in particle physics circles), from James Joyce's *Finnegan's Wake*: "... another three quarks for Muster Mark."

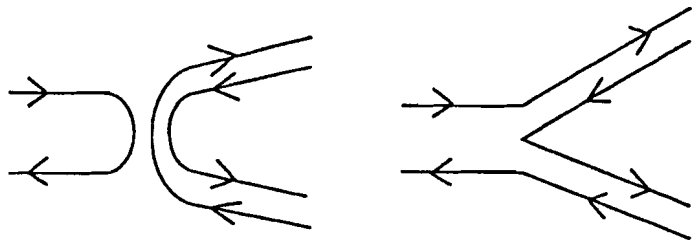

Figure 1: The diagram on the left shows a schematic representation of OZI forbidden transitions while the right represents allowed transitions.

Quantum Chromodynamics (QCD), used to describe the dynamics of high energy hadronic systems, requires the presence of gluons to bind quarks together into particles. The gluons interact not only with quarks, but also with each other. This interaction is energy dependent, which provides an explanation of why free quarks have not been directly observed.

Overall, the quark model is extremely successful at predicting experimentally known states. Searches continue for mesonic states that exist outside the context of the quark model. These searches include seeking mesons that have no place in $q\bar{q}$ nonets or that have exotic quantum numbers[9, 10]. In addition, mixtures of quarks and gluons ($q\bar{q}g$) and perhaps $q\bar{q}q\bar{q}$ states may exist. The possible existence of one such candidate state, $J/\psi\pi^{\pm}$, will be examined in this work. Close and Lipkin[11] have predicted the possibility of two $q\bar{q}q\bar{q}$ states which decay into $\phi\pi$ and $J/\psi\pi$. The photoproduction of a $q\bar{q}$ meson that decays via $\phi\pi$ (made of an $s\bar{s}$ quark pair and a pion) or $J/\psi\pi$ (made of a $c\bar{c}$ quark pair and a pion) cannot occur unless an OZI (Okubo-Zweig-Iizuka - see Close[12] for references) forbidden transition occurs. The OZI rule essentially states that quark diagrams that have continuous lines are heavily favored over quark diagrams that have disconnected lines, as shown in Figure 1. If an OZI forbidden transition does occur, the $J/\psi\pi$ combination would be a suppressed decay mode of a $q\bar{q}$ state. Other presumably larger decay channels would be expected to exist and these should have been seen by other experiments. Since no known isovector state exists in this mass region[9], the state may be a $q\bar{q}q\bar{q}$ state.

Chapter 2

Meson Production

This work examines peripheral photoproduction of various light quark mesons. The light quark mesons that have been firmly established are shown in Figure 2[13].

2.1 The Vector Dominance Model (VDM)

The Vector Dominance Model (VDM) describes the interaction of the nucleon and photon in the scattering process[14]. This model adds a hadronic component to the bare electromagnetic photon which then interacts with the target. These hadronic states must be neutral mesons which couple to the bare photon with the strong coupling constant $\sqrt{\alpha}$. The wavefunction will take the form:

$$|\gamma> = \sqrt{Z_3}\,|\gamma_{\text{Bare}}> + \sqrt{\alpha}\,|h> \tag{1}$$

where $\sqrt{Z_3}$ is a Quantum Electrodynamic (QED) normalization constant and $|\gamma_{\text{Bare}}>$ and $|h>$ are the bare electromagnetic and hadronic states. Since a strong interaction is assumed, the reaction conserves Isospin and G-Parity. The hadronic states are also required to maintain the helicity of the photon. These properties illustrate one of the more salient features of photoproduction – namely that the

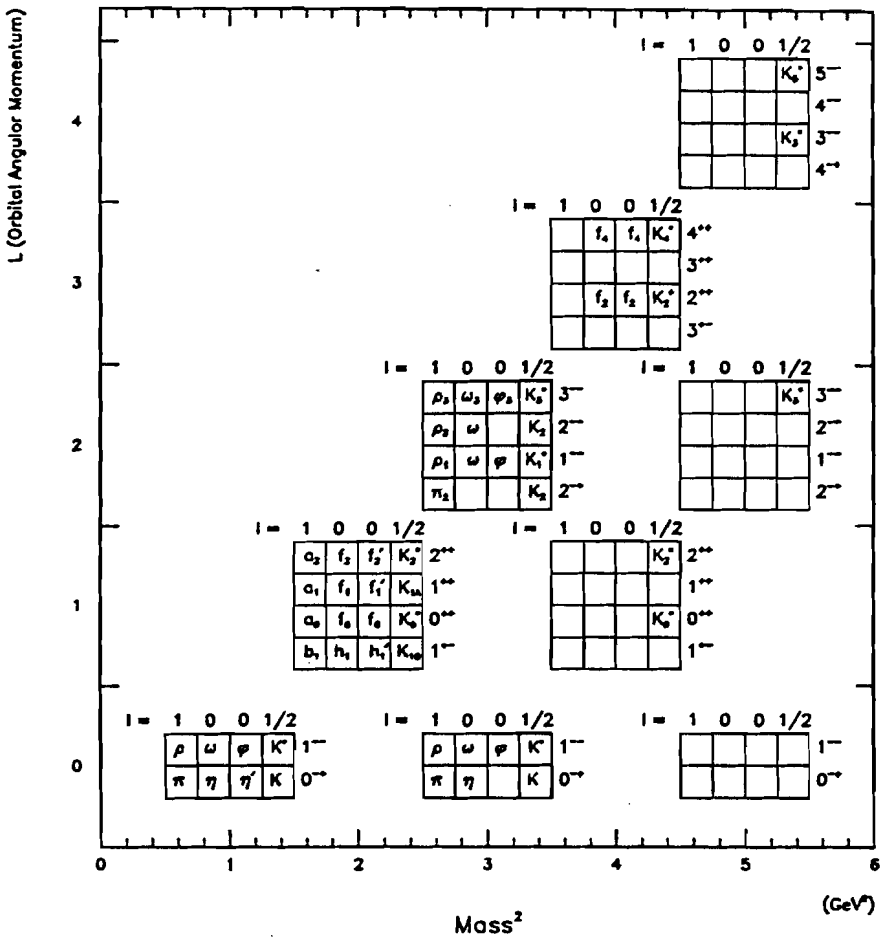

Figure 2: The (u, d, s) mesons below 2.5 GeV in a Chew-Frautschi plot. The mesons are ordered to show their relative angular momentum L versus their mass squared.

final states reflect most of the properties of the photon. The scattering mechanism is mediated by the exchange of a virtual particle, and diffractive scattering is dominated by Pomeron[1] exchange ($J^{PC} = 0^{++}$).

At high energies Pomeron exchange dominates one pion exchange (OPE) in peripheral photoproduction processes. In early photoproduction experiments OPE was thought to be essentially nonexistent when E_γ was above 10 GeV[16]. Subsequent work at 20 GeV, however, has shown evidence for charge exchange processes such as $\gamma p \rightarrow \Delta^{++}\rho^-(770)$, $\Delta^{++}a_2^-(1320)$, and $na_2^+(1320)$[17, 18, 19]. Some of the more important features of Pomeron exchange versus OPE are listed below[20]:

- The total photoproduction cross-section is not dependent upon energy, or at least is relatively constant over a large energy range. OPE predicts that it should vary as s^{-2} which is not seen experimentally.

- The absolute cross-section for $\gamma p \rightarrow \rho p$ is predicted and measured to be of the order of 10 μb, whereas the OPE prediction is several orders of magnitude smaller than what is observed.

- Decay angular distributions of the final states of a 1^- meson adhere to a $\sin^2\theta$ distribution in the helicity frame, which Pomeron exchange does predict but OPE does not.

- The mass distribution of the photoproduced ρ shows a distinct skewing toward lower mass, which again OPE does not predict. This can be explained in terms of p-wave dipion interference[21], which will be exploited later in this analysis.

The Bethe-Heitler Dilepton Cross-Section

Aside from the photon's hadronic coupling, it also couples to to the electromagnetic field. The photon may produce dileptons (e^+e^-, $\mu^+\mu^-$, $\tau^+\tau^-$) inside the

[1]The Pomeron is modeled in QCD via a double gluonic exchange process[15].

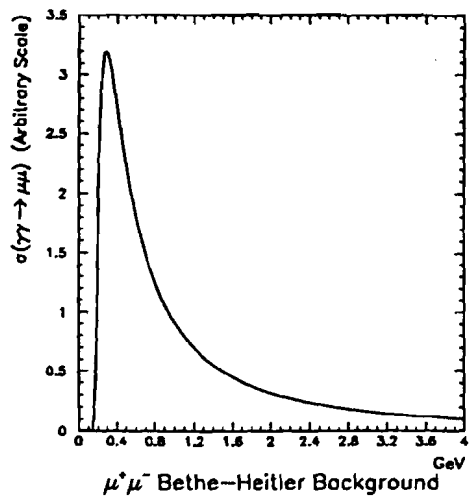

Figure 3: The Bethe-Heitler dimuon background.

experimental target via the exchange of a virtual photon provided by the large coulombic fields near the target nuclei.

For $\mu^+\mu^-$ pair production, which is of great interest here, the cross-section derived from QED is:

$$\sigma_T(\gamma\gamma \to \mu^+\mu^-) \approx \frac{4\pi\alpha^2}{m_{\mu\mu}^2}\left(\ln\frac{m_{\mu\mu}^2}{m_\mu^2} - 1\right) \tag{2}$$

where $m_{\mu\mu}^2 \equiv s$ is the overall center of mass energy, α is the fine structure constant and m_μ^2 is the square of the muon mass. In this formula a large s approximation has been used[22] to avoid logarithmic divergences. The form of the Bethe-Heitler background is shown in Figure 3 and is well fit by the sum of two decaying exponentials when the dimuon mass exceeds 0.5 GeV.

The VDM Prediction for the Photoproduction of Light Mesons

A more detailed look at the VDM shows predictions for the relative production rates of vector mesons. At sufficiently high energies, the hadronic component will dominate the electromagnetic (or photonic) portion of the interaction, and the interaction will proceed as a coherent mixture of neutral vector mesons (ρ, ω, ϕ, J/ψ, ...). To lowest order the interacting hadronic states will be[16]:

$$\sqrt{\alpha} \mid h >= \sum_V \left(\frac{e}{f_V}\right) \left[\frac{m_V^2}{m_V^2 + Q^2}\right] \mid V > \tag{3}$$

where e/f_V measures the strength of the photon-meson coupling and Q^2 is the photon "mass" ($E_\gamma^2 - \mid \vec{k} \mid^2 \equiv Q^2$) so that the term in the square brackets accounts for off-mass-shell photons. In peripheral photoproduction one assumes that the photon is on shell, $Q^2 = 0$, so that the states $|V>$ are summed with only the photon-meson coupling. This leads to the basic premise that photons couple directly to vector mesons. With the assumption that little mixing occurs between the vector mesons (the so-called diagonal approximation), the following differential cross-section may be found[19]:

$$\frac{d\sigma}{dt}(\gamma N \rightarrow VN') = \frac{\alpha}{4}\frac{4\pi}{f_V^2}\frac{d\sigma}{dt}(VN \rightarrow VN') \tag{4}$$

where ($\gamma N \rightarrow VN'$) is the differential cross-section for vector meson photoproduction from a nucleon, and ($VN \rightarrow VN'$) is the cross-section for vector meson scattering.

The optical theorem relates the imaginary part of the forward elastic scattering amplitude to the total cross-section, giving:

$$\frac{d\sigma}{dt}(\gamma N \rightarrow VN')|_{t=0} = \frac{\alpha}{64\pi}\frac{4\pi}{f_V^2}\sigma_{\text{Total}}^2(VN)(1 + \eta_V^2) \tag{5}$$

where η_V^2 is the ratio of the real to imaginary part of the forward scattering amplitude. Additionally, quark model predictions are used to relate the vector meson-nucleon scattering to π- and K-nucleon elastic scattering data. The photon-meson

Table 2: Previous experimental results for the cross-section of various vector mesons at different interaction energies.

Previous Experimental Cross-Sections			
Particle	Experiment	Cross-Section (μb)	γ Energy (GeV)
$\rho(770)$	LBL-SLAC	13.5 ± 0.5	9.3 GeV
$\rho(770)$	BC72-73	11.1 ± 0.9	20 GeV
$\rho(770)$	OMEGA	9.4 ± 0.1	20-70 GeV
$\phi(1020)$	LBL-SLAC	0.55 ± 0.07	9.3 GeV
$\phi(1020)$	E401	~ 0.61	45-165 GeV
$\rho'(1600) \rightarrow \pi^+\pi^-$	BC72-73	0.15 ± 0.01	20 GeV
$\rho'(1600) \rightarrow \pi^+\pi^-$	OMEGA	0.10 ± 0.02	20-70 GeV
$\rho'(1600) \rightarrow \pi^+\pi^-$	E400	0.07 ± 0.03	45-160 GeV

couplings f_V may then be calculated. The couplings are proportional to the cross-sections, and various production ratios may be found[16].

The cross-section for the diffractively photoproduced $\rho(770)$ has been found to be approximately flat over a large range, while the $\phi(1020)$ cross-section is found to increase (as shown in Figure 4 [23, 24, 25, 26, 27, 28, 29]). The cross-sections from various experiments are given in Figure 4 and in Table 2 [23, 26, 30, 31, 32, 33]. The curves in Figure 4 represent a quark model prediction deduced from the $\rho(770)$ and $\phi(1020)$ elastic cross-sections[16]. Based on the results of the quark model predictions[28] presented in Figure 4, the ratio of the $\rho(770)$ cross-section to the $\phi(1020)$ cross-section at an energy of 120 GeV is 1/16.

Interference effects from the 2π decay mode of the $\omega(783)$ should be small, since the decay $\omega(783) \rightarrow \pi^+\pi^-$ accounts for only about 2% of the total decays of the $\omega(783)$. The $\phi(1020) \rightarrow K^+K^-$ decay accounts for 49.1% of all $\phi(1020)$ decays, and direct comparison with the $\rho(770) \rightarrow \pi^+\pi^-$ channel should produce a ratio of one $\phi(1020)$ for every thirty-three $\rho(770)$'s.

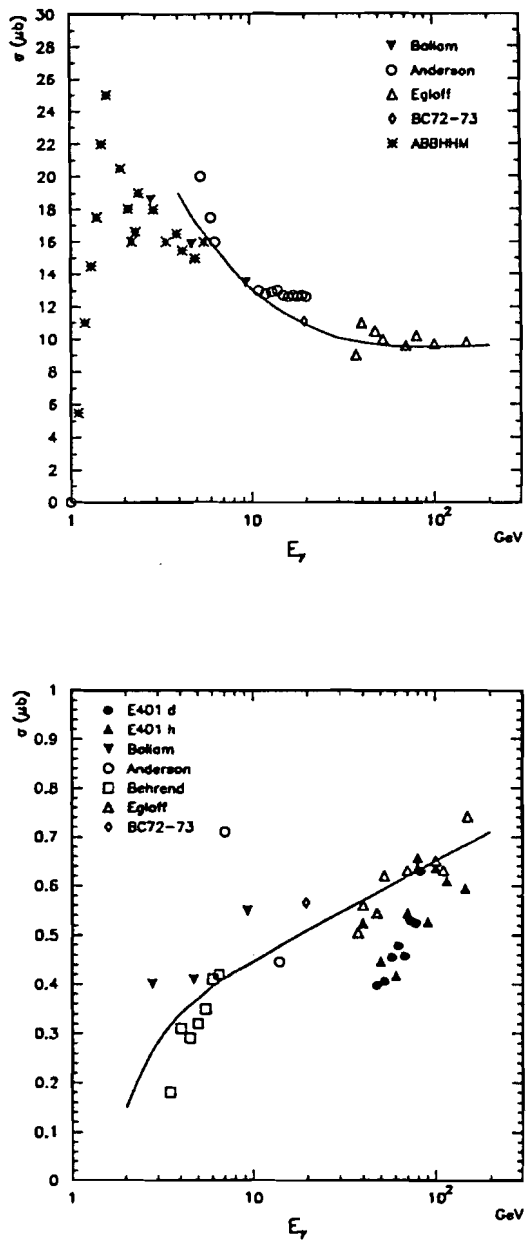

Figure 4: The variations in cross-sections for the $\rho(770)$ (upper graph) and $\phi(1020)$ (lower graph) for various photon energies.

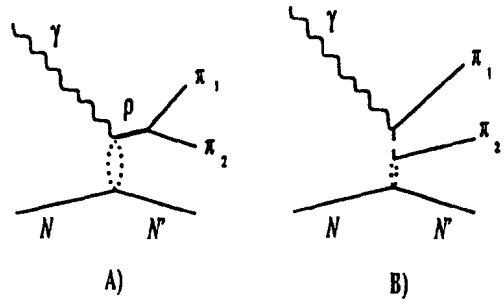

Figure 5: (A) The Breit-Wigner Resonance term for $\rho(770) \rightarrow \pi\pi$. (B) The Drell term for the Söding description of the photoproduced $\rho(770)$.

Diffractive Dissociation and the Söding Model of $\rho(770)$ Meson Photoproduction

To describe the effects of diffractive dissociation in $\rho(770)$ production, the photon is written in terms of a phenomenological Ansatz which includes "Drell" type processes[2], where a nonresonant p-wave background is formed via virtual pion exchange with the nucleon (see Figure 5). The ordering ambiguity of the pions in the Drell term introduces a third term.

The cross-section is determined by squaring the sum of the three matrix elements and integrating over the energy. This yields three quadratic terms and three cross terms. The three cross terms drop out after summing over polarizations. The remaining contributions are illustrated in Figure 6, which shows the functional contributions of the three terms in the cross-section, and the resulting dipion spectrum generated for the $\rho(770)$ meson by Monte Carlo techniques. The first term in the cross-section is a Breit-Wigner type resonance with the relativistic form:

$$\sigma_{\text{Breit-Wigner}} = \frac{m_{\pi\pi}}{q} \frac{m_\rho \Gamma_\rho}{(m_\rho^2 - m_{\pi\pi}^2)^2 + m_\rho^2 \Gamma_\rho^2} \quad . \tag{6}$$

The second term represents the effect of the Drell background and the third term,

[2]This derivation follows the work of Söding[21].

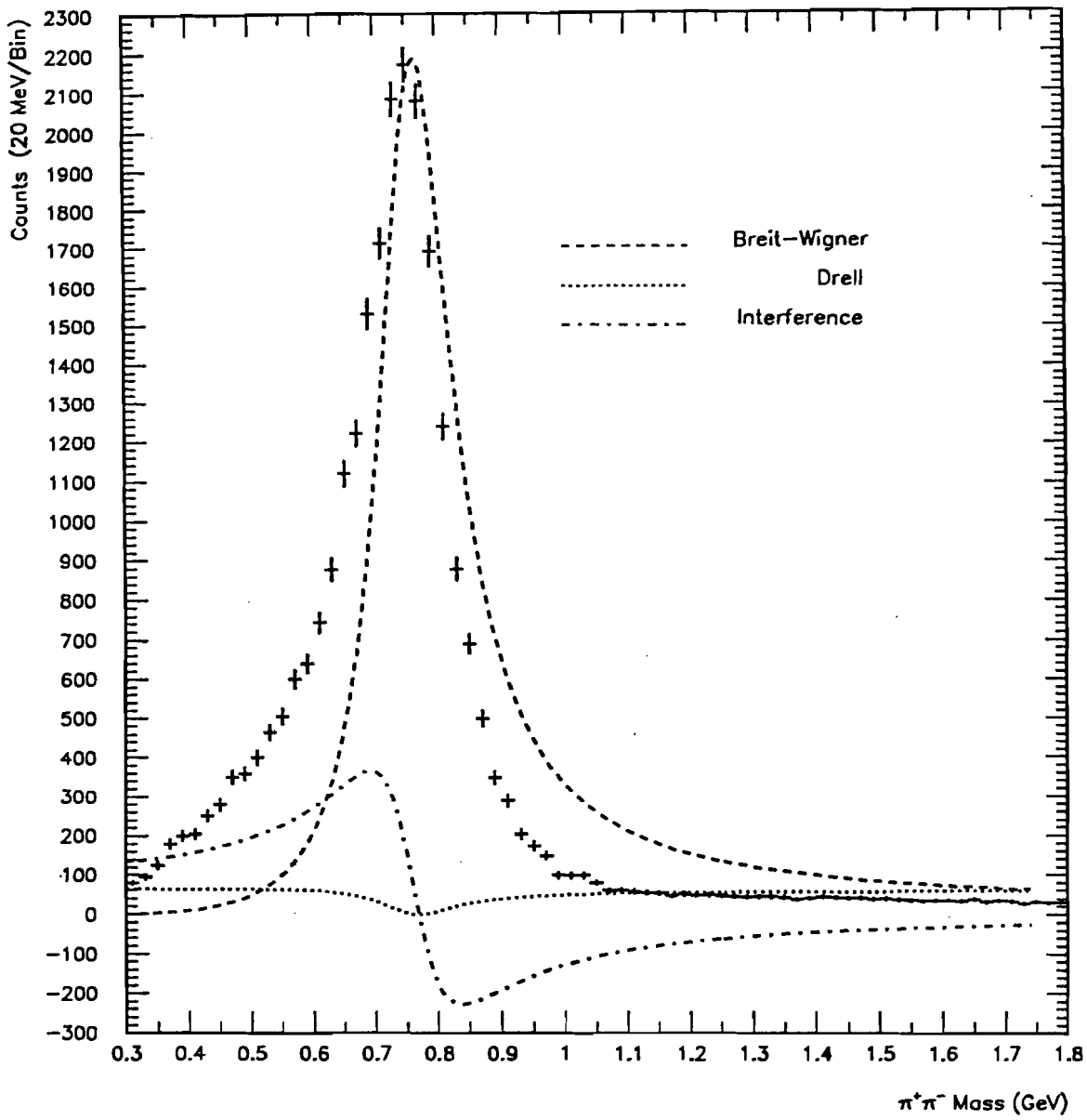

Figure 6: The effects of the three individual scattering terms which combine to produce the Söding mass shift. The + points represent the Monte Carlo data points. For a comparison to the experimental data, see Chapter 4.

the Interference term, accounts for the pion ordering. These terms are[34]:

$$\text{Drell}(m) = \frac{(m_{\pi\pi}^2 - m_\rho^2)^2}{(m_\rho^2 - m_{\pi\pi}^2)^2 + m_\rho^2\Gamma_\rho^2} \tag{7}$$

and

$$\text{Interference}(m) = \frac{(m_{\pi\pi}^2 - m_\rho^2)}{(m_\rho^2 - m_{\pi\pi}^2)^2 + m_\rho^2\Gamma_\rho^2} \tag{8}$$

where q is the pion momentum in the dipion center of mass and the modified width Γ_ρ is given by

$$\Gamma_\rho = \Gamma_\rho^\circ \left[\frac{q(m_{\pi\pi})}{q(m_\rho)}\right]^3 \frac{2q^2(m_\rho)}{q^2(m_{\pi\pi}) + q^2(m_\rho)} \tag{9}$$

where m_ρ and Γ_ρ° are the PDG[9] ρ mass ($m_\rho = 768.1$ MeV) and width ($\Gamma_\rho^\circ = 151.2$ MeV). It should be noted that these terms are relatively independent of the incident photon energy.

2.2 Charge Exchange Scattering Versus Double Regge Processes

Charge exchange processes occur when charge must be balanced across an interaction vertex[3]. These reactions can not be mediated by Pomeron exchange. The pion has a small mass which means it may be involved over a large range of distances (and be observable in a peripheral (small t) sample of events). The possibility of pion exchange suggests the possible observation of charged mesons, such as the $a_2(1320)$ from photoproduction reactions. The effects of pion exchange are energy dependent and diminish with increasing interaction energy, as has been previously reported[34]. The effect may still be observable in a high statistics experiment, such as E687.

The double Regge process (or double peripheral mechanism) may be thought of as an intermediate process between Pomeron and charge exchange. The process

[3]For example, the following process must have charge exchange: $\gamma p \rightarrow \rho^-(770)\Delta^{++}$.

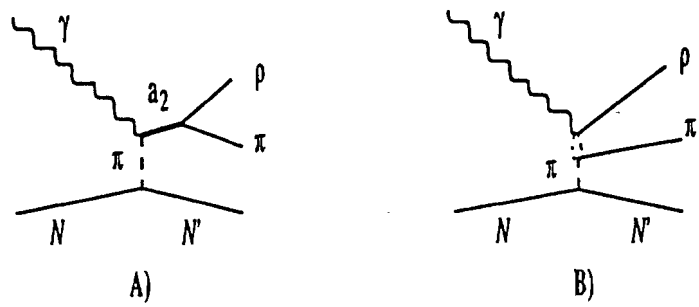

Figure 7: (A) The direct production process in charge exchange. (B) The double Regge (or double peripheral) production process.

entails the exchange of a Pomeron coupled with the exchange of a charged particle, as illustrated in Figure 7. Again the pion is the most likely contribution since it is relatively light, and has a strong coupling to the NN' vertex.

Wolf[35] has calculated the interaction energy dependence of the cross-section for double peripheral processes. He shows that the cross-section is relatively flat and peaks at higher mass as the interaction energy increases. Extrapolation to higher interaction energies indicates negligible contributions above an interaction energy of 20 GeV. Thus any structure seen in the charge exchange process should be indicative of resonance formation. In an early review article Bauer *et al.*[16] suggest that charge exchange photoproduction processes become negligible for laboratory photon energies in excess of 10 GeV. However, at 20 GeV, subsequent work has shown that substantial charge exchange cross-sections exist for the reactions $\gamma p \rightarrow \rho(770)^- \Delta^{++}$, $a_2^-(1320)\Delta^{++}$ and $a_2^+(1320)n$[17, 18, 19].

2.3 The Kinematics for Experimental Analysis

The experimental analysis makes use of the following kinematic variables:

1. The frame invariant Mandelstem variables built from the 4-momenta:

$$s = [k_\mu(\gamma) + p_\mu(p)]^2 = m^2 \tag{10}$$

and

$$t_{\gamma;n\pi} = \left[k_\mu(\gamma) - p'_\mu(V \to n\pi)\right]^2 \tag{11}$$

where k_μ is the 4-momentum of the photon, p_μ is the 4-momentum of the proton and $p'_\mu(V \to n\pi)$ is the 4-momentum for the meson V which decays into $n\pi$, where n is the number of pions (or Kaons, muons, *etc.*) that are formed in the decay of the meson. We will often abbreviate $t_{\gamma;n\pi}$ as simply t.

2. The variable $t'_{\gamma;n\pi}$ ($t'_{\gamma;n\pi} \equiv t'$) defined as:

$$t' = [t - t_{\mathrm{Min}}]\,|_{\mathrm{CM}}. \tag{12}$$

A sample restricted to low values of t' is comprised primarily of diffractive or OPE events. Qualitatively, the t' distribution for Pomeron exchange will exhibit a sharp exponential decay, while OPE will be similar but with less of an exponential slope. The exchange of heavier mesons ($a_2(1320)$, $f_2(1270)$, *etc.*) have never been convincingly observed in peripheral photoproduction processes.

The study of the photoproduction of light quark mesons is often enhanced by investigation of their decay angular distributions. Thus, for example, both elastic (γp $\to$ $\rho^\circ(770)$p) and inelastic (γp $\to$ $N^\star\rho^\circ(770)$) $\rho^\circ(770)$ photoproduction have been found to conserve s-channel helicity[30, 34]. This has also been found to be true for the reactions γp $\to$ $\omega(783)$p and $\phi(1020)$p, which suggest that vector meson photoproduction conserves s-channel helicity and has led to the speculation that all diffractive photoproduction reactions will conserve helicity in the s-channel (s-channel helicity conservation, or SCHC). In the current experiment we shall investigate the decay angular distributions for the reactions γp $\to$ $\rho^\circ(770)$p and γp $\to$ $\phi(1020)$p. For the other states we observe, large backgrounds prohibit meaningful interpretations of these distributions.

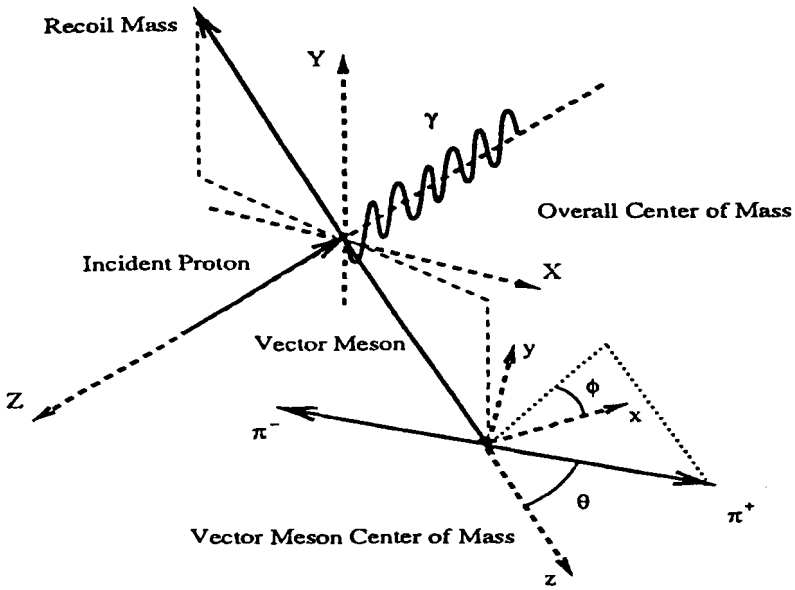

Figure 8: The helicity angles θ and ϕ for the $\pi^+\pi^-$ decays where $\hat{\pi}$ is chosen as the direction of the π^+ in the dipion rest frame.

The decay angular distributions for this analysis are best defined in the helicity frame. For a description of the angles[36], see Figure 8. The z axis in the helicity frame is defined as the direction of the final state particle (meson) in the γp center of mass frame. The y axis is defined by the cross product of the directions taken by the γ and vector meson V, namely $y = \vec{k}_\gamma \times \vec{\mathrm{V}}$. The remaining direction x is determined from the cross product of $y \times z$. The spherical angles θ and ϕ are found by using an analyzing vector $\hat{\pi}$. For the 2π decay modes, $\hat{\pi}$ is chosen as the direction of the π^+ in the rest frame of the dipion system. The Gottfried-Jackson frame, which is relevant to one pion exchange processes, is identical to the helicity frame except that the z axis is taken to be the direction of the incident photon in the rest system of the meson being studied.

Chapter 3

Experimental Setup of E-687

The photon beam for E687 was generated from Fermilab's proton accelerator, the Tevatron, in a multi-stage process. The final interacting γ beam was produced by the bremsstrahlung radiation of an electron beam. The initial energy of the electron beam was measured with a spectrometer called the Tagging system. The recoil energy of the electron after the bremsstrahlung was measured in the Recoil Electron Shower Hodoscope (RESH) to deduce how much energy was released by the electron in the bremsstrahlung process. With the measurement of any noninteracting photons in either the Beam Gamma Monitor (BGM) or Beam Calorimeter (BCAL) the interacting photon energy could be ascertained.

The E687 detector was made of several separate components. The detector had two large magnets (M1 and M2) with opposite polarities. This allowed the detector to operate as a large spectrometer which separated and measured the momenta of oppositely charged particles (see Figure 9). A silicon strip microvertexing detector (SSD) was used for event vertexing, while five proportional wire chambers (PWC) interspersed throughout the detector provided tracking and momentum measurements. Electromagnetic and hadronic calorimeters measured particle energies and Čerenkov detectors provided particle identification. Muon chambers were also available for muon identification. Each subsystem will be examined in greater detail in the following sections. Figure 10 gives an overview of the detector.

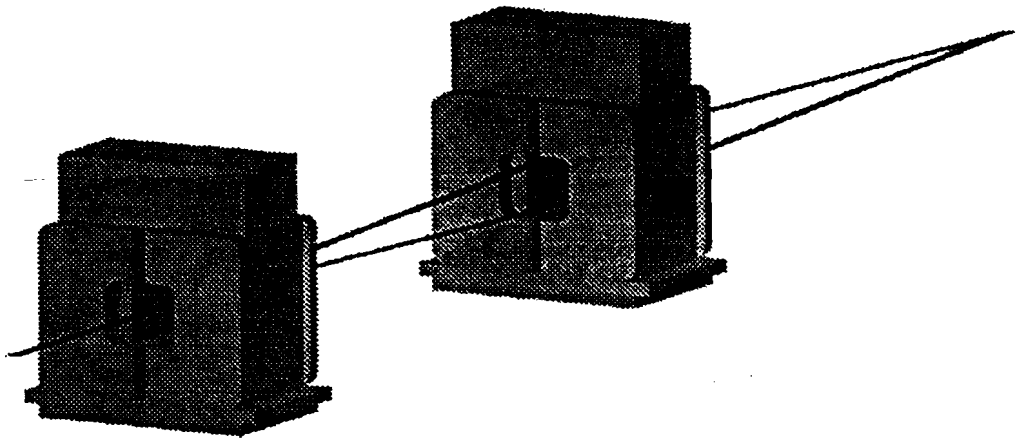

Figure 9: The E687 magnets are shown with a e^+e^- pair traced through the detector. The first magnet opens up the pair in the vertical (bend) direction while the second magnet (run with opposite polarity) closes the trajectories. The H×V hodoscope (not shown) is located at the final focus.

3.1 Fermilab Supplied Beams

Protons extracted from the Tevatron (see Figure 11) were split into three separate beam lines for the fixed-target experiments. They included the meson line, the muon/neutrino line, and the proton line. The proton line consisted of several separate lines, including Proton East (PE), at the end of which resided the Wide Band Hall and E687. The process of generating the photon beam involved several mechanisms that permitted the production of various particle beams: neutral hadrons, electrons, muons and pions, as well as photons. This was consistent with E687's philosophy of a versatile multipurpose beam[37]. The electrons, muons and pions were important options, as they were used to calibrate the detector.

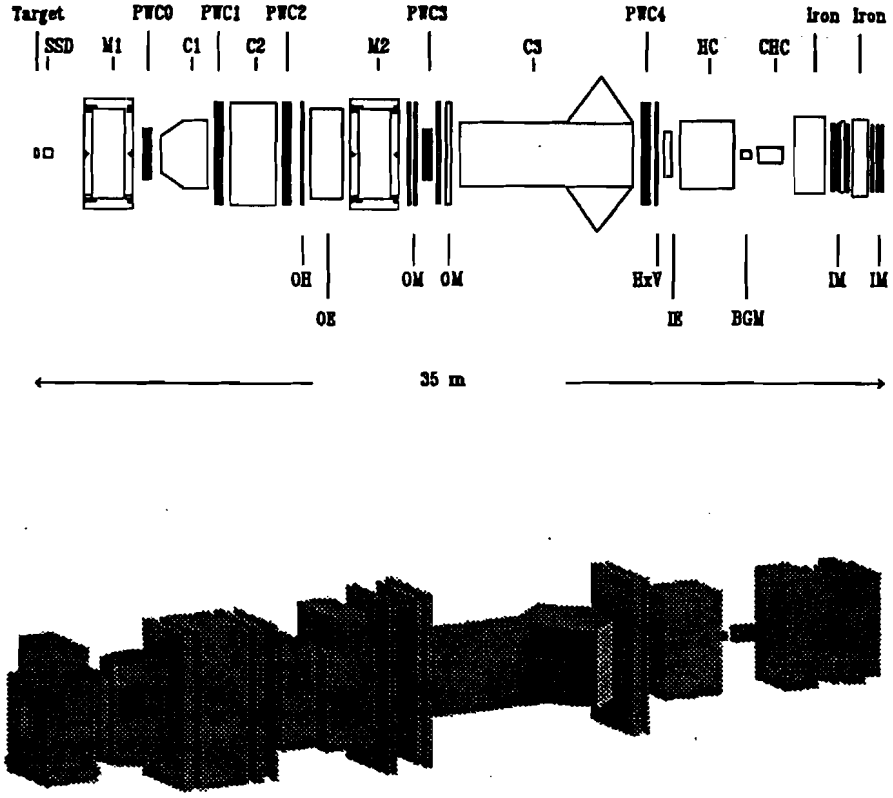

Figure 10: A plan view of the E687 detector and a 3D view. The target and SSD have been removed in the 3D view for clarity.

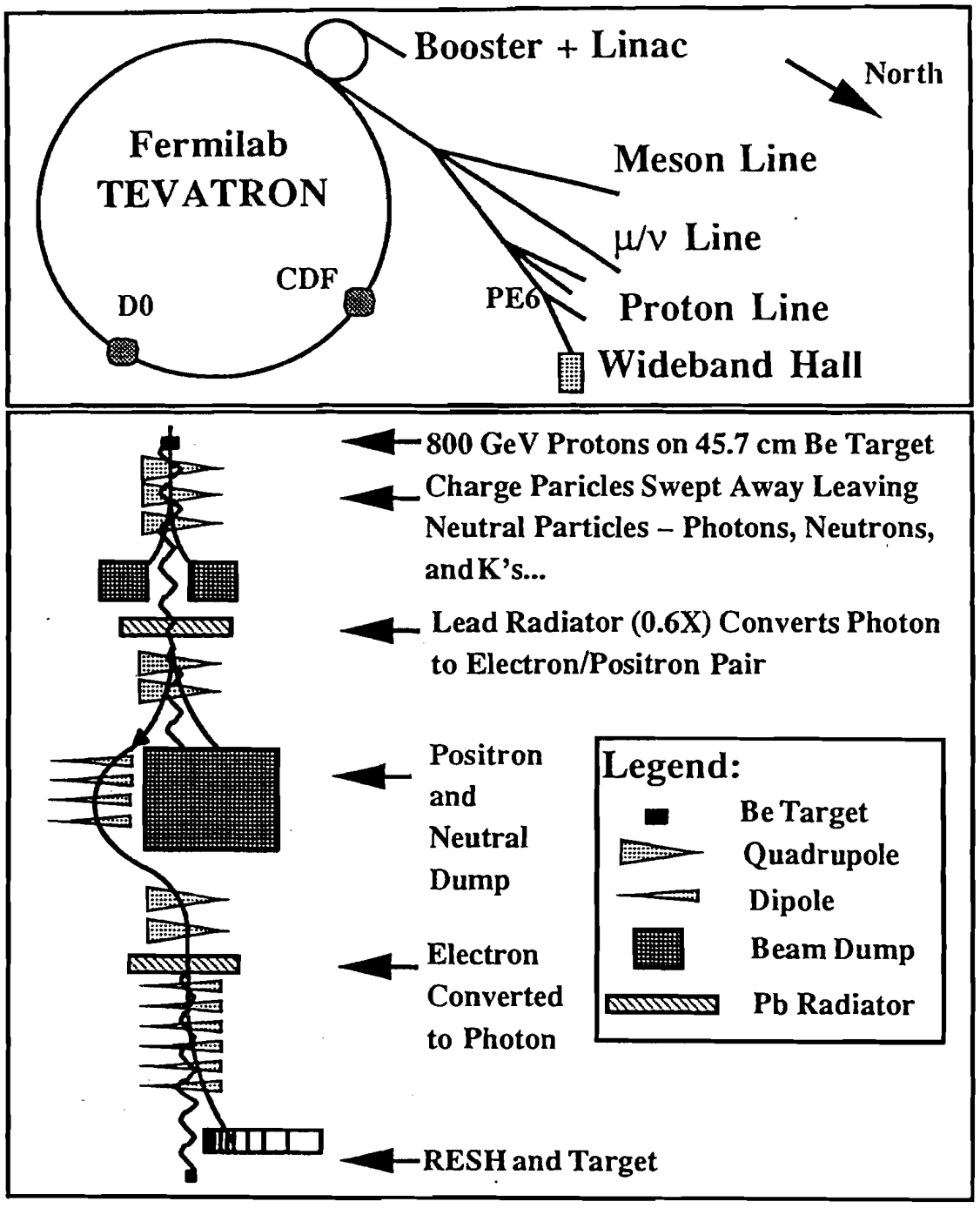

Figure 11: Schematic of Fermilab Beam Lines, and the Wide Band Photon Beam Line (*Not to scale*).

The γ Beam Line

The conversion of the proton beam into a photon beam employed standard beam optics techniques and entailed three major steps. First, the proton impinged upon a 46 cm beryllium target to generate an initial round of neutral particles (see Figure 11). The charged particles were swept away magnetically, leaving only a neutral beam comprised of neutrons, neutral K's, and photons (primarily from π° decays). The neutral beam was then passed through a lead converter where some photons were converted into e^+e^- pairs. The electrons were then swept around a beam dump, where any neutral and positively charged particles were absorbed. The beam momentum was nominally tuned to 350 GeV. The final bremsstrahlung beam was generated in front of the E687 spectrometer by allowing the electrons to pass through a 20% radiation length lead radiator.

Since the electron beam was passed through a relatively thick piece of material, multiple bremsstrahlung photons could be produced[38], as well as Bethe-Heitler e^+e^- pairs[1]. The energy and number of photons created via the bremsstrahlung process were tracked with EGS[39], an electromagnetic shower simulation package. The results[40] showed that the number of photons generated varied from zero to six (see Figure 12). Any additional noninteracting photons that still passed undetected (without converting into pairs) were measured at the downstream end of the detector.

The bremsstrahlung method produced a fairly clean beam with hadronic contamination of the order of 10^{-5} hadrons per photon. The principal source of contamination was negative pions generated in the first stage of the creation of the photon beam. These pions could have interacted in the lead radiator at the front of E687 and produced neutral particles which were a source of contamination in the detector. Similarly, negative muons could be produced in the initial stages of the beam generation causing a beam "halo" (contamination) when they entered

[1]These produced pairs are called "embedded pairs", and occur when additional photons pair-produce in the radiator or target during an event. The embedded pairs are distinguishable by the fact that they have separate vertices.

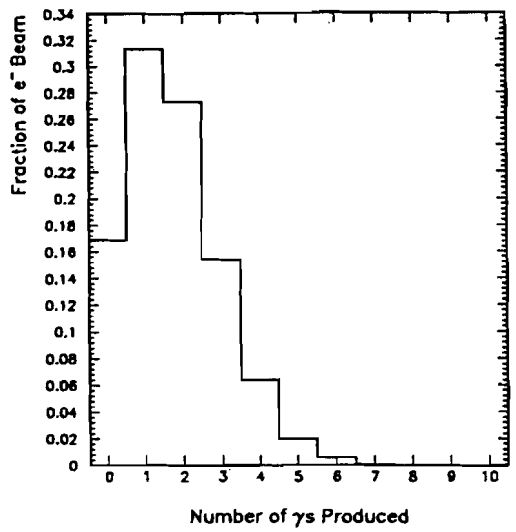

Figure 12: EGS result showing multiple γ production.

the detector.

3.2 The Target

Although the photon beam was directed into one of several different interchangeable targets, the principal target used in this experiment was a 4.41 cm beryllium target. The physical shape of the target was a combination of rectangular parallelopipeds. The "base" was made of two plates, each with a cross section of 2.54 cm^2 and a thickness of 0.8128 cm. Three remaining plates were designed to physically match the target with the high resolution area of the silicon strip microvertex detector (SSD) which was located further downstream.

3.3 Detector

Since the E687 detector had many interacting systems, the following subsections will give an overview of the major systems of the detector.

The Electron Tagging System and the γ Interaction Energy

A critical feature of nearly all high energy experiments is an accurate knowledge of the parameters of the incident beam. In this experiment the γ energy was not measured directly. In order to accomplish this, the electron's initial energy was measured upstream of the radiator at the bend in the electron beam by the Tagging system. After traversing the radiator, the electron was magnetically swept out of the beam into the RESH, which measured the energy of the deflected electron. The difference in these two energies was the amount of energy given up by the electron to create photons. Any additional energy in the beam line, which was due to noninteracting photons was measured at the downstream end of the experiment with either the BGM or the BCAL[2]. This noninteracting energy was subtracted off, leaving the interacting photon's energy.

The Tagging system was essentially a magnetic spectrometer which utilized a pair of dipole magnets that bent the electrons around the neutral dump. This deflection was measured by five microstrip detectors, as shown in Figure 13. The microstrips were large area detectors, measuring 7.7 cm $\times$ 5.7 cm and consisted of 256 strips, each with a 300 μm width. Two pairs of microstrip detectors measured the incident and outgoing angles, while the detector situated between the dipoles was used to resolve track projections and to differentiate true hits from noise. This was important for discriminating between two electrons in the same event and differentiating spurious signals from true hits which would have given a poor fit to the electron trajectory. The resolution of the tagging system was determined by using a pion beam tuned to three different energies (60, 100 and 300 GeV). A single

[2]The BGM was used during the 1988-89 and part of the 1990 run, while the BCAL as part of E683, was used after the inclusion of E683 during the 1991 run.

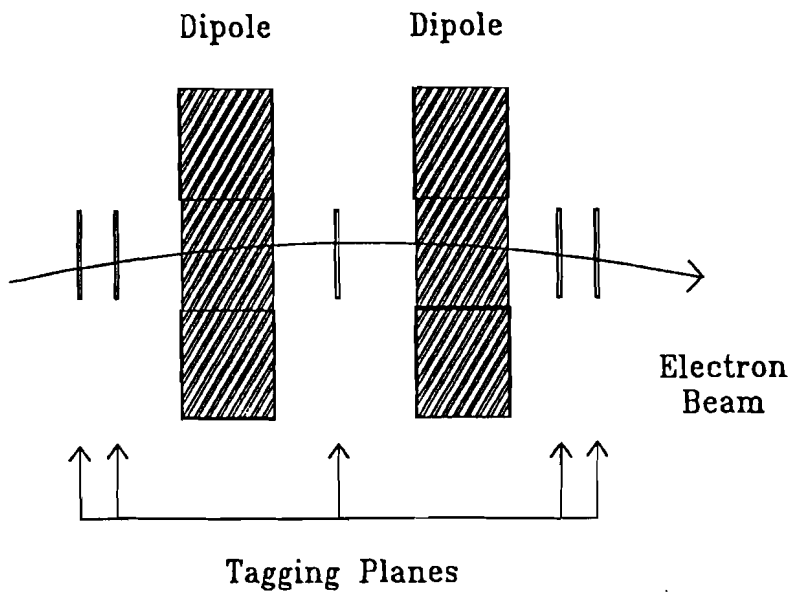

Figure 13: The Beam Tagging detector planes, located between the two dipoles of the double dog-leg for the electron beam.

pion was required to hit all five tagging planes and to generate a clean event in the detector (a clean event had tracks that were linked between the PWC and the SSD systems — more on this later in the Reconstruction section). The PWC system was used to calibrate the pion's momentum since the resolution and stability of the tracking system was well known. The tagging system's resolution slightly degraded the overall resolution and was fitted accordingly. At low energies (60 and 100 GeV) the resolution of the pion was dominated by the tagging system. The momentum was then extrapolated into higher momentum regions where the PWC resolution was dominant. The extrapolated resolution, ignoring multiple coulomb scattering (MCS) effects, was fit with a 2-parameter function, namely[41, 42]:

$$\frac{\sigma_p}{p} = \mathrm{P}_1 \cdot \left(\frac{p}{100\,\mathrm{GeV}}\right) \sqrt{1 + \left(\frac{23\,\mathrm{GeV}}{p}\right)^2} + \left(\frac{\mathrm{P}_2 \cdot p}{100\,\mathrm{GeV}}\right)^2, \tag{13}$$

where $\mathrm{P}_1 = 1.38\%$, $\mathrm{P}_2 = 0.25\%$. Acceptance studies by the beam tagging group indicated that the beam tagging system reconstructed the pion correctly in 81%

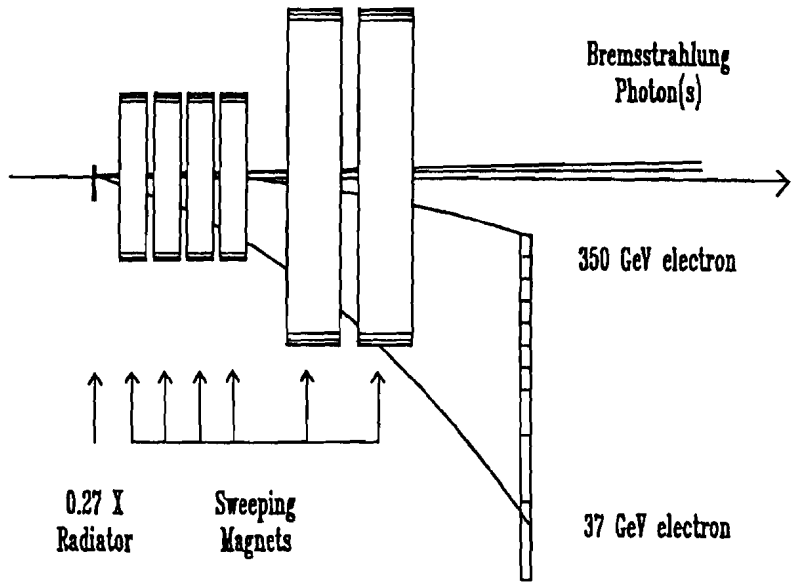

Figure 14: Schematic of the Recoil Electron Shower Hodoscope (RESH). Once a tagged electron passed through the lead radiator, it was swept into the RESH, which registered the hit in one of the ten fingers.

of all triggers used for study. The remaining 19% were lost to either acceptance limits, inefficiency, or both[42].

After the bremsstrahlung process the tagged electron's recoil energy was measured in order to deduce the energy of the photon. The electron was swept into the RESH (see Figure 14), where its energy was measured. The RESH consisted of ten lead-Lucite shower counters and was designed as a shower hodoscope. In this experimental analysis the RESH was used to quantize the recoil energy of the electron. Either one or two fingers of the RESH was required to fire in order to select an event. The finger struck by the electron determined the electron's recoil energy, which was taken as the energy required to strike the centroid of the finger. At this stage of the process, the energy lost by the electron was assumed to go entirely into the production of the single interacting photon. Any extra neutral energy was detected in the BGM/BCAL detector at the downstream end of the experiment. This energy consisted primarily of any noninteracting photons and

any other neutral particles in the beam. In the earlier runs of E687, the BGM, which consisted of 45 lead-Lucite layers (0.32 cm of lead), was employed for this purpose[43]. In later runs the BCAL, which was part of E683, was used. Signals from the latter device were tied into the E687 Data Acquisition System, and energies were recorded for it. The BCAL was designed to provide E683 with energy and position measurements. It contained forty-six 3.81 cm scintillators spread over 10 radiation lengths comprised of ninety-two 0.5 inch steel plates. In addition, the BCAL had ten PWC's that performed spatial measurements for jet events in E683.

The photon energy was determined on an event-by-event basis as follows:

$$E^{(\gamma)}{}_{\mathrm{INT}} = E^{(e^-)}{}_{\mathrm{TAG}} - \left[E^{(e^-)}{}_{\mathrm{RESH}} + \sum E_{\mathrm{BGM\,or\,BCAL}}\right]. \tag{14}$$

$E^{(\gamma)}{}_{\mathrm{INT}}$ was the photon energy given by the tagged energy of the electron, $E^{(e^-)}{}_{\mathrm{TAG}}$, after subtraction of the RESH and BGM energies, $E^{(e^-)}{}_{\mathrm{RESH}}$ and $\sum E_{\mathrm{BGM\,or\,BCAL}}$. In the event of pile-up or electronic overload, the BGM energy was not used[3].

Silicon Strip Microvertex Detector

The silicon strip microvertex detector (SSD) was used primarily to establish vertices and to detect in-flight decays of heavier mesons and baryons, particularly D's, K_s's and Λ's, which are sufficiently long-lived and decay within the detector. The SSD consisted of four sets of three planes (see Figure 15 and Table 3). The leading set was placed 4.6 cm downstream from the target. One of the three planes was oriented in the y (or vertical) direction, the other two were at angles of $\pm 45°$ with respect to the y axis. The first set of microstrip planes had twice the resolution of the other three sets. This increased the resolution of the tracks and provided a more accurate determination of the vertex position. Each plane of the SSD was further divided into inner and outer regions. The design of the SSD ensured greater track resolution by incorporating twice as many detecting strips

[3]In the event that the energy measured by the PWC exceeded the determined γ energy, then the PWC energy was used for the photon energy.

Table 3: Silicon Strip Detector Parameters.

Group	Number Channels	Active Area (cm^2)	Central Region (cm^2)	Width (I/O) (μm)	z (cm)	Depth (μm)
1	2064	3.5×2.5	3.5×1.0	25/50	4.6	300
2	2064	5.0×5.0	5.0×2.0	50/100	10.6	300
3	2064	5.0×5.0	5.0×2.0	50/100	16.6	300
4	2064	5.0×5.0	5.0×2.0	50/100	28.6	300

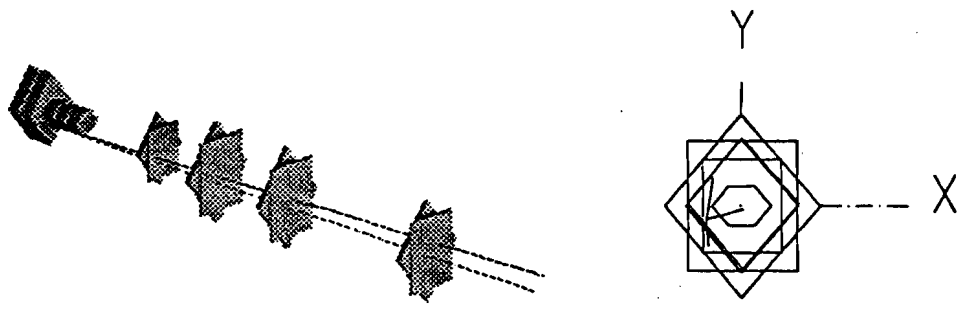

Figure 15: E687 Target and Silicon Strip Detectors. The first figure shows the orientation of the target and SSD, while the second shows the projection onto the x-y plane (z is coming out of the page).

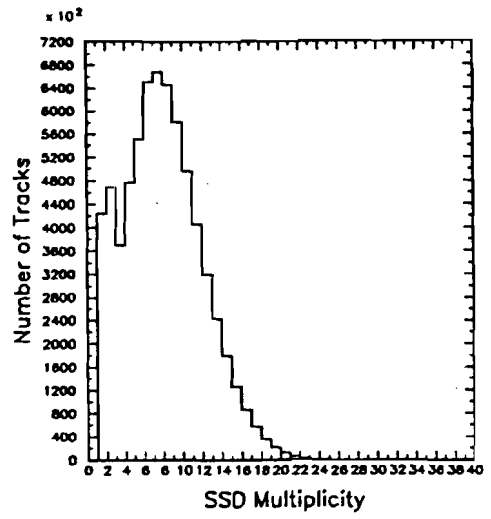

Figure 16: Typical SSD multiplicities. These are taken from various runs over the 1990 and 1991 run periods.

in the inner region, where there was a higher multiplicity of tracks, than in the outer region. The detector was theoretically capable of attaining a resolution for the vertex of about 10 microns in the x and y directions and 400-500 microns in the z (beam) direction.

Typical event topologies as seen by the SSD are shown in Figure 16, which shows the multiplicity of tracks sampled throughout the 1990 and 1991 runs. The microstrip detectors were found to be 96% efficient, with a 99% efficiency for reconstructing tracks with momentum of more than 10 GeV. The resolutions in the x and y directions of the SSD differed and were given by:

$$\sigma_x = 11\ \mu m \sqrt{1 + \left(\frac{17.5\,\mathrm{GeV}}{P_{<\mathrm{MCS}}}\right)^2} \tag{15}$$

$$\sigma_y = 7.7\,\mu m \sqrt{1 + \left(\frac{25.0\,\mathrm{GeV}}{P_{<\mathrm{MCS}}}\right)^2}, \tag{16}$$

where $P_{<\mathrm{MCS}}$ indicates the momentum (roughly about 5 GeV) below which the

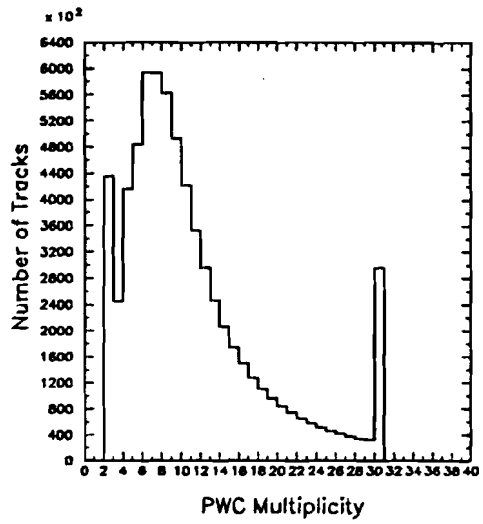

Figure 17: Typical PWC multiplicities.

track would be significantly effected by multiple coulombic scattering[44]. Multiple scattering effects were taken into account during the track fitting process. Detailed descriptions of this procedure exist elsewhere[45, 46] and will not be included here.

Proportional Wire Chambers and Tracking

The Proportional Wire Chambers (PWC's) were used to determine each particle's trajectory. Event multiplicities determined during the 1990-1991 runs by the PWC are shown in Figure 17[4]. The PWC's detected charged particles, and the amount of curvature that they exhibited revealed their momenta. The purpose of the PWC system is to measure the momentum of the charged particles produced in an interaction. Generally, the positions of charged particles passing through the PWC system were recorded after which the trajectory of the particle could be determined. This allowed a determination of the curvature of the charged particle

[4]These multiplicities correspond to the SSD multiplicities of Figure 16. If an event had more than thirty reconstructed tracks then the multiplicity was truncated to thirty. The trigger cuts out single charged tracks.

in a known magnetic field and from these data the momentum could be calculated. More specifically, the two large magnets, M1 and M2 (see Figure 10) had three sets of PWC planes placed between them (P0, P1 and P2), and two sets placed after them (P3, P4). These chambers, with their associated fitting algorithm, were capable of a spatial resolution of between 1.4% and 3.4% for a charged track with a momentum of 100 GeV. The resolution was dependent upon the nature of the track itself: higher momentum particles traversed the entire spectrometer (a 5-chamber track), while some lower momentum particles received enough of a deflection from M1 to leave the detector without entering into M2 (a 3-chamber track). Each of the five PWC's consisted of 4 planes, with x, y, U and V directions, where U and V were inclined at $\pm 11.6°$ with respect to y (see Figure 18)[5]. The size of the PWC's varied depending upon the location. P0 and P3, located just beyond each magnet, had the same size as the opening aperture of the magnets. P1 and P2 were matched to the acceptance of the spectrometer, while P4, originally the same size as P1 and P2, was reduced in size after the 1988 fire. Table 4 gives more of the specifications of the PWC's. The resolution of the PWC's was determined to be

$$\frac{\sigma_P}{p} = 1.4\% \left(\frac{p}{100\,\mathrm{GeV}}\right) \sqrt{1 + \left(\frac{23\,\mathrm{GeV}}{p}\right)^2}. \tag{17}$$

Particle Identification and Čerenkov Detectors

Partial particle identification was effected by the use of three Čerenkov detectors, labeled C1, C2 and C3 in Figure 10. The first two, C1 and C2, were placed between the two large magnets of the spectrometer while the third was placed after the second magnet (see Figure 10). Čerenkov detectors operate on the principle that a charged particle moving faster than the speed of light in a medium emits light (Čerenkov radiation). The Čerenkov detectors used in this experiment were multi-celled gas threshold devices, each of which contained a different gas. A particular

[5] Late in 1988 a fire erupted in Wideband, destroying much of the electromagnetic calorimeters, as well as some of P4. When P4 was rebuilt, only the x, y and U planes were used.

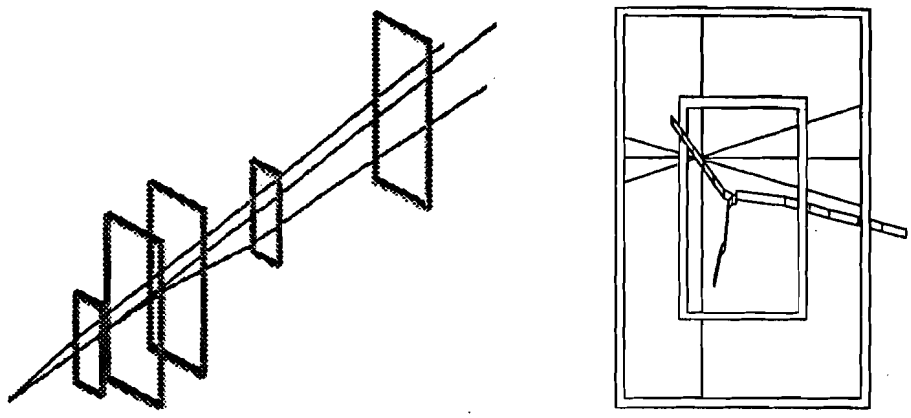

Figure 18: PWC Detectors, showing reconstructed tracks. The left shows a 3D view, while the right shows a projection onto the x-y plane (the beam direction, z, is coming out of the page). The solid straight lines in the second figure show the PWC wires of one plane registering hits. The track projections from the figure on the left are also shown in this figure.

Table 4: PWC configuration parameters. Note: P4 wires have an x separation of 2 mm , while y and U have 3 mm separations.

			total number of wires				
PWC	*Aperture* (cm^2)	*Wire Spacing*	x	y	U	V	*Total*
P0	76.2 × 127.0	2 (mm)	376	640	640	640	2296
P1	152.4 × 228.6	3 (mm)	512	832	832	768	2944
P2	152.4 × 228.6	3 (mm)	512	823	832	768	2944
P3	76.2 × 127.0	2 (mm)	376	640	640	640	2296
P4	101.6 × 152.4	2-3 (mm)	336	768	768	—	1872

Table 5: Čerenkov Particle Identification Information for reconstructed data.

ISTATP	*Identification*	*Momentum Range* (GeV/c)
0	Ambiguous	≥ 0.0
1	e definite	0.0 - 17.4
2	π definite	4.5 - 17.4
3	e, π ambiguous	4.5 - 61.7
4	K definite	16.0 - 44.5
6	π, K ambiguous	16.0 - 17.4
7	e, π, K ambiguous	16.0 - 44.5, 61.7 - 117.4
8	p definite	16.0 - 44.5, 61.7 - 117.4
12	K, p ambiguous	4.5 - 61.7
14	π, K, p ambiguous	0.0 - 17.4
15	total uncertainty	≥ 0.0

particle traversing the detectors would have a different momentum-dependent response in each. This allowed differentiation of e's, π's, K's and protons, although a degree of ambiguity often remains. Figure 19 and Table 5 show the extent to which the Čerenkov detectors employed in this experiment can distinguish between e's, π's, K's and protons.

The Čerenkov information was processed off-line during the reconstruction process. PWC track information was used to calculate the hypothesized Čerenkov radiation from a specific track, and this projected light was compared to the actual light yield from each of the Čerenkov detectors. The particle identification is described in Table 5 with the values of the descriptive variable ISTATP[44, 47]. The overall efficiencies for identifying K's and π's were 85% and 98% respectively[6].

[6]These efficiencies are determined from SROGUE – see Chapter 5.

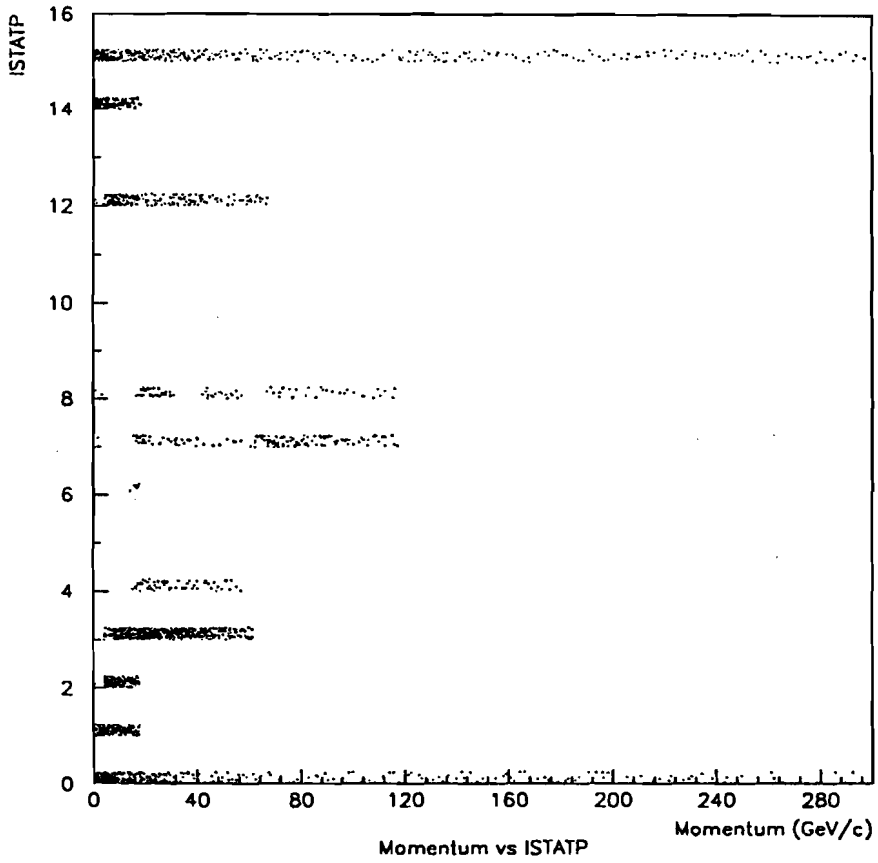

Figure 19: Momentum distribution for different levels of Čerenkov particle identification. This plot shows ≈ 50k events of all possible topologies. Refer to Table 4 for a description of ISTATP.

Calorimeters

E687 had two sets of calorimeters, one to measure the energy of electrons and photons (the electromagnetic calorimeters) and one to measure the energy of hadrons (the hadronic calorimeters). These devices measured the kinetic energy of each particle and worked in concert with the PWC and Čerenkov systems. In this analysis, the electromagnetic detectors were used primarily for eliminating spurious photons and electrons generated in an event while the hadronic calorimeters were used to remove neutral hadrons.

Electromagnetic Calorimeters (Inner and Outer)

There were two electromagnetic detectors. One was the large aperture Outer Electromagnetic shower counter (OE) placed after P2, on the upstream side of M2 (see Figure 10). The other was the Inner Electromagnetic shower counter (IE), placed downstream from P4 (see Figure 10). These detectors were used to identify electrons and photons and to reconstruct π°'s from their two photon decay.

The purpose of the OE was to detect electromagnetic particles that were the equivalent of 3-chamber tracks – namely those having low energy or wide production angles. The OE was a lead-aluminium scintillator shower detector made of 18.4 radiation lengths and of 1.8 interaction lengths overall and had an active area of 255 cm × 205 cm with an internal aperture of 51 cm × 88 cm. It was divided into 4 separate blocks in the x-y plane and had a square hole in the middle of the detector to allow noninteracting photons, e^+e^- pairs, and photons for E683 to pass through without interacting within the detector. The OE had an angular acceptance of 28 to 142 mrad in x, and 49 to 114 mrad in y. The energy resolution for an electron or a photon of energy 20 - 100 GeV was $(\Delta E/E)_{\mathrm{FWHM}} = 23\%/\sqrt{E}$.

The IE was an electromagnetic "catch-all" for almost any remaining neutral energy. As mentioned before, it was located behind P4. This allowed all other electromagnetic particles, aside from those that go down the beam line, to be measured. The IE had three sections, rather than the four of the OE. The active

area of the IE was 229 cm × 137 cm. It was made of lead and scintillating fiber and was upgraded from the 1988-1989 runs. The detector had an angular acceptance of 28 to 47 mrad. The energy resolution was $\approx 15\%/\sqrt{E} + 4\%$. The central beam hole of the IE was 5.1 cm × 5.1 cm.

Hadronic Calorimeters, (HC and CHC)

There were two hadronic calorimeters, the main Hadronic Calorimeter (HC) and the Central Hadronic Calorimeter (CHC). The purpose of these detectors was two-fold: first to act as a trigger which ensured that a hadronic interaction had occurred and secondly to reconstruct charged and neutral hadronic showers. These detectors were placed after the IE and before the inner muon detectors and iron shields. In addition to the total energy readout, the HC had a readout to find the transverse energy[48], which was found by independently summing the energy in each successive ring of the calorimeter. The energy in each ring was weighted by a predetermined calibration value and thus a transverse energy was determined.

The HC was a sampling calorimeter, made of 28 layers of 4.45 cm iron plates alternating with 28 layers of Iarocci tubes. The HC also had a hole in the middle matching that in the OE/IE. The active area of the HC was 304.8 cm by 203.2 cm, with an angular acceptance of 5 to about 30 mrad (see Figure 20).

The Central Hadronic Calorimeter (CHC) was also a sampling calorimeter made of 26 alternating layers of 5.08 cm iron and a total of 50 sheets of scintillating fibers[49]. It was modified from the 1988-89 run to accommodate the beam transport incorporated into E683. The original CHC description may be found in various E687 theses [45, 46, 50, 51]. The length of the detector was 128.0 cm and had a transverse area of 50.8 cm × 61.0 cm. The CHC was divided into two sections, leaving a split in the y direction. Depleted uranium, sheafed by 0.24 cm steel and interleaved with 0.635 cm scintillator made up the 6.4 interaction lengths.

The combined resolution of the HC/CHC $\approx 144\%/\sqrt{E}$[52]. For this reason it

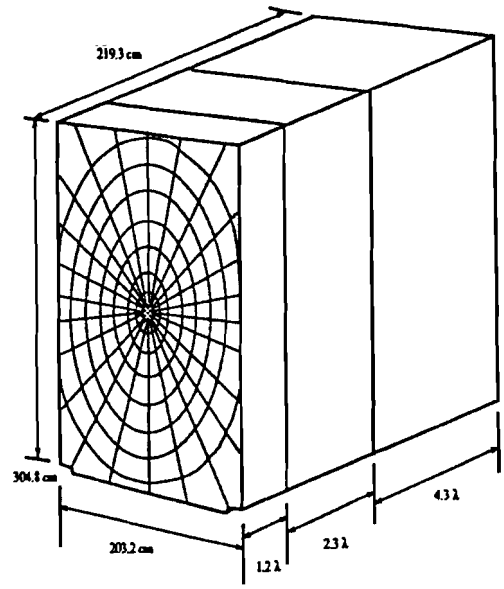

Figure 20: Schematic of Hadron Calorimeter, showing rings and segmentation of detector.

was only used to aid in the determination of total energies seen by the hadronic calorimeters and to differentiate hadronic from leptonic production.

Muon Detectors

The muon system was particularly important for the charm physics, especially for the semi-leptonic decay modes of the D. The muon system contained both scintillator planes and gas proportional tubes. The scintillator supplied a fast response for triggering and the gas tubes provided high spatial ($\sim$ 0.9 cm) resolution. The Outer Muon system was located directly behind M1, where the yoke of the magnet provided 10 interaction lengths of steel. The Inner Muon system was located at the end of the detector, behind additional layers of steel (121 cm and 60 cm). A more detailed description of these detectors may be found elsewhere[45, 46].

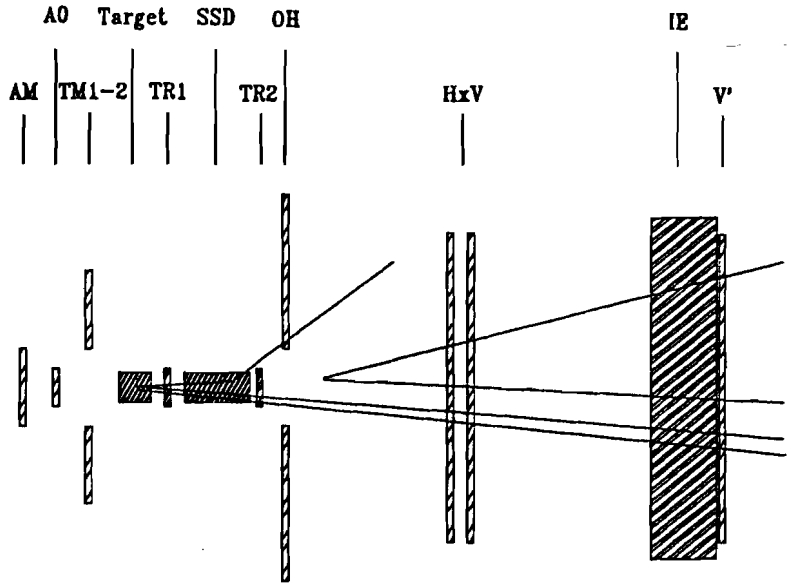

Figure 21: First Level (Master Gate) Trigger.

3.4 Triggers

Several triggering schemes were employed to maximize the number of events with final state hadrons while, at the same time, minimizing the number without hadrons. The First Level, or Master Gate Trigger, would only let data be processed if certain requirements from the systems with faster response times were satisfied. The Master Gate decided when the primary detectors should be read out and provided a period of time, or gate, in which to do this. During this interlude, such things as obtaining the readouts of the PWC information, setting latches (essentially a custom-built cache), and gating the ADC's (Analog to Digital Converter) were accomplished. The Master Gate sent the detector into a dormant state while the second level trigger made additional decisions about the event. The Master Gate required predetermined hodoscopes to receive a hit in order to proceed (see Figure 21). The full logic is represented by:

$$\mathrm{MG} = (\mathrm{TR1} \cdot \mathrm{TR2})\,[(\mathrm{H} \times \mathrm{V})_1 \cdot \mathrm{OH} + (\mathrm{H} \times \mathrm{V})_2]\,(\overline{\mathrm{A0} + \mathrm{AM} + \mathrm{TM1} + \mathrm{TM2}})\,.$$

The Master Gate consisted of two scintillators placed in the photon beam (AM and A0), two scintillators outside the photon beam line to reject muon beam halo (TM1 and TM2), and scintillators on either side of the SSD to make certain that there were tracks inside the target region (TR1 and TR2). The logic of the Master Gate required a charged track in the electron beam, no charged tracks in the photon beam, no muons accompanying the beam, and charged particles emanating from the target region. There was also a requirement that at least two charged particles from an event had to exist in the spectrometer. This was accomplished by requiring the inner hodoscope H×V to have either one charged particle when the outer hodoscope (OH) had at least one, or to register at least two charged particles with H×V. The H×V hodoscope, which was located just past P4, was a pair of crossed scintillators. Half way through the 1991 run, a second V hodoscope, V′, was placed in the detector to improve the efficiency of the trigger. The OH was a layer of scintillator in front of the OE. These hodoscopes were divided along the y direction so as to avoid triggering on e^+e^- pairs[7].

The veto on unwanted events was enhanced roughly a factor of 20 by including an additional Second Level Trigger. The Second Level Trigger utilized many slower detectors (hence these were not in the Master Gate) and was accommodated by the Master Gate, which extended the dead time an additional 2.4 μs. The second level trigger required that at least one hit occurred in P0 outside the e^+e^- pair direction, that more than 35 GeV of energy was deposited inside the HC, and that there was a valid RESH response. If the event was acceptable, the second level trigger delayed the access of other events until the complete event data acquisition took place - such as digitization of the ADC's and transfer into and out of buffers. If the event did not satisfy all the criteria, a fast clear of all segments occurred and the inhibit on data taking was released. The second level trigger logic could be changed to accommodate different "trigger sets", and this was done for different

[7]The magnets deflected oppositely charged particles in the vertical direction and were not spread much more than the size of the photon beam in the horizontal direction. A gap the size of the photon beam was therefore placed in the OH in order not to trigger on e^+e^- events.

runs in the experiment.

3.5 Data Acquisition

The E687 data acquisition system incorporated several hardware and software systems. The output channels of pulse heights were temporarily stored in a large buffering system and then written to tape. The readout from the PWC's went into LeCroy 4291B Camac TDC's, the calorimeter readouts went through LeCroy 1885 Fastbus ADC's, and the SSD readout went into a specially built University of Milan MIDA ADC. In addition, latches were set up by Fermilab and the University of Illinois to record trigger hits, data from muon counters, and busline logic signals.

During a spill the data acquisition system was clocked. If an event satisfied the triggering criteria, a gated signal was initiated to allow time for the digitization of the data from the spectrometer. This process required about 300 ns, and an additional veto signal of about 1 μs inhibited any other triggers from firing.

If the Master Gate was satisfied, the signals were stored locally in the buffers of the electronics while the second level trigger output was examined. If no second level trigger was forthcoming during the Master Gate veto, the event was cleared. If the second level trigger was satisfactory, the data was read into and stored in LeCroy 1892 Fastbus Multiple Record Buffer Memory modules and a University of Illinois memory module. Until all the data was flushed out, any subsequent data taking was inhibited. The data was moved with "PANDA", a specialized data acquisition system run on a local DEC Vax. This system included automation of the tape handling (2 GB Excabyte 8 mm Tapes), Camac controls of high voltage settings, and generation of pedestals (readouts with no radiative source to find a "zero" value).

In addition, constant control of data quality was monitored with several programs that checked in real time the average operation of the detector. There were also several programs that monitored specific detection systems. All of the on-line

monitoring systems were accessible with a UNIX Hoist, so several Sun and DEC workstations could also run the on-line software.

Finally, a simple database system kept account of ADC pedestal information (recorded roughly once or twice a day), as well as any geometrical changes in the detector subsystems. This information, along with a map of the magnetic fields of the two magnets, was maintained in several data files available on whichever computer system the analysis was run.

Data "Reduction"

Since the only data recorded were the raw hit information, it was necessary to convert this into a usable form. This process involved a few members of the collaboration running computer "farms" continuously for several months using reconstruction programs on the 1990 – 1991 data sets. The farms were fashioned from several RISC based UNIX workstations running under CPS (Cooperative Processes Software, an extension of APS, Advanced Computer Program, which were both efforts developed at Fermilab[53]). The workstations were connected by a Local Area Network (LAN) and provided single-code multiple-data (SCMD) architecture on a large grained, loosely coupled parallel system. The event reconstruction ran essentially as diagrammed in Figure 22. The farms were comprised of both SGI and IBM 6000's, as configured in Figure 23.

The reconstruction process employed (called Pass1) converted the raw data from the approximately 500 million triggered events into kinematic variables that were subsequently used in the analysis. This process took approximately 4 months for the 1990 data set (run primarily on 3 farms) and 6 months for the 1991 data set (5 farms). Serial processing of the raw data would have taken an estimated 700 Vax 11/780 equivalent years. The 1990 data set incorporated a simple relational database to track the progress of the reconstruction, while the 1991 data set used ORACLE, a professional relational database.

The 1990 data set had 275,016,917 events read in, and 204,259,613 events

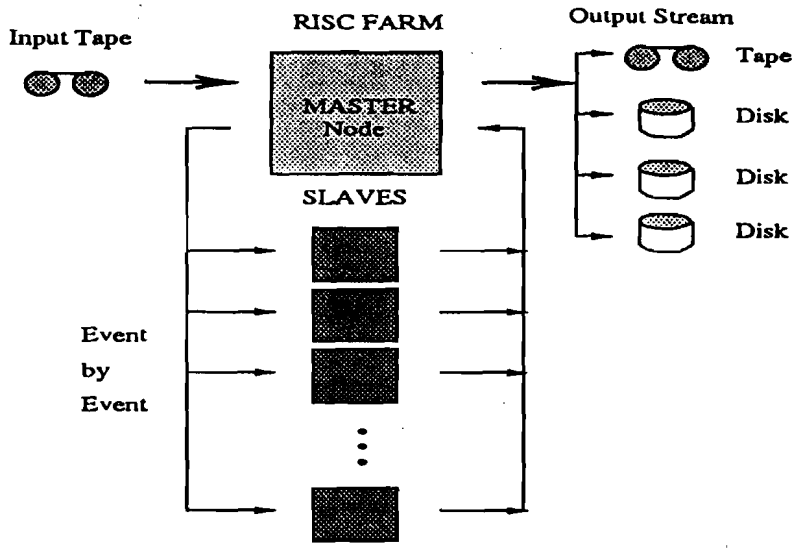

Figure 22: Event reconstruction using SCMD on FNAL UNIX farms.

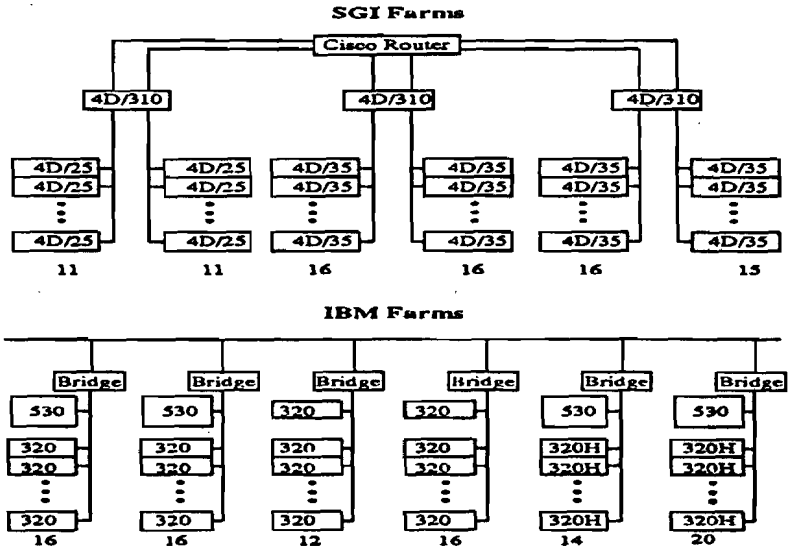

Figure 23: Schematic of the Silicon Graphics (SGI) and IBM 6000 (IBM) farms, indicating the number of nodes on each farm.

written out. The corresponding numbers for the 1991 data set were 211,030,666 events read in and 160,628,066 events written out. Thus roughly 25% of the data was lost in the reconstruction process. An additional skim process was carried out to reduce the data sets onto fewer tapes and to write out smaller data records. Three preliminary skims were run: the MOM skim, the QT skim, and the TINY skim. The MOM skim wrote out most of the major records for each detector system. The QT skim used a much smaller set of records, and the TINY skim used only two. The QT and TINY skims also employed specific physics cuts. The principal cut in the QT tapes that would effect this analysis was a $\phi(1020)$ mass cut ($m_{K^+K^-} \leq 1.1$ GeV). A subskim was run with the QT skim in order to reduce the number of events and is summarized in Tables 6 and 7.

Data Reconstruction

The track reconstruction programs treated the SSD and PWC tracks individually and attempted to link them together. The tracks were then analyzed to see if they shared a common vertex with any other tracks or if any "kinks" where present, or whether any secondary vertices from either charged or neutral (vee) decays occurred. Secondary vertices and "kinks" for the most part represented weak decays of various elementary particles which would not be found in events of interest in this analysis. This analysis used positive evidence for the presence of a kink or vee as a veto.

SSD Reconstruction

The SSD track reconstruction was rather straightforward. Because there was no magnetic field in this region of the detector, the individual hits in the SSD planes were matched and fitted to a straight line. The SSD fitting algorithm employed a means of discerning isolated hits from shared hits. Clusters of up to three hits distributed across three cells were analyzed. If they were resolved as two tracks the centroid of the hits was placed on the centerline between the strips. A

Table 6: The various cuts used for the event selection. The table lists the number of events in the 1990 and 1991 data runs.

Cut	*Description*	1990 *Data* (67 *tapes*)	1991 *Data* (65 *tapes*)	*Combined* (132 *tapes*)	%
	Total Triggers Written	275,016,917	211,030,666	486,047,583	—
	Survived Pass1	204,259,613	160,628,066	364,887,679	—
1	QT Events Read	73,843,267	68,494,377	142,337,644	100.00
2	PWC: 2, 3 tracks	8,949,012	5,650,140	14,599,152	10.26
3	SSD: 2, 3 tracks	4,090,394	2,599,790	6,690,184	4.70
4	1 SSD or PWC Vertex	4,090,394	2,599,790	6,690,184	4.70
5	No Reconstructed "V"	3,891,663	2,371,994	6,263,657	4.40
6	No Reconstructed Kink	3,891,663	2,371,994	6,263,657	4.40
7	Charge: $2\pi \rightarrow 0$, $3\pi \rightarrow \pm 1$	3,464,731	2,121,301	5,586,032	3.92
8	z in Target	1,989,621	1,908,336	3,897,957	2.74
9	Tagged > 0.0 GeV	1,925,779	1,591,696	3,517,475	2.47
10	RESH > 40.0 GeV	692,645	738,359	1,431,004	1.01
11	$E_\gamma \geq 0.0$ GeV	538,012	640,167	1,178,179	0.83
12	HC+CHC > 5.0 GeV	262,591	391,694	654,285	0.46
14	Čerenkov not e^-	165,610	226,903	392,513	0.28
15	All linked tracks	132,376	187,637	320,013	0.23
16	No Doubly Linked Tracks	85,715	123,347	209,062	0.15

Table 7: Final data sample of skimmed events (the final entry of the previous Table) for the $\rho(770)$, $\phi(1020)$, $\rho'(1600)$ and the $a_2(1320)$, $a_3(2050)$ samples.

Combined Data	2 *Track Data*	3 *Track Data*
209,062	119,699	89,363

pattern recognition search was then employed, which extended hits along the three projected coordinates. The pattern required at least three of four projections, and a χ^2 fit was used to make a cut. Finally, the projections were formed into a three dimensional spatial array.

PWC Reconstruction

The PWC tracks represented a special problem, not only because the trajectories of the particles in this region were curved due to magnetic fields, but also because not all the tracks traversed the entire detector. 5-chamber tracks, extending through the entire length of the detector, may or may not have been linked to the SSD. The same is true for tracks passing through only three chambers. Tracks may also have extended from the target region to the first three sets of PWC planes but left the detector without entering into the second half of the detector.

Linking Tracks

After the tracks were established with the SSD and PWC fitting procedures, they were compared with each other to see if they matched. The PWC tracks were projected onto the bend plane of M1 in order to compare them with SSD tracks. A search was performed to match slopes and intercepts for every track in an event, and those that were found to match within a certain tolerance were refit using all SSD and PWC information. Three chamber hits from the PWC were excluded because they did not present enough information to project through either side of M1 or M2. If the global refit met a strict χ^2 criterion, the new linked fit was used. This method was useful in identifying e^+e^- pairs, as they would likely have a single SSD track matched to two PWC tracks.

Vertexing

The vertex of the event was determined by the SSD track projections into a single point. If no SSD vertex could be found, the center of the target was used as the

vertex. If only a single SSD vertex was found, it was employed as the primary vertex. If several SSD vertices were found, the farthest upstream with at least one linked track was used. Any further vertices were run through a "stand-alone vertexing routine" to determine the type of vertex. This procedure was used to find neutral strange and charm particle decays and had little impact on this work (all multivertex events were excluded from this analysis).

Electromagnetic Showers

The neutral Electromagnetic shower reconstructions were crucial for finding π°'s and eliminating electrons from the pion spectrum. Shower reconstruction involved looking at individual showers in the Inner and Outer Electromagnetic Calorimeters. First, showers were eliminated from PWC tracks using a proximity cut based on track location and initial shower position. Isolated showers were then further analyzed for possible π°'s, while showers associated with tracks were used to determine the type of track in the calorimeter, if possible. The IE code generated a track hypothesis by finding the actual hit in the IE strips weighted by their energy and corrected for the transverse profile of the shower. The transverse and longitudinal energies were then passed to two separate discrimination functions which distinguished noninteracting pions and electrons from interacting ones. The OE determination worked in a similar way.

Chapter 4

Data Analysis

4.1 The Beam and Its Characteristics

Figure 24 shows the characteristics of the tagged electron beam, the RESH energy response[1], the BGM/BCAL energy, and the interacting γ energy. These events are taken from the two- and three-track data sample and have an average energy of 130.7 GeV[2]. If the total energy of the event as measured by the PWC system exceeds that deduced from the Tagging system measurement, we adopt the former for the interaction energy.

The "scalar" measurements depicted in Figure 24 suffice to determine the beam energy. Many useful kinematic quantities, however, require knowledge of the beam direction as well. In this experiment we determine only the average beam direction which was found in the following way:

- The x and y projections of the charged tracks were recorded at two well separated values of z in the detector. These projections were summed on an event by event basis and averaged over the entire data set.

[1]These are "skimmed" events, and the cut of 40 GeV on the RESH energy removes a small degree of pile-up in the 40 GeV bin. The digitization of the RESH is clearly evident.

[2]The interacting energy had an RMS (Root Mean Square) of 62.31 GeV, while a Gaussian fit yielded an energy of 126.8 ± 0.3 GeV with a width of $45.31 \pm .15$ GeV.

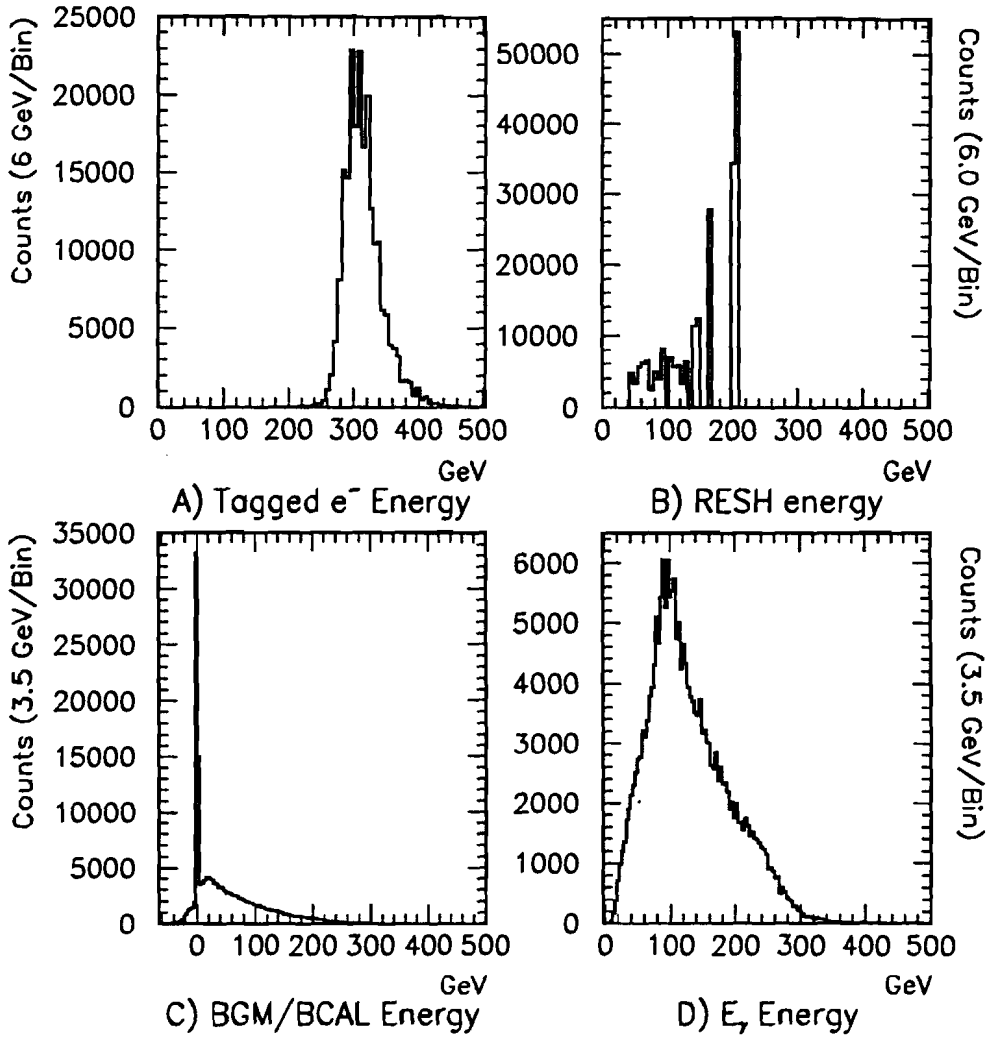

Figure 24: The quantities used to measure the beam energy: A) The energy of the Tagged e^-. B) The recoil energy of the e^- as measured by the RESH. C) The noninteracting energy measured by the BGM/BCAL. D) The energy of the Interacting γ.

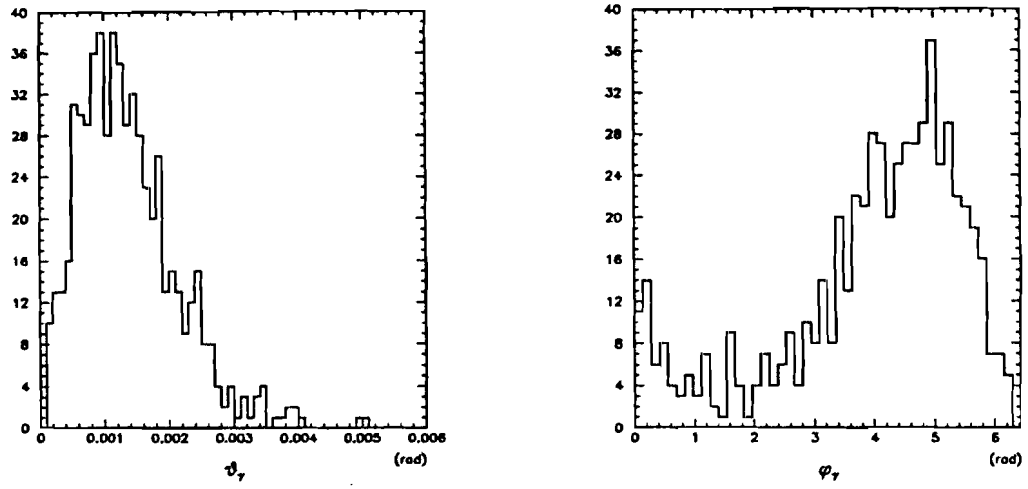

Figure 25: The sum of the residuals from a run by run basis. The values of the correction are $\theta_\gamma = 0.913$ mrad and $\phi_\gamma = 3.943$ rad.

- The angular variables θ and ϕ were calculated according to:

$$\phi = \tan^{-1}\left(\frac{y}{x}\right) \tag{18}$$

and

$$\theta = \tan^{-1}\left(\frac{\sqrt{y^2 + x^2}}{z}\right). \tag{19}$$

- The averaged θ and ϕ were assumed to point back into the direction of the incident interacting γ.

- Only events from runs having more than 100 events were kept.

The averaged values for θ and ϕ for each accepted run are shown in Figure 25. The mean value of the averaged values is chosen as the mean direction of the photon beam.

4.2 Mass Errors

Errors in the calculation of the mass of the $\pi^+\pi^-$, K^+K^- or $\pi^+\pi^-\pi^\pm$ systems arise from the finite resolution of the detector. The method for ascertaining the mass error is as follows. A 2×2 or 3×3 covariant matrix is formed for each reconstructed track. Since each track is found individually, no cross-terms are involved for the errors on the tracks. An error matrix is created with the form:

$$E_{\text{Mass}} = \begin{vmatrix} E_{\pi^+} & 0 & 0 \\ 0 & E_{\pi^-} & 0 \\ 0 & 0 & E_{\pi^\pm} \end{vmatrix}. \tag{20}$$

The E_π submatricies are 3×3 covariant matricies formed for each track. The elements of the submatricies are the square of the errors on the slopes at the target: $\Delta x = x'$, $\Delta y = y'$, and the momentum error. The SSD vertexing algorithm is used to determine the slope errors, and the PWC's were used for the momentum measurements[45]. The E_π matricies then assumed the form:

$$E_\pi = \begin{vmatrix} \sigma^2_{x'} & \sigma_{x'y'} & K\sigma_{x'y'} \\ \sigma_{y'x'} & \sigma^2_{y'} & K\sigma_{y'y'} \\ K\sigma_{x'y'} & K\sigma_{y'y'} & \left\{ \begin{array}{c} [\sigma^2_P]_{5\ Chamber} \\ \text{or} \\ \left[K^2(\sigma^2_{\delta y'})\right]_{3\ Chamber} \end{array} \right\} \end{vmatrix}, \tag{21}$$

where the K is an additional term due to the poor resolution of 3-chamber tracks ($K = \frac{P^2}{\text{M1}_{kick}}$), and is set to zero for 5-chamber tracks. The $\sigma^2_{\delta y'}$ term arises from the extra kick the track receives from M1. The error on the mass is then

$$\sigma^2_{\text{Mass}} = D^T E D, \tag{22}$$

where

$$D = \left(\frac{\delta^2 E}{\delta x^2}, \frac{\delta^2 E}{\delta y^2}, \frac{\delta^2 E}{\delta p^2}\right) \tag{23}$$

is the vector defined by the derivatives of the mass with respect to x', y', and momentum.

The spread of the mass errors for the three channels may be seen in Figure 26. The resolution of the $\pi^+\pi^-$ channel is approximately 6 MeV, while the resolution in the $\pi^+\pi^-\pi^\pm$ channel is roughly 1.3 times as great. The resolution of the K^+K^- ($\sim$ 2 MeV) channel exceeds both of the pion channels since only positively identified Čerenkov tracks are used.

4.3 Final Sample Selection

After the final skim had been performed on the data set, additional cuts were made to increase the reliability of the sample[3]. These include:

1. Elimination of duplicate events and any events from calibration runs.
2. Matching the number of PWC tracks to the number of SSD tracks.
3. Elimination of events with reconstructed neutral showers.
4. Partial or full identification of each track from Čerenkov information.
5. Imposition of an opening angle requirement such that this angle exceed 7.5 mrad.
6. Use of a t' cut (this criterion is not always applied but will be emphasized when it is).

The results are summarized in Table 8. The opening angle cut is employed to differentiate $\pi^+\pi^-$ pairs from e^+e^- pairs. The angle is formed by taking the dot product of the laboratory track trajectories. The e^+e^- events have an extremely small opening angle, so that within an opening angle of 7.5 mrad there is a large

[3]These cuts are performed during the analysis, and no distinction is made between $\pi^+\pi^-$ events and $\mu^+\mu^-$ events until mass plots are made.

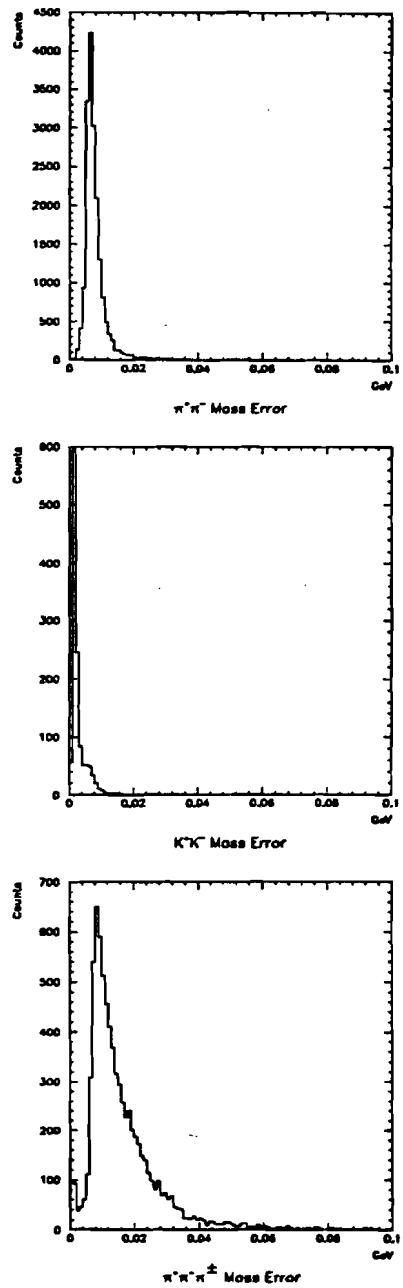

Figure 26: The mass errors in the $\pi^+\pi^-$, the K^+K^- and $\pi^+\pi^-\pi^\pm$ channels from the final event selection.

Table 8: Final cuts for the data sample.

Final Data Samples				
Selection	$\pi^+\pi^-$	K^+K^-	$\mu^+\mu^-$	$\pi^+\pi^-\pi^\pm$
Initial Number	127,641	127,641	127,641	86,392
No Duplicate Events	119,022	119,022	119,022	30,694
PWC = SSD	82,402	82,402	82,402	30,694
No γ's	65,531	65,531	65,531	24,447
Čerenkov	50,244	4704	50,244	7981
$\theta_{-,+} \geq 7.5$ mrad	46,670	—	46,670	6421
t'	18,363	1229	9451	1856

amount of e^+e^- contamination. The effect of the opening angle cut may be seen in Figure 27, which shows the data sample before and after the opening angle cut.

4.4 The $\pi^+\pi^-$ Channel

Mass and t' Distributions

The dipion mass spectrum for the $\pi^+\pi^-$ channel is shown in Figure 28 where only events for which t' lies between 0.015 and 0.2 GeV^2 are included. The data which are dominated by the $\rho(770)$ are fit twice: once with a Breit-Wigner alone, and once with a Breit-Wigner supplemented by the extra terms suggested by Söding (the Drell and Interference terms, as mentioned in the second chapter) for a photoproduced ρ. Both fits utilize a fifth order polynomial background. The latter description of the data yields a mass of 767.5 ± 1.1 MeV and a width of 172.4 ± 5.5 MeV. These values are in much better accord with the values given by the PDG[9] than when the data are fit to only a Breit-Wigner. The pure Breit-Wigner fit gives a $\rho(770)$ mass of 719.3 MeV and width of 193.5 MeV which are quite inconsistent with the known parameters of the $\rho(770)$. The various terms of the fit

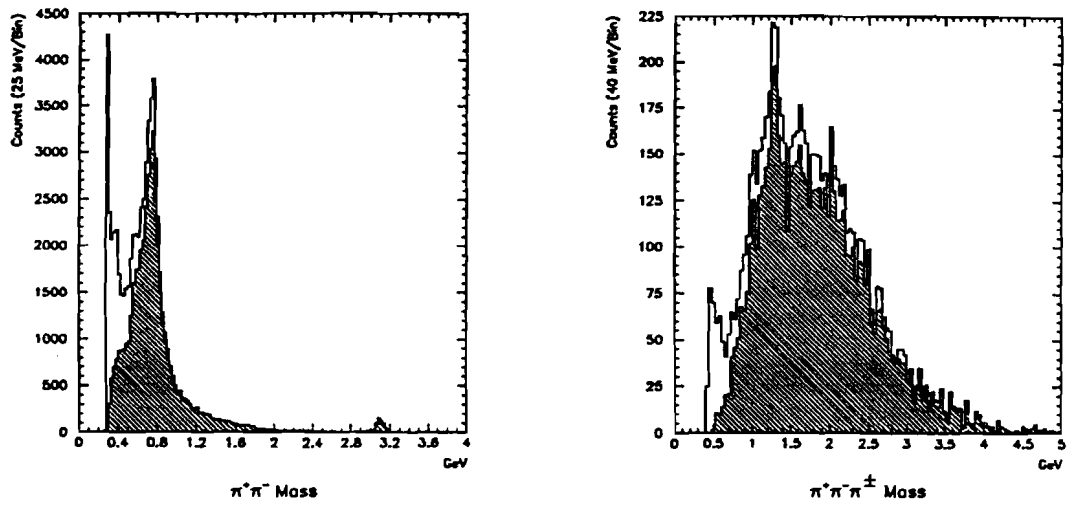

Figure 27: The mass spectrum of the $\gamma N \rightarrow \pi^+\pi^- N$ (left) and $\pi^+\pi^-\pi^\pm$ (right) channels. The unhatched histograms show all the data, while the hatched histograms show those events that satisfy the opening angle requirement.

in the Söding description are listed in Table 9. Both fits are hampered by the presence of Bethe-Heitler dimuon pairs, which form a background to the $\rho(770)$ in the low mass region. The decay of the $\phi(1020) \rightarrow \mu^+\mu^-$ can be seen between the $\rho(770)$ and $\rho'(1600)$. The $J/\psi(3097)$ also appears in this plot, presumably through the misidentification of muons as pions. The Bethe-Heitler dimuon background decreases with increasing mass, essentially as a decaying exponential[54], and will not effect the events above 1.5 GeV.

The polar decay angular distribution for the $\rho(770)$ in its helicity frame is shown in Figure 29. The raw data are shown in the left hand histogram while the right hand histogram shows the spectrum after correction for the acceptance presented by our experimental apparatus. This correction will be described in Chapter 5. The events included in Figure 29 have the same selection criteria as those in Figure 28, except their invariant mass is restricted to the ρ region ($600 \leq M_{\pi\pi} \leq 900$ MeV). The events for Figure 29 have the same requirements as those in Figure 28, though

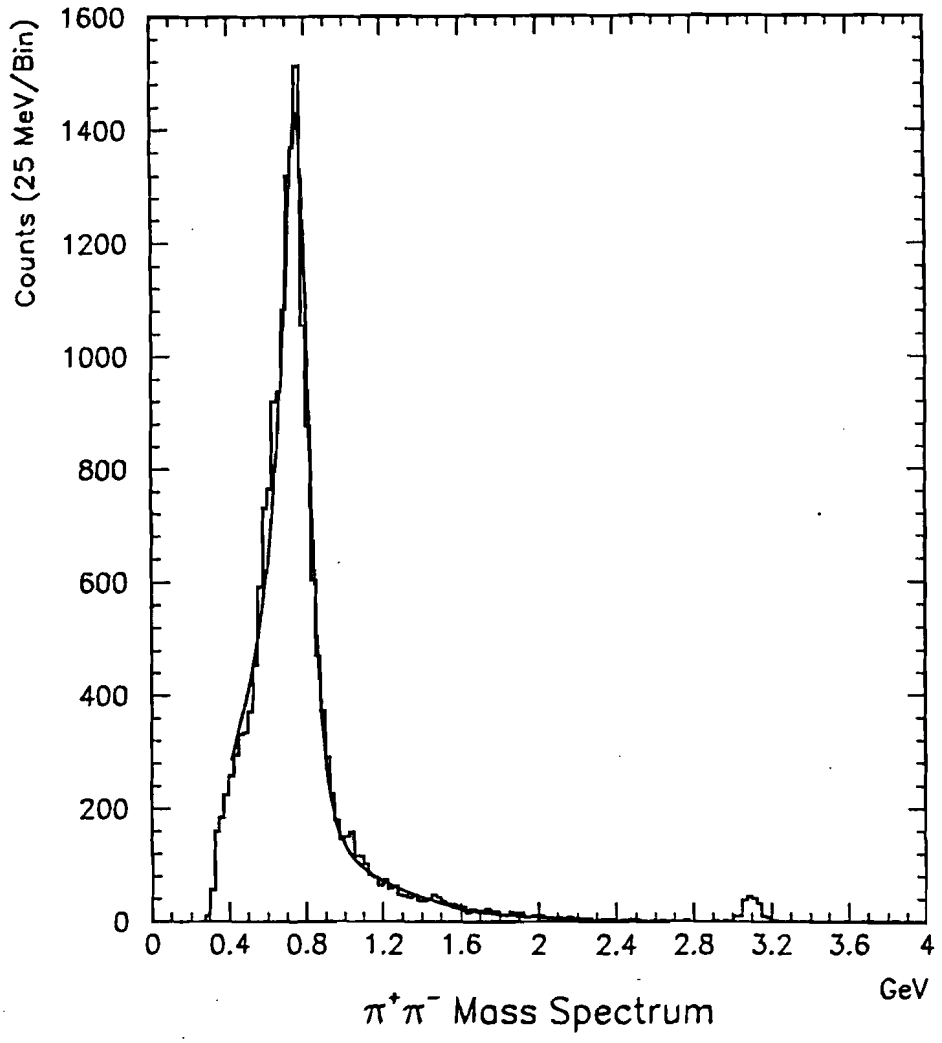

Figure 28: The $\gamma N \rightarrow \pi^+\pi^- N$ channel, exhibiting the $\rho(770)$ enhancement in the 0.7-0.8 GeV range. Note the skewed $\rho(770)$, a peak around 1.02 GeV ($\phi(1020) \rightarrow \mu^+\mu^-$ misidentified as $\pi^+\pi^-$), the $\rho'(1600)$, and the $J/\psi(3097)$ (from $J/\psi(3097) \rightarrow \mu^+\mu^-$ with μ's misidentified as π's).

Table 9: Fit results for the $\rho(770)$. The lower table only shows the values of the acceptance corrected data.

Söding $\rho(770)$ Fit Parameters				
f_{BW}	f_{Drell}	f_{Int}	Mass (GeV)	Width (GeV)
166.5 ± 1.66	75.69 ± 0.75	65.23 ± 1.27	0.7675 ± 0.0011	0.1724 ± 0.0053

Helicity Angle Fit $(A + B(1 - \cos^2\theta))$	
Constant (A)	Quadratic (B)
3540.3 ± 127.8	89840.1 ± 217.4

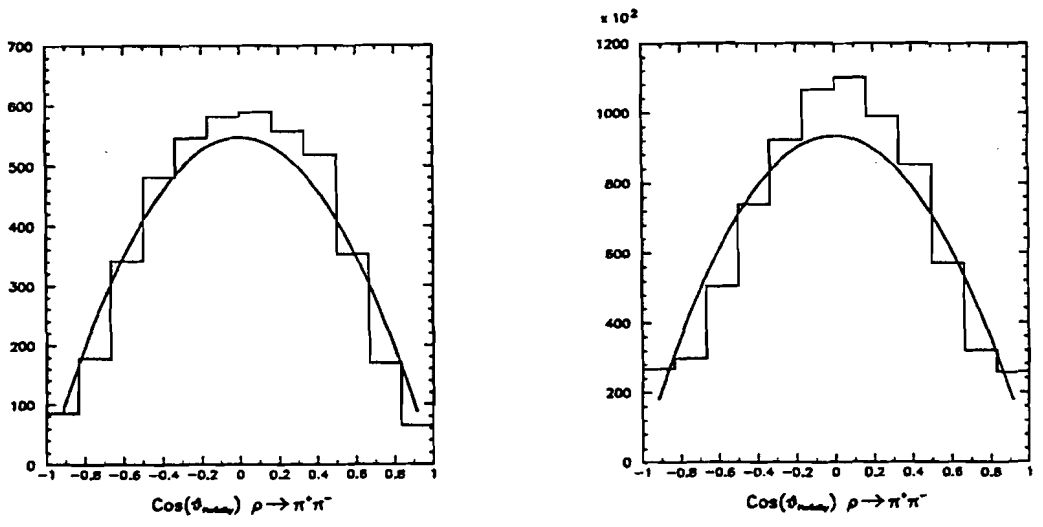

Figure 29: The decay angular distribution for the $\rho(770)$ in its helicity frame. The left histogram contains uncorrected events while the histogram on the right shows the same events corrected for detector acceptance. The smooth curve shows the $\sin^2\theta$ distribution of a $J^{PC} = 1^{--}$ meson with relatively little background.

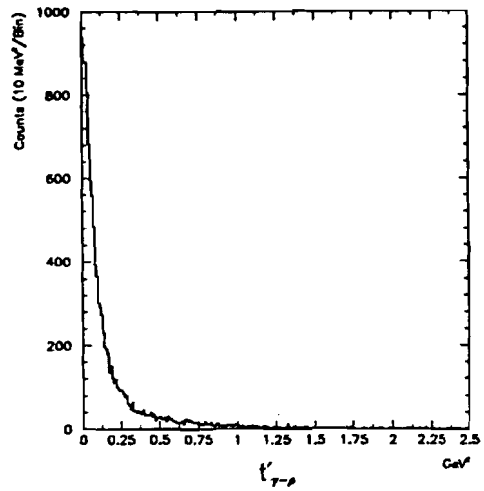

Figure 30: The t' distribution of the $\rho(770)$.

the events are constrained to have an invariant mass between 600 and 900 MeV. The fit is with a quadratic of the form $(A + B(1 - \cos^2\theta))$ using the values listed in Table 9. The overall shape shows a $\sin^2\theta$ distribution, which is indicative of the decay of a particle with $J^P = 1^-$ which is polarized in the z direction ($J_z = \pm 1$).

Figure 30 shows the t' distribution for the events in the $\rho(770)$ mass region which demonstrates the peripheral nature of the photoproduced $\rho(770)$. The best fit of this t' distribution is with an exponential function $e^{-b|t'|}$ with b $= 9.18 \pm 0.14/\text{GeV}^2$. This value is reasonably consistent with previous results (a value of $t' = 7.5/\text{GeV}^2$ was found at 20 GeV[30]).

The $\rho'(1600) \rightarrow \pi^+\pi^-$

The dipion mass spectrum for the mass region $1.0 \leq M_{\pi\pi} \leq 2.0$ GeV is shown in Figure 31. The fit shown employs a Breit-Wigner resonance for the $\rho'(1600)$ over a double exponential background. The parameters from this fit for the mass and width of the $\rho'(1600)$ are 1.489 ± 0.073 GeV and 0.195 ± 0.004 GeV respectively.

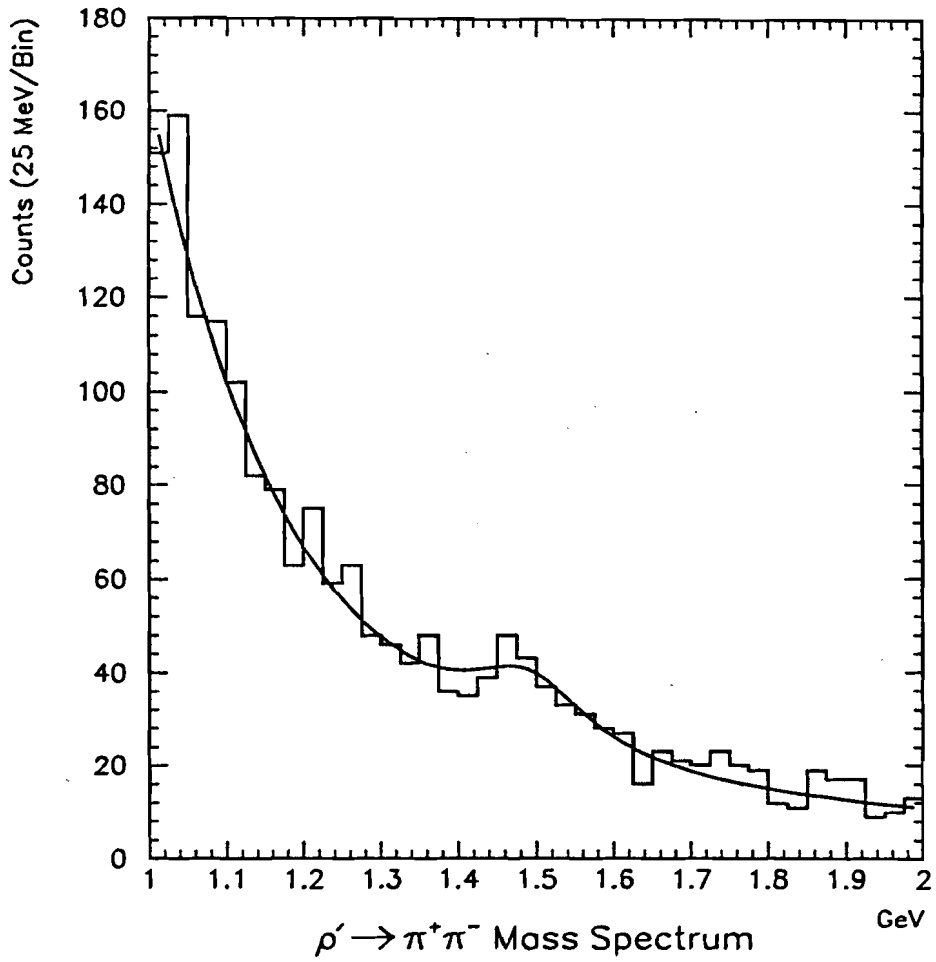

Figure 31: The $\gamma N \rightarrow \pi^+\pi^- N$ channel, exhibiting the $\rho'(1600)$ enhancement in the 1.450-1.700 GeV range. The mass is 1.498 GeV with a width of 0.198 GeV.

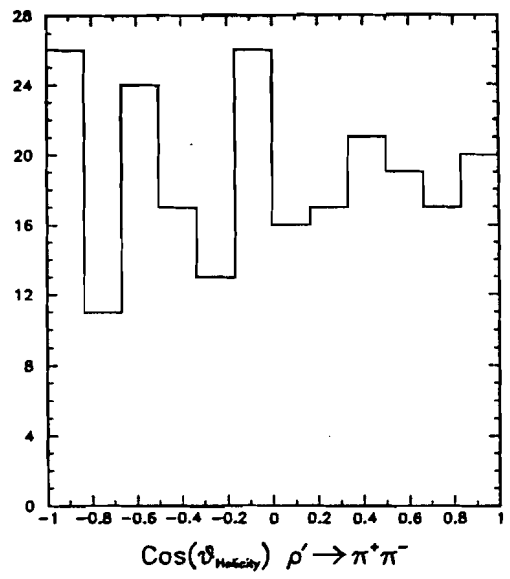

Figure 32: The $\rho'(1600) \rightarrow \pi^+\pi^-$ helicity angle distribution.

The mass is somewhat lower than the average given in the PDG[9], but consistent with the analysis of Donnachie and Mirzaie[55]. The $\rho'(1600)$ helicity polar angular distribution is shown in Figure 32. The fact that the $\rho(770)$ has a relatively large width and is produced copiously in photoproduction implies that the high energy tail of the $\rho(770)$ can distort the $\rho'(1600)$ decay angular distribution. The effect of this background in the $\rho'(1600)$ region and the presence of Bethe-Heitler dimuons together with the small $\rho'(1600)$ signal makes interpretation of this angular distribution uncertain. For that reason, neither an acceptance correction nor a fit is applied.

Table 10: Fit values for the $\phi(1020)$.

$\phi(1020) \rightarrow K^+K^-$ Fit Parameters		
Amplitude	Mass (GeV)	Width (GeV)
0.8507 ± 0.0474	1.0201 ± 0.0002	0.0063 ± 0.0003

4.5 The K^+K^- Channel

As was mentioned in the third chapter, the so-called QT tapes used in this analysis required the effective mass of any K^+K^- pair to be less than 1.1 GeV. Because of the excellent resolution in this channel, we can still study the photoproduction of $\phi(1020)$ mesons in a bias free manner. In order to do this we impose the most stringent Čerenkov identification criteria that is available for Kaons (ISTATP = 4, 12). The resulting mass spectrum is shown in Figure 33. The fit, represented by the smooth curve in Figure 33, is a Breit-Wigner with a quadratic background. The parameters of the fit are listed in Table 10. The acceptance corrected polar angular distribution in the $\phi(1020)$ helicity frame (with the $\phi(1020)$ defined as $1.0125 \leq M_{KK} \leq 1.0250$ GeV) is presented in Figure 34. The smooth curve represents a $\sin^2\theta$ distribution which would be expected for s-channel conserving $\phi(1020)$ events. While the fit is not good, it would appear that most of the $\phi(1020)$ signal does have $J = 1$. The t' distribution (Figure 35) for those events in the $\phi(1020)$ mass region shows the diffractive nature of $\phi(1020)$ photoproduction. A fit of this distribution to a decreasing exponential $e^{-b|t'|}$ gives a value of $b = 8.38 \pm 0.63$ GeV^{-2}.

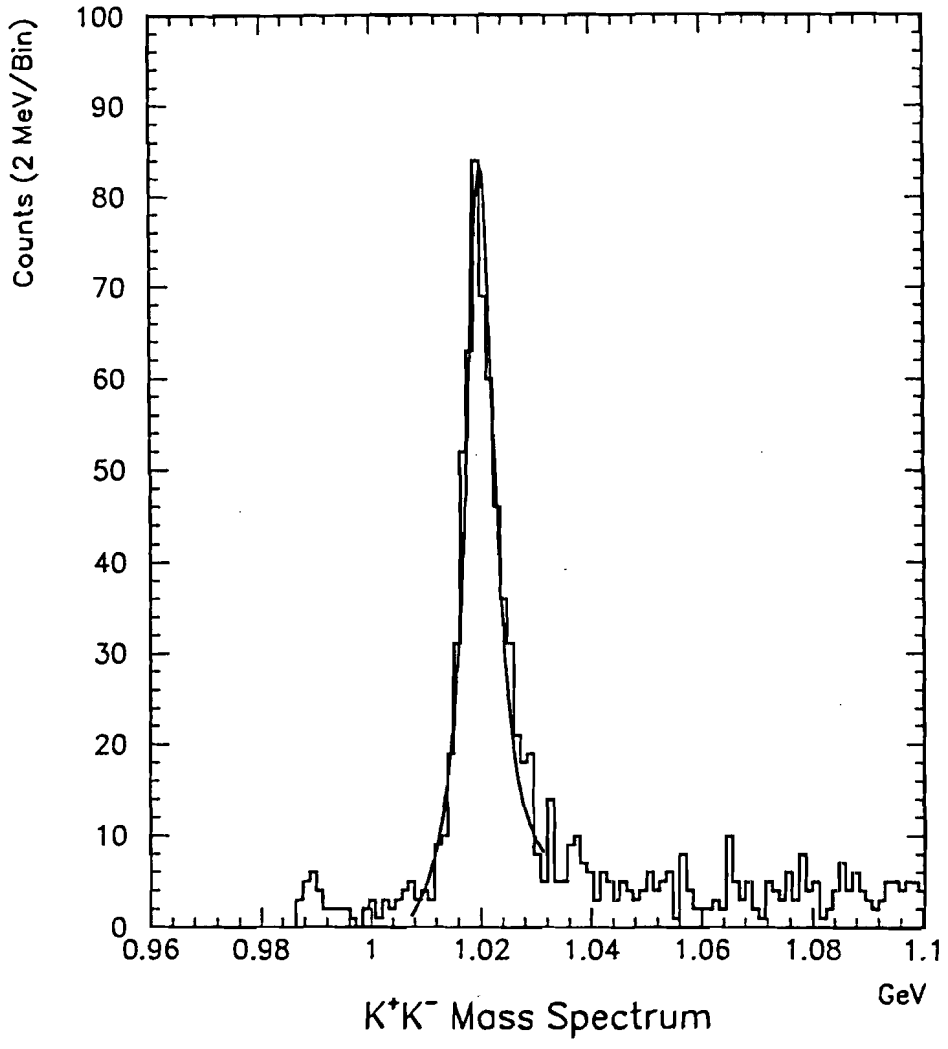

Figure 33: The K^+K^- mass distribution. The events are restricted to those for which both Kaons are positively identified. These events are also restricted to the t' region $0.015 \leq t' \leq 0.2$ GeV^2.

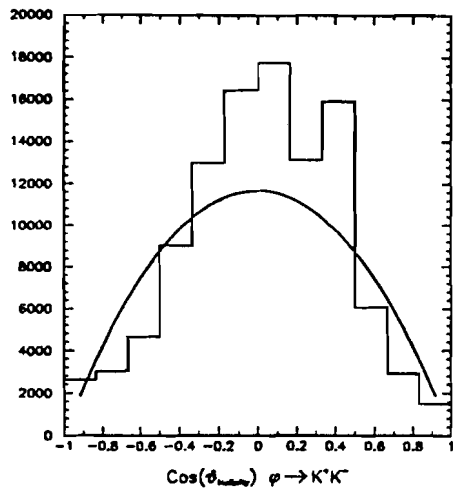

Figure 34: The polar decay angular distribution for the $\phi(1020)$ in its helicity frame. The histogram has been corrected for acceptance.

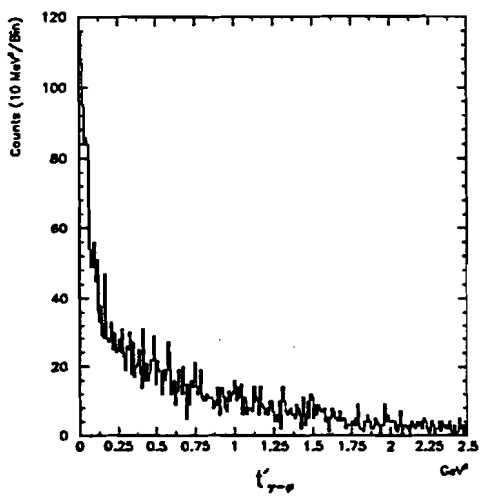

Figure 35: The t' distribution of the $\phi(1020) \rightarrow K^+K^-$.

4.6 The $\mu^+\mu^-$ Distribution

In this section we shall investigate the $\mu^+\mu^-$ mass spectrum. Muon tracks are identified by requiring at least one track to register in either of the muon detectors. The appearance of a strong $J/\psi(3097)$ signal in the "dipion" mass spectrum indicates that there was some contamination in the dipion spectrum from $\mu^+\mu^-$ events and could not possibly account for the signal that is observed. This follows since the $J/\psi(3097)$ decay into $\pi^+\pi^-$ is relatively weak (0.0147%)[9]. Figure 36 shows the invariant $\mu^+\mu^-$ mass. The full histogram indicates those events where the Muon Chambers identified at least one of the particles as a muon, while the hatched area indicates events where both were identified as muons. Both sets of events were required to have t' between 0.015 and 0.2 GeV^2. The low mass (≤ 1.5 GeV) region of Figure 36 shows the presence of an enhancement in the $\rho(770)$ region when an event has only one positively identified muon, leaving the other track identified as a pion. This peak is undoubtedly a $\rho(770)$, as the $\rho(770)$ rarely decays into muons[4]. The form of the Bethe-Heitler background is evident in the hatched histogram when both tracks are positively identified as muons, though the requirement of a minimum opening angle has truncated the low mass region of the Bethe-Heitler pairs. The $J/\psi(3097)$ peak is relatively immune to the identification requirements of having either one or two muons identified in the event. Those events where it was determined that there was at least one muon are shown in Figure 37. The data in this figure differ from the unhatched histogram of Figure 36 only by the bin widths. The smooth curve represents a fit to the data employing a Gaussian distribution for the $J/\psi(3097)$ together with a background composed of a Bethe-Heitler dimuon pair term plus an exponential. The results of this fit are given in Table 11.

[4]The $\rho(770) \rightarrow \mu^+\mu^-$ decay is only about 0.0046% of the total $\rho(770)$ decay which in the present data sample amounts to less than one event.

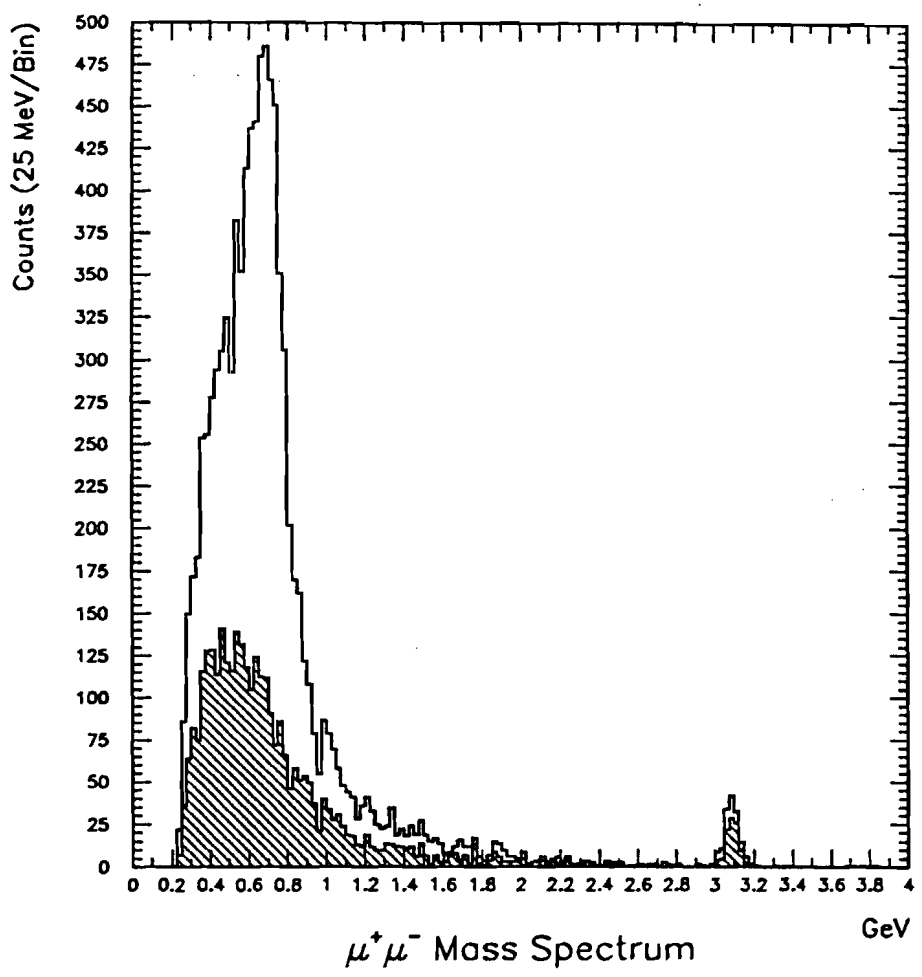

Figure 36: The $J/\psi(3097) \rightarrow \mu^+\mu^-$ mass spectrum. The unhatched histogram shows events with at least one μ positively identified, while the hatching indicates events with both tracks positively identified as μ's. A t' cut of $0.015 \leq t' \leq 0.2$ GeV^2 has been placed on these events.

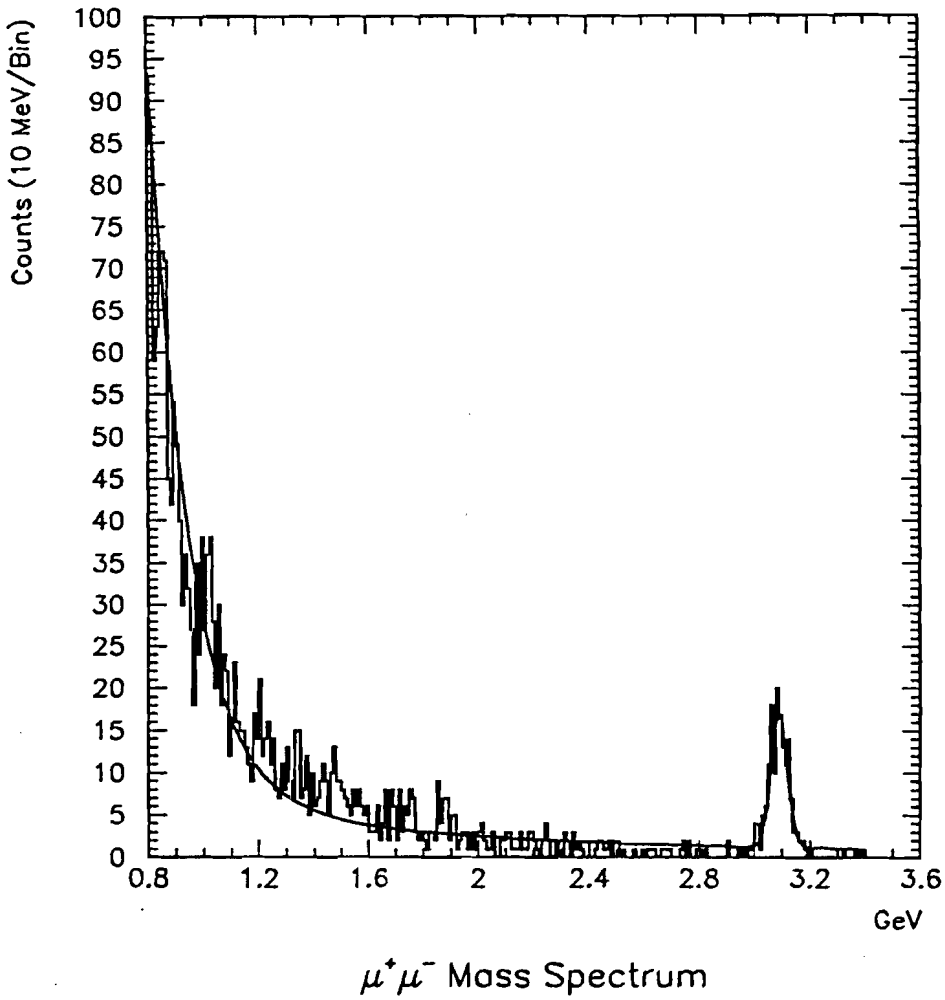

Figure 37: The $J/\psi(3097) \rightarrow \mu^+\mu^-$ mass spectrum. The fit shown is with a Gaussian superposed with the Bethe-Heitler background and a decaying exponential.

Table 11: Fit values for $J/\psi(3097) \rightarrow \mu^+\mu^-$.

$J/\psi(3097) \rightarrow \mu^+\mu^-$ Fit Parameters			
Particle	Amplitude	Mass (GeV)	Width (GeV)
$J/\psi(3097)$	1.147 ± 0.116	3.095 ± 0.003	0.029 ± 0.003

4.7 The $\pi^+\pi^-\pi^\pm$ Channel

Because this experiment consists of $> 10^8$ events, there is a reasonable chance to observe charge exchange processes even if the cross-section falls approximately as $E_\gamma^{-1.5}$, as has been found for reactions mediated by one pion exchange[17, 18, 19]. In Figure 38 we present the $\pi^+\pi^-\pi^\pm$ spectrum for all of the 3π events satisfying the criteria of Table 8. The only clearly discernible resonance present in this spectrum is the $a_2(1320)$. The smooth curve in Figure 38 represents a fit to a Breit-Wigner for the $a_2(1320)$ over a polynomial background. The fit parameters determined by this fit are given in Table 12 where it can be seen that there is tolerable agreement with the latest PDG value of 1.318 ± 0.001 GeV for the mass and 0.110 ± 0.005 GeV for the width. This $a_2(1320)$ mass does however compare well with another photoproduction experiment which found the mass of the $a_2(1320)$ to be 1.292 ± 0.002 GeV[56]. While there are possible indications for the charge exchange photoproduction of the $\pi_2(1670)$ and $a_3(2050)$, the only signal exceeding 4σ above background is that corresponding to the $a_2(1320)$.

We further attempt to quantify resonant production in this channel by plotting the neutral dipion spectrum (both combinations) in Figure 39 (triangle plot) and its projections in Figure 40. The dipion spectrum is shown again in Figure 41 when $t'_{\gamma;3\pi}$ between the interacting photon and the three pions is required to be between 0.015 and 0.2 GeV^2. The smooth curves shown in Figures 40 and 41 are fits comprised of simple Breit-Wigners over polynomial backgrounds. The results of these fits are listed in Table 13.

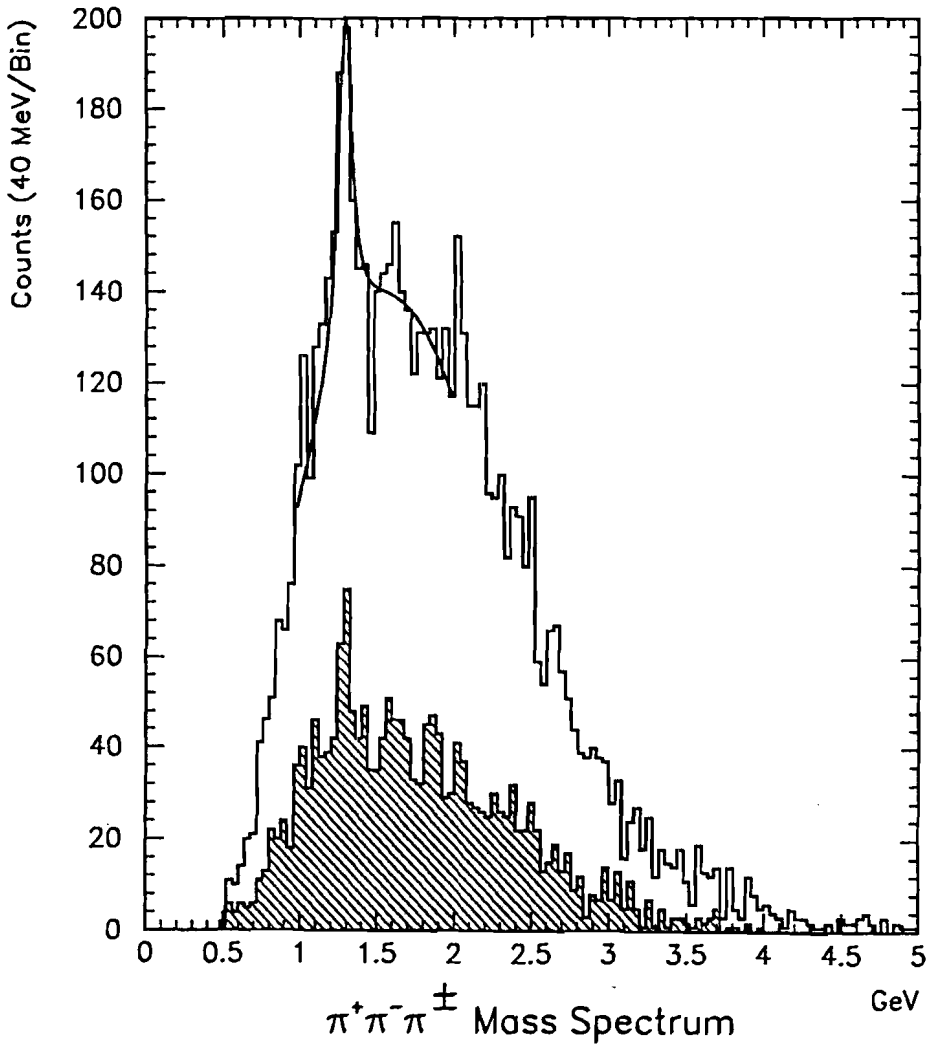

Figure 38: The $\gamma N \rightarrow \pi^+\pi^-\pi^\pm N'$ channel showing the $a_2^\pm(1320)$ enhancement. The hatched histogram corresponds to those events surviving a $0.015 \leq t' \leq 0.2$ GeV^2 cut. Note that the $a_2(1320)$ is clearly seen near 1.30 GeV.

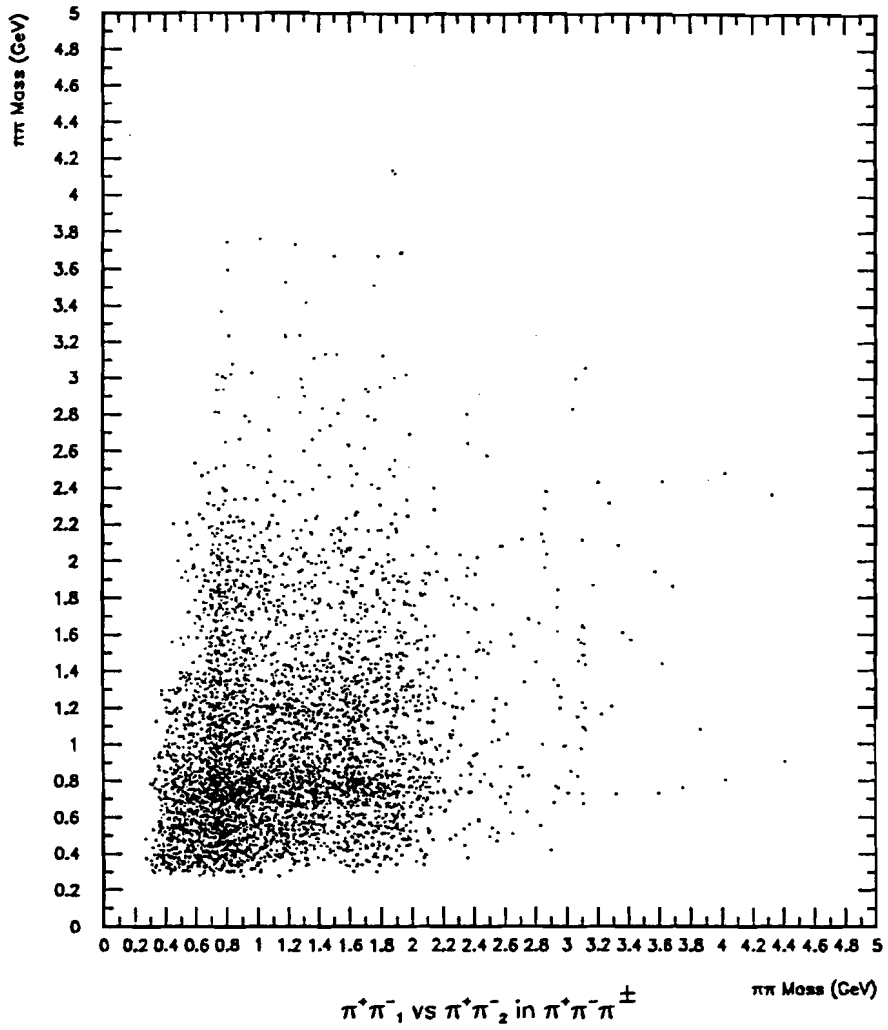

Figure 39: "Triangle" plot of $\pi^+\pi^-$ combinations. Note the presence of the $\rho(770)$, the $f_2(1270)$ and the $\rho_3(1690)$, as evident by the dark bands through these respective masses. The events from the $J/\psi(3097)$ also form a band along the 3.1 GeV bin.

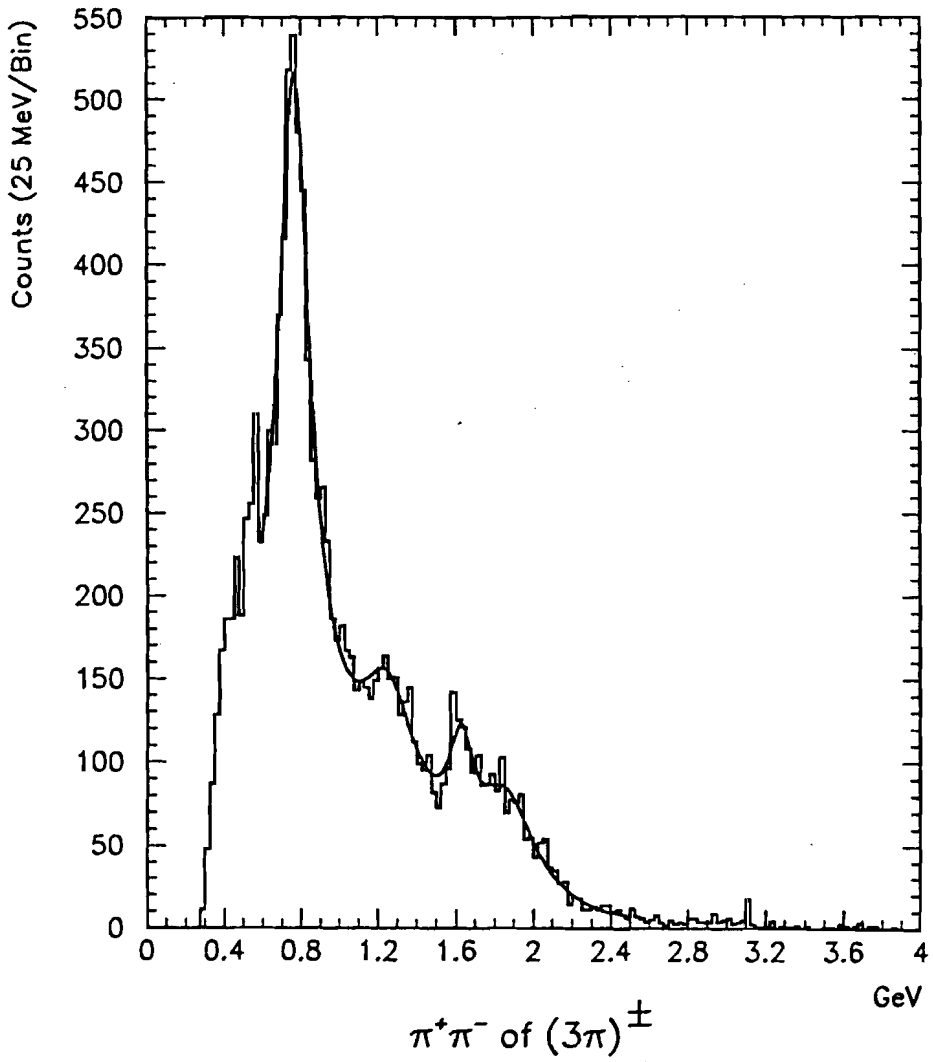

Figure 40: The neutral dipion combinations in the $\gamma N \rightarrow \pi^+\pi^-\pi^{\pm}N'$ channel.

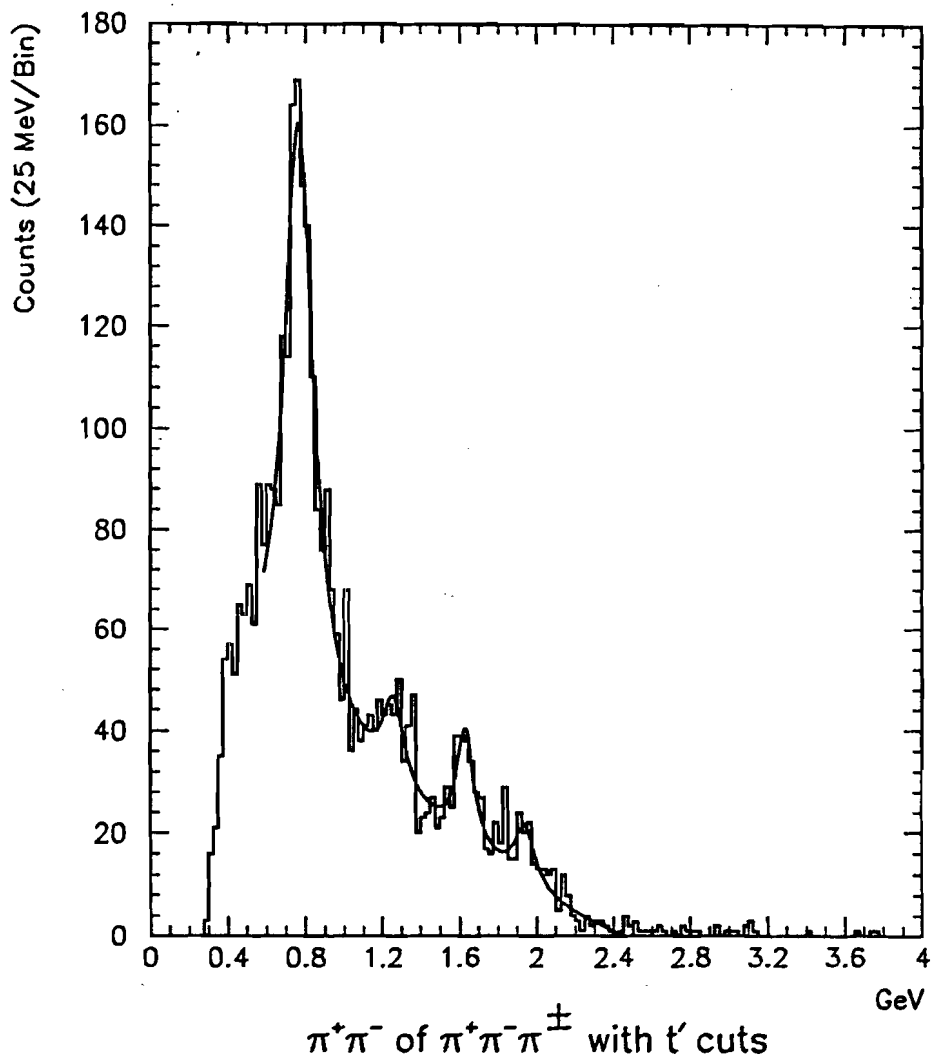

Figure 41: The neutral dipion combinations in the $\gamma N \rightarrow \pi^+\pi^-\pi^\pm N'$ channel subjected to a $0.015 \leq t'_{\gamma;3\pi} \leq 0.2$ GeV^2 cut.

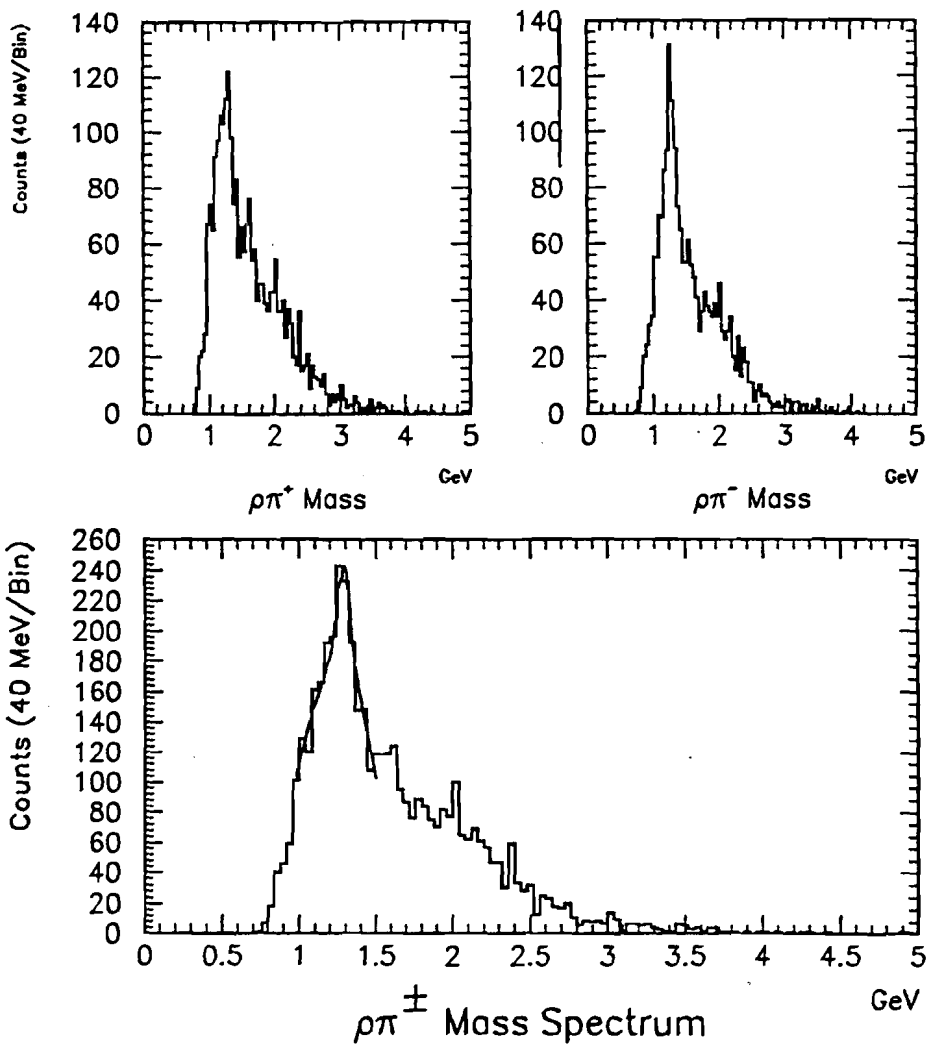

Figure 42: The $\rho(770)\pi^{\pm}$ combinations in the $\gamma N \rightarrow \pi^{+}\pi^{-}\pi^{\pm}N'$ channel. The $\rho(770)$ mass region is defined to be 0.60 GeV $\leq \rho(770) \leq$ 0.90 GeV.

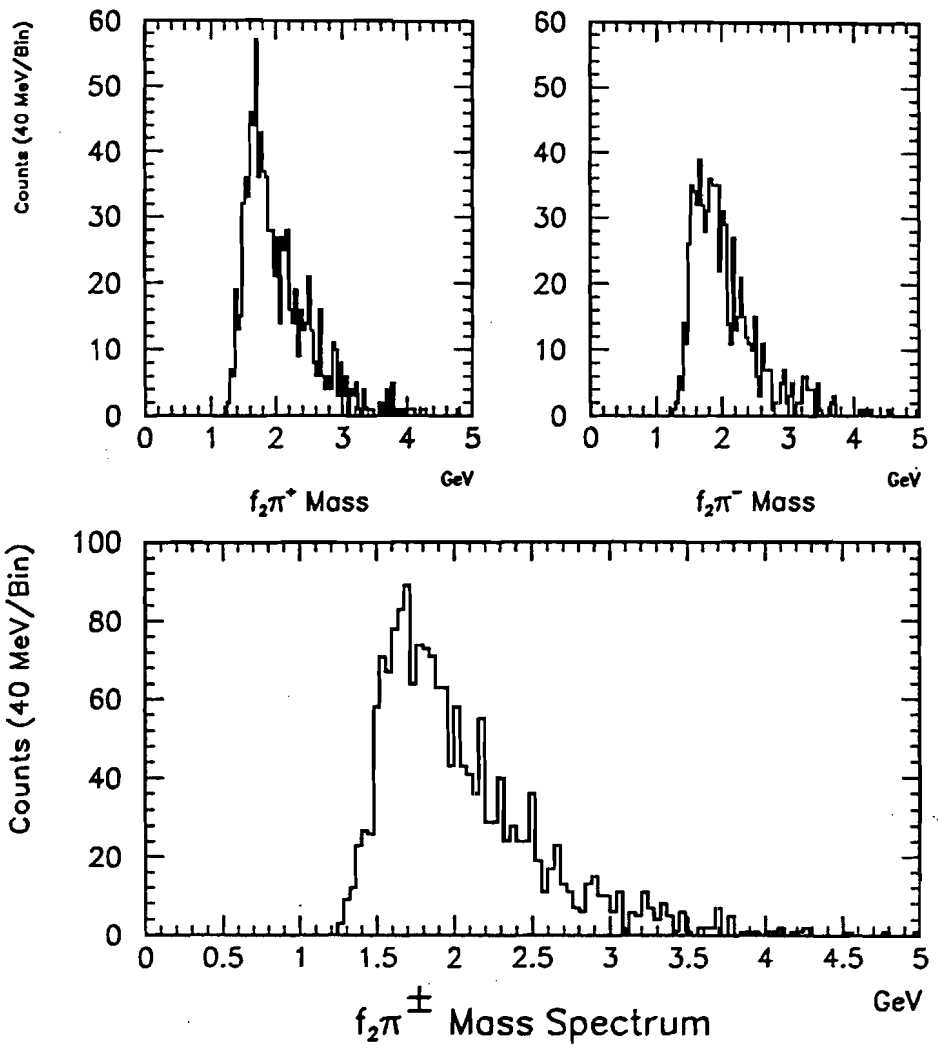

Figure 43: The $f_2(1270)\pi^\pm$ combinations in the $\gamma N \to \pi^+\pi^-\pi^\pm N'$ channel. The mass of the $f_2(1270)$ is taken to be 1.10 GeV $\leq f_2(1270) \leq$ 1.40 GeV.

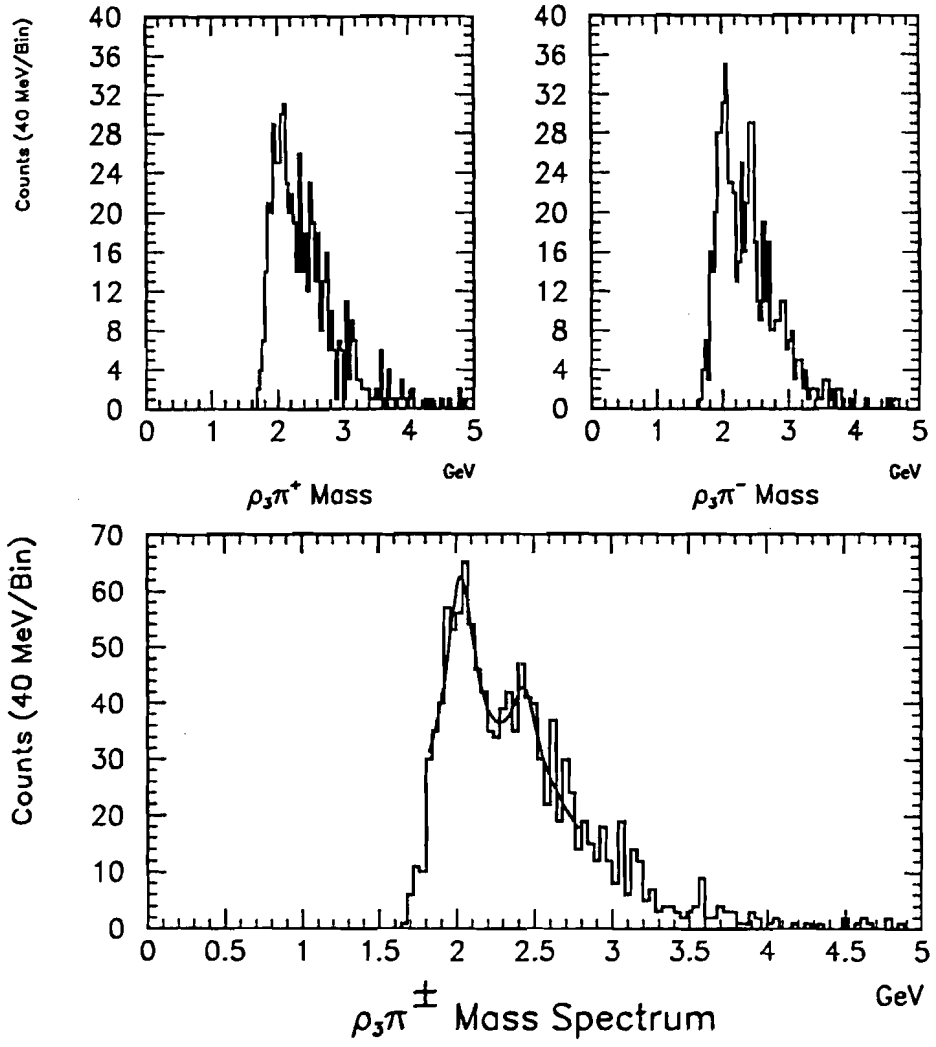

Figure 44: The $\rho_3(1690)\pi^\pm$ combinations in the $\gamma N \to \pi^+\pi^-\pi^\pm N'$ channel. The $\rho_3(1690)$ mass is taken to be 1.50 GeV $\leq \rho_3(1690) \leq$ 1.80 GeV.

Table 15: Fit results for the $\rho_3(1690)\pi^{\pm}$ spectrum before (upper) and after (lower) the $t'_{\gamma;3\pi}$ cut.

$a_3(2050) \rightarrow \rho_3(1690)\pi$ Fit Parameters			
Particle	Amplitude	Mass (GeV)	Width (GeV)
$a_3(2050)$	12.37 ± 2.35	2.029 ± 0.022	0.221 ± 0.009
Y	4.97 ± 1.55	2.438 ± 0.025	0.198 ± 0.005

$a_3(2050) \rightarrow \rho_3(1690)\pi$ Fit Parameters After The t' Cut			
Particle	Amplitude	Mass (GeV)	Width (GeV)
$a_3(2050)$	4.60 ± 1.13	2.028 ± 0.023	0.221 ± 0.003
Y	2.22 ± 0.96	2.460 ± 0.054	0.220 ± 0.015

evidence for two resonances. The data is fit accordingly with two Breit-Wigners superposed onto a polynomial background. The two resonances appear at masses of 2.029 ± 0.022 GeV and 2.438 ± 0.025 GeV with the former being reasonably identified as the $a_3(2050)$ (Table 15). This is the only state with a $\rho_3(1690)\pi$ decay mode that is listed in the PDG table[9].

The $\rho(770)\pi$, $f_2(1270)\pi$ and $\rho_3(1690)\pi$ masses are presented again in Figure 45 where each is required to have $t'_{\gamma;3\pi}$ between 0.015 and 0.2 GeV^2. The $\rho(770)\pi$ and $\rho_3(1690)\pi$ spectra are fit as in Figures 42 and 44, and the results are given in Tables 14 and 15. The masses and widths for the $a_2(1320)$, $a_3(2050)$ and the state at 2.44 GeV remain consistent with those obtained from data not subjected to the t' constraint.

The $J/\psi(3097)\pi^{\pm}$ Events

The appearance of the $J/\psi(3097)$ in the neutral dipion spectrum of $\pi^+\pi^-\pi^{\pm}$ events was not expected. It is another example of the failure of our apparatus to resolve the pion-muon ambiguity whereby dimuon events appear in a dipion mass spectrum. In Figure 46 we plot the $J/\psi(3097)\pi^{\pm}$ spectrum. To do this, the $\pi^+\pi^-$

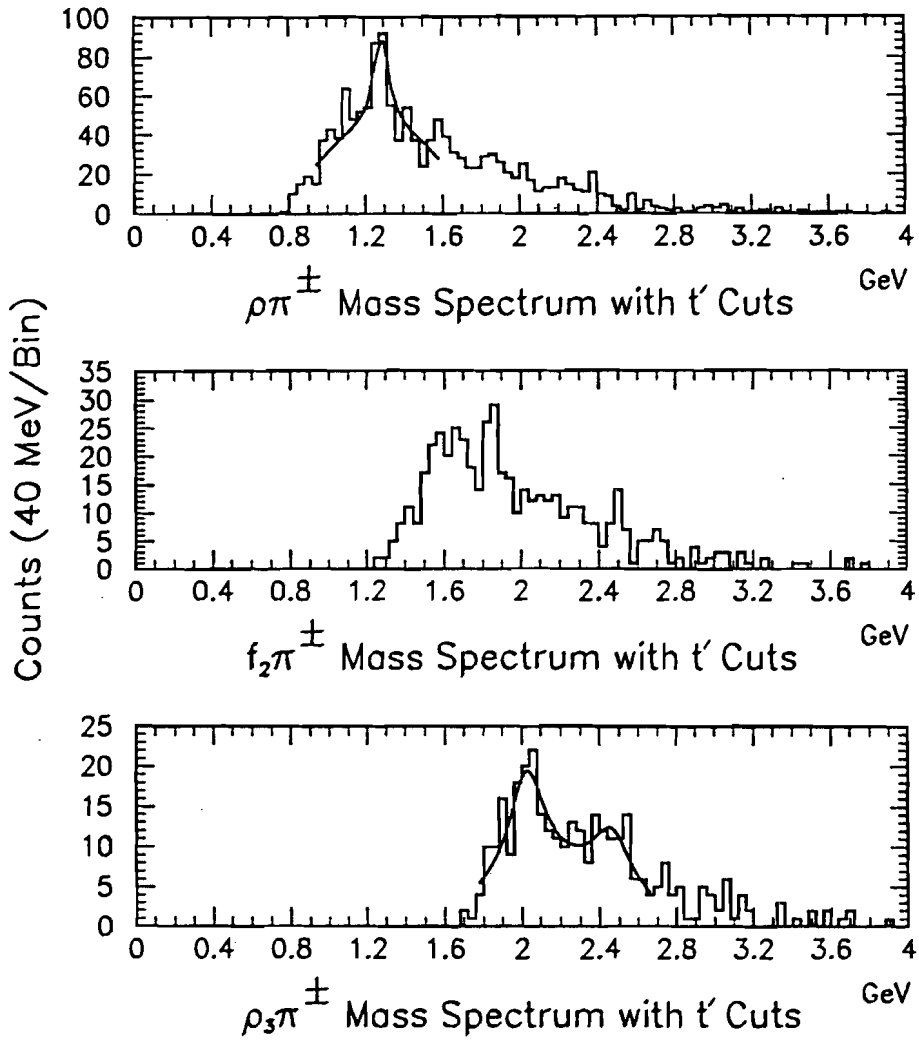

Figure 45: The $\rho(770)\pi^{\pm}$, $f_2(1270)\pi^{\pm}$ and $\rho_3(1690)\pi^{\pm}$ combinations with a $0.015 \leq t' \leq 0.2$ GeV^2 cut applied.

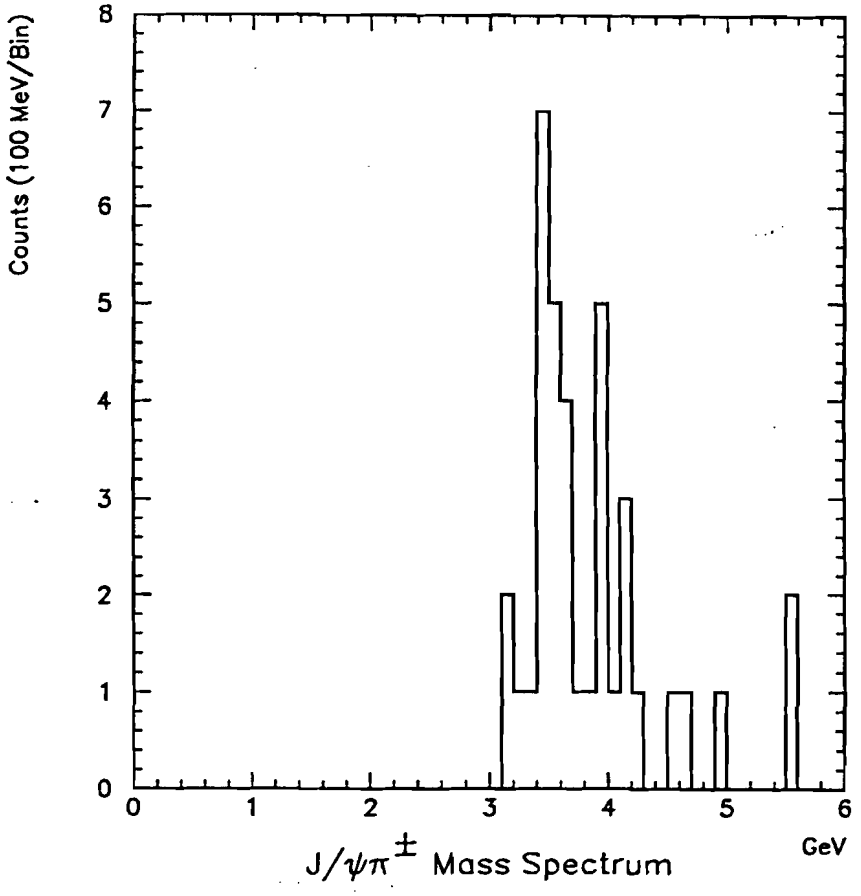

Figure 46: The $J/\psi(3097)\pi^{\pm}$ combinations.

combination with an invariant mass between 3.0 and 3.2 GeV is reconstructed as a $\mu^+\mu^-$ combination with the bachelor pion retaining the pion rest mass (in order to conserve lepton number). The spectrum, though statistically weak, contains a low mass enhancement at $\sim$ 3.6 GeV. A Gaussian fit yields 3.558 ± 0.073 GeV with a width of 0.270 ± 0.270 GeV. If these events were due to a double peripheral production mechanism, the spectrum would be expected to be nearly flat in this mass region. Monte Carlo calculations show that the background from $J/\psi(3097)$ events with an associated e^+e^- pair would be expected to produce at most 3 events which simulate $J/\psi(3097)\pi^\pm$ whereas we observe 41 such events. Also, the shape of this Monte Carlo spectra peaks at a slightly lower value than the real data. The $J/\psi(3097)\pi^\pm$ events possibly represent a new resonance. The PDG tables have no confirmed isovector states which decay into (J/ψ + anything).

Chapter 5

Monte Carlo and Detector Simulation

5.1 The ROGUE Monte Carlo

A detailed Monte Carlo program, Super Rogue (SROGUE), has been developed by the E687 experimenters to analyze geometrical, triggering, and reconstruction efficiencies. The initial electron beam and multibremsstrahlung photon production from the lead radiator are treated in the code system called GENERIC. The interacting photon and the particles of interest are generated in GENERIC. GENERIC then passes the information on to another code system, ROGUE. ROGUE produces the final particle products and transports them through the detector. The output from ROGUE is in the form of raw data, and adheres to the triggering conditions of the various run periods. Finally, the reconstruction and user codes are applied to the Monte Carlo data.

Event Generation and Decay

GENERIC simulates the incident electron beam before it passes through the lead radiator. The energy of the beam is determined from real electron calibration

runs for the BGM/BCAL and is parameterized to follow these distributions. The bremsstrahlung photon is then passed through the lead radiator following a mean free path. The electron is also allowed to multiple scatter in the radiator. The produced photons (> 5 GeV) are then tested for conversion. The probability of the photon generating an event inside the target is determined via a step function over the target length, so that proper targeting is achieved. The recoil energy of the electron is simulated in the RESH, and any additional energy in the BGM is tracked and accumulated. Only a single photon produced from the initial electron is used as an event generator.

Vector meson photoproduction is initiated with an $e^{-10|t'|}$ distribution in the center of mass frame[1]. The vector mesons are assumed to decay with a $\sin^2\theta$ distribution in their helicity frame. This corresponds to assuming the vector mesons are created with the helicity of the incident photon. The mass is generated either to follow a nonrelativistic Breit-Wigner or the Söding description of the $\rho(770)$ discussed earlier in the Theory section. This uniquely determines the momentum distribution of the meson and the recoil nucleon.

The efficiency of the detector for a particular variable, such as the resolution of an angular distribution, requires the variable to be generated without any functional form. Thus the cosine of the helicity angle θ is generated with a flat distribution rather than the SCHC form $[\sin^2\theta = 1 - \cos^2\theta]$ for a 1^- vector meson. Likewise, the mass is generated with a flat distribution rather than a Breit-Wigner, or with the Söding description of the photoproduced $\rho(770)$.

GENERIC can include additional "embedded" pairs, which correspond to pair production from a bremsstrahlung photon *not* associated with the interaction. This is generally considered to be about a 17% effect[50]. The vertex position is randomized inside the target volume and limited by the spread of the photon beam.

[1]This t' distribution was chosen because it is reasonably consistent with much of the raw experimental data in this work and because it is consistent with much of the previous experimental data.

ROGUE and the Detector

ROGUE traces each final state particle through the detector and examines specific "natural" stopping points, such as detector apertures, wire hits in PWC's, and places where multiple scattering is expected to occur. The charged particles are tracked throughout the detector based upon one of four magnetic configurations. These essentially correspond to different mappings of the magnetic field. Neutral particles are likewise followed, allowing interaction with various components of the detector.

ROGUE transports each particle through the various devices in the detector and generates an appropriate response as if the device were actually monitoring the particle. In the SSD's the simulation is rather straightforward. A hit is recorded where the track intersects the microstrip. When a track bisects several cells, a simple geometric model based upon an ionization cloud is projected around the track. This allows for charge sharing and emulates the silicon strip data. Extra hits adhering to a Gaussian distribution are then added in to simulate noise.

The PWC simulation is somewhat similar to that of the SSD. A particle trajectory close to a wire creates a hit in that wire. About 5% of the hits involve an "adjacency" hit, where multiple wire hits are recorded. This simulates the actual data. Smearing is applied to the trajectory according to the resolution of the PWC's. The efficiencies of the various PWC planes varied over the 1990-1991 runs and with each other, and hits were randomly removed in order to model this distribution.

The Čerenkov counters were simulated in the reverse order of the data reconstruction process. The charged tracks are followed through the detectors, and light is emitted according to the particles' mean free path. These light cones are then allowed to transverse the Čerenkov detectors, and the light is reflected into photomultipliers. The inefficiences due to transparency of the Čerenkov counters, mirror reflectivity, and photocathode efficiency were taken into account. No corrections are made to simulate noise in the Čerenkov detectors.

Triggering Efficiencies over Run Periods

Finally, the triggering setups of the 1990-1991 runs are simulated for the various run periods. Either individual run periods or the entire run of E687 could be modeled, and as such no special attention to individual trigger periods were needed.

5.2 ROGUE Results

The results of GENERIC for the beam generation are summarized in Figure 47. This figure shows an arbitrary number of accepted Monte Carlo events. The Monte Carlo data may be compared with the real data in Figure 24. The electron beam is passed into a lead radiator to simulate the photon flux and then the fluxes for the individual decay channels are determined with the BGM run as a scalar or counter. Every time neutral energy greater than 133 GeV reaches the BGM, a scalar is increased. This value, shown in Figure 48 is used to scale the photon flux for the cross-section calculations. The ratio of Monte Carlo generated events divided by the number of BGM scalars gives the ratio of interactions to the total photon flux[46, 52].

$\pi^+\pi^-$ Corrections from the Simulation

The acceptance curves for mass of the $\pi^+\pi^-$ channel are shown in Figure 49, where the number of reconstructed events are divided by the number of Monte Carlo generated events. This figure shows the efficiency after all cuts have been used.

The $\phi(1020) \rightarrow K^+K^-$ Channel

The mass acceptance for the K^+K^- channel is shown in Figure 50. The detection efficiency of the K^+K^- channel is roughly twice that of the $\pi^+\pi^-$ channel. This is expected, as the E687 triggers are generally selected to maximize the efficiency for

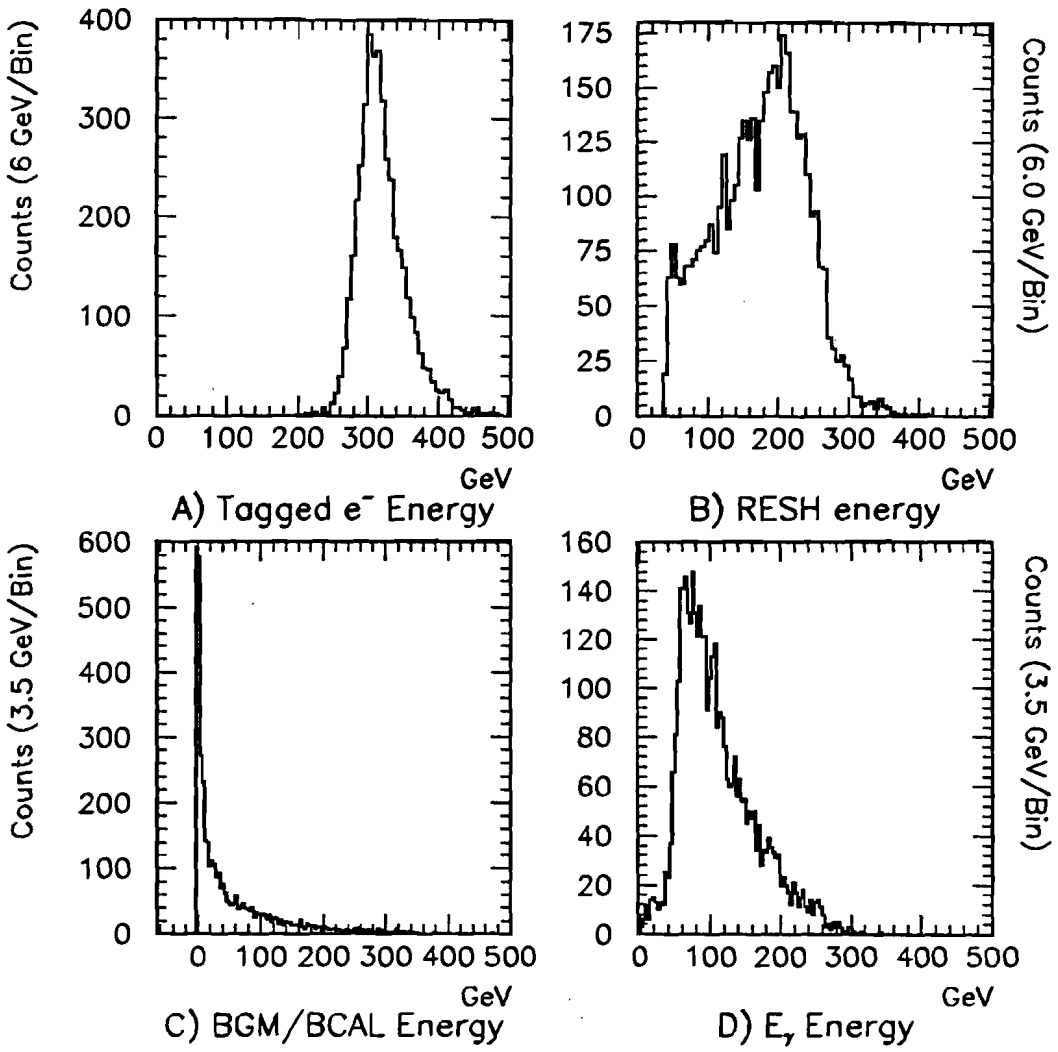

Figure 47: The SROGUE results showing the derivation of the photon energy. A) The tagged e^- energy. B) The RESH energy. C) The BGM energy. D) The interacting photon energy.

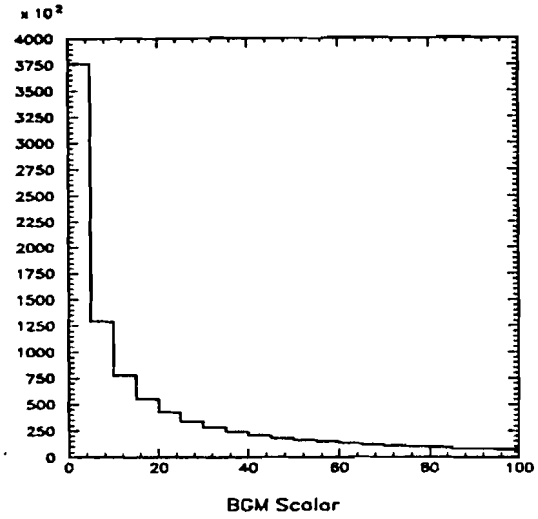

Figure 48: The SROGUE results showing the photon flux reaching the BGM.

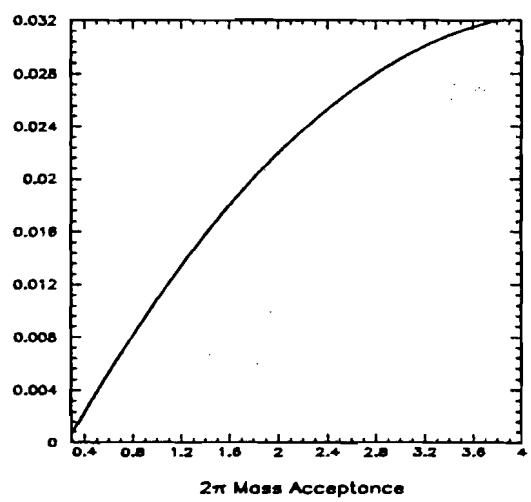

Figure 49: The mass acceptance curve for the 2π channel. These are the events that have passed all the analysis cuts, including the $0.015 \leq t' \leq 0.2\,\mathrm{GeV}^2$ cut.

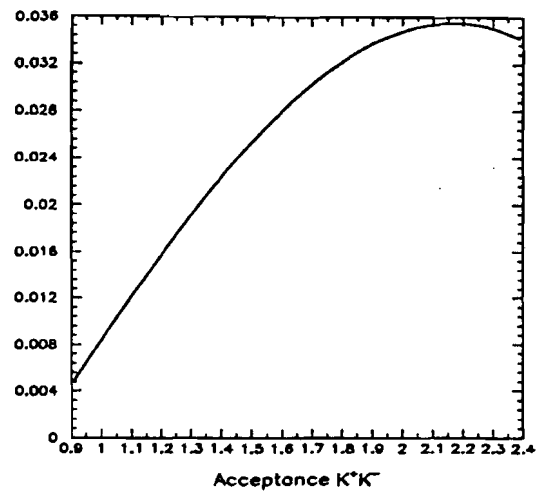

Figure 50: The Monte Carlo acceptance for the $\phi(1020) \rightarrow K^+K^-$ channel.

detecting either charm particles (massive events) or large transverse momentum events.

The $J/\psi(3097) \rightarrow \mu^+\mu^-$ Channel

The $J/\psi(3097)$ Monte Carlo presents some additional considerations. The cut requiring 5 GeV of energy in the HC could eliminate several examples of the $J/\psi(3097)\,(\mu^+\mu^-)$ in our sample. The HC response was modeled in the Monte Carlo, and the results along with the HC and CHC energies from real data are shown in Figure 51. The deposited energy follows a Landau distribution, as expected for a Minimum Ionizing Particle (MIP). The 5 GeV hadron energy cut corresponds to a 28.7% cut on the μ tracks in the $J/\psi(3097)$ mass region (3.0 to 3.2 GeV). It should be noted that because of the π-μ ambiguity the data exhibit a smeared distribution (some of these events contain π's that have interacted in the hadron calorimeter).

Examination of the data from the $\pi^+\pi^-$ mode shows a very large $J/\psi(3097)$

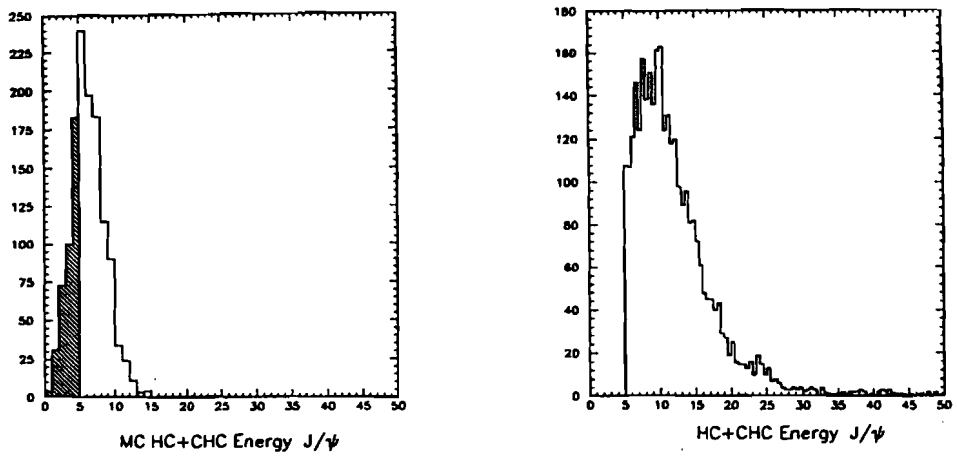

Figure 51: The HC and CHC energy response for the μ's passing through those detectors. The histogram on the left is from the Monte Carlo; the shaded region indicates those events having an energy less than 5 GeV. The histogram on the right is the HC and CHC energy from the data.

peak, which must necessarily be due to $\mu^+\mu^-$ decays[2]. Eliminating any event with one or more positively identified μ leaves roughly 40% of the $J/\psi(3097)$ sample. Hence, μ identification is about 60% efficient. In addition, the Čerenkov detectors are used to select π-consistent tracks. This adds an additional 5% inefficiency due to misidentification of muons as electrons, which are removed from the sample.

The Charge Exchange $\pi^+\pi^-\pi^\pm$ Channel

The charge exchange processes of the reaction $\gamma N \rightarrow (\pi^+\pi^-\pi^\pm)N'$ were also modeled with ROGUE. The results are shown in Figure 52. An interesting result from the Monte Carlo shows that $\pi^+\pi^-\pi^-$ generated events reconstruct approximately 36.3% of the events as $\pi^+\pi^-\pi^+$ events, and vice-versa. This result is presumably due to one track being produced with a small enough curvature that the reconstruction process cannot distinguish the sign of the charge.

[2]The $\pi^+\pi^-$ decay mode of the $J/\psi(3097)$ is 0.0147%, whereas the $\mu^+\mu-$ mode is 5.97%.

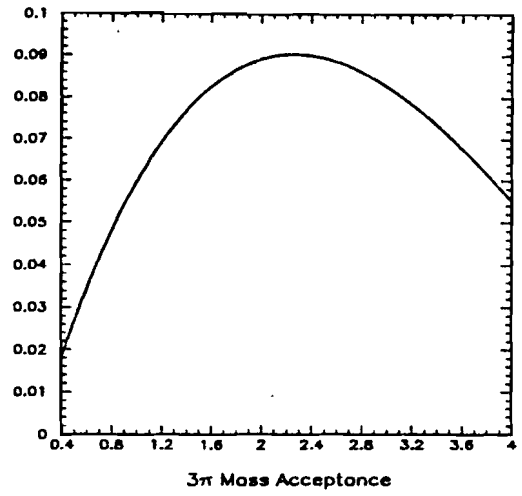

Figure 52: The mass acceptance curve for the 3π channels. The curve shows the efficiency of the 3π events passing all analysis cuts.

The Charge Exchange $J/\psi(3097)\pi^{\pm}$ Channel

A source of background for the $J/\psi(3097)\pi^{\pm}$ events becomes evident when the Monte Carlo is run for diffractive $J/\psi(3097)$ production. The $J/\psi(3097)\pi^{\pm}$ events appear when the diffractive $J/\psi(3097)$ is constructed with embedded e^+e^- pairs[3] and the detector reconstructs the electron pair as a single track. The results of $J/\psi(3097)$ Monte Carlo are shown in Figure 53 where the mass of the $J/\psi(3097)$ is reconstructed for events with only two tracks. The small fraction of events that have been reconstructed with 3 PWC tracks are also shown in Figure 53. There exists some similarity in the shape of this $J/\psi(3097)\pi$ spectra with the one presented previously in Figure 46. However, the Monte Carlo generated $[J/\psi+(e^+e^-)]$ events peak at a lower mass than do the real data. Furthermore, the misidentified $J/\psi(3097)\pi^{\pm}$ events generated from $J/\psi(3097)$ production are completely removed by the requirement that events have equal number of SSD and PWC linked tracks.

[3]Recall that these are the lepton pairs created in the coloumbic field of the target.

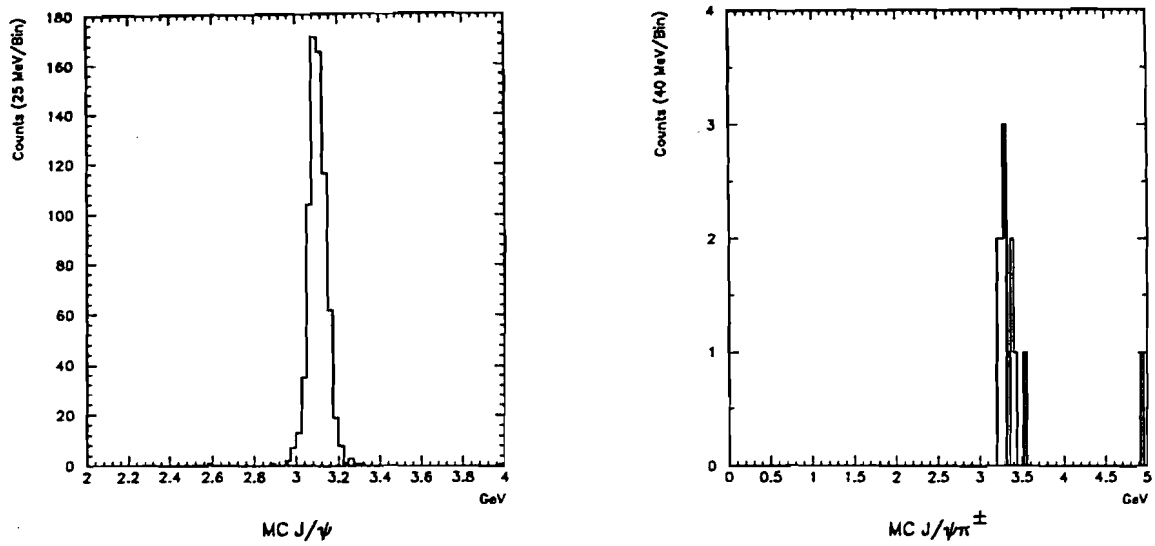

Figure 53: The diffractive $J/\psi(3097)$ (left) and $J/\psi(3097)\pi^{\pm}$ (right) events from the Monte Carlo generation of diffractive $J/\psi(3097)$ events with embedded electron pairs.

Since this requirement is used in the analysis of the real data, it is unlikely that the $J/\psi(3097)\pi^{\pm}$ data are due to "embedded pair" events.

Chapter 6

Yields and Cross-Sections

Total cross-sections in E687 are determined primarily with the assistance of Monte Carlo calculations. These Monte Carlo calculations are needed to determine the total photon flux. The cross-section is:

$$\sigma = \left[\frac{N_{\text{Meson}}}{N_\gamma \cdot A_{\text{Channel}} \cdot \text{BR}}\right]\left[\frac{1}{N_A(\rho_{\text{Be}}/A_{\text{Be}})\,(\epsilon_{\text{target}} \cdot d)\,\tau_{Live}}\right] \tag{24}$$

Individual cross-sections are primarily dependent upon the first ratio, which includes the number of mesons created (N_{Meson}), the photon flux (N_γ), and the acceptance of the detector for a given channel (A) times the branching ratio (BR) into that channel. The second term of the equation gives the number of scattering centers. The terms employed are:

- N_A = Avogadro's Number = 6.022×10^{23}/mole;
- $\rho_{\text{Be}}/A_{\text{Be}}$ = density of Be = (1.898 gm/cm^3)/(9.01 gm/mole);
- $\epsilon_{\text{target}} \cdot d$ = Effective target length = 0.4702×4.4014 cm (the targeting efficiency was determined from the Monte Carlo and is the ratio of accepted events in the target / total accepted events);
- τ_{Live} = Average live-time of the detector, taken as 71.5%[46, 52];

so that the cross-section becomes

$$\sigma = 5.0835 \times 10^6 \left[\frac{N_{\text{Meson}}}{N_\gamma \cdot A_{\text{Channel}} \cdot \text{BR}} \right] \mu\text{b}. \tag{25}$$

The ratio $N_{\text{Meson}}/N_\gamma$ is calculated from a Monte Carlo procedure as mentioned on the previous page. The cross-section calculations include the following systematic errors on the following quantities (which add in quadrature):

- The FLUX of the photons is estimated to be uncertain by 5%.
- The PHOTON SPECTRUM is estimated to be known to within 5% in the Monte Carlo calculations. The true photon spectrum is less well-known, as both the direction of the photon and the RESH response to the radiated electron are not accurately known. An additional 15% error is assumed. Errors in the photon spectrum will have their greatest impact in the calculation of momentum transfer (t').
- The RECONSTRUCTION PROCESS contributes an estimated additional 20% error. This error also includes systematic errors from the Čerenkov detectors. Errors in μ identification contribute an additional 10-15% error, especially in the lower mass region where the Bethe-Heitler background is significant.
- The overall systematic error obtained by adding the individual systematic errors in quadrature is estimated to be 28.83%.

Additional corrections to the $J/\psi(3097) \rightarrow \mu^+\mu^-$ events must also be applied. The requirement that 5 GeV be deposited in the hadron calorimeter rejects 28.1% of the real μ events which must be taken into account. The Čerenkov misidentification of the muon as an electron contributes another 5%.

The vector mesons are modeled in the Monte Carlo to be produced off the entire beryllium nucleus. The conversion of the cross-section per nucleus to cross-section per nucleon is given by the formula[45, 46, 52, 57]:

$$\sigma_{\text{nucleon}} = \sigma_{\text{nucleus}} \left(\frac{1}{A_{\text{Be}}} \right)^{0.94} \tag{26}$$

Table 16: Acceptance corrected yields and cross-sections for various mesons. The upper table lists the yields while the lower shows cross-sections.

Acceptance Corrected Yields			
Particle	Acceptance	Yields	Corrected Yields
$\rho(770)$	0.0035	12,296.8 $\pm$147.2	3,513,371.4 $\pm$42,057.1
$\phi(1020)$	0.0058	425.4 $\pm$ 23.7	73,344.8 $\pm$ 4,086.2
$\rho'(1600)$	0.0181	170.7 $\pm$ 40.8	9,430.8 $\pm$ 4,086.2
$J/\psi(3097)$	0.0124	120.7 $\pm$ 14.4	9,733.8 $\pm$ 1,161.3
$a_2(1320)$	0.072	188.3 $\pm$ 29.8	2,615.3 $\pm$ 413.9

Cross-Sections per Nucleon		
Particle	N_γ	$\sigma \pm$ statistical $\pm$ systematic
$\rho(770)$	1.993×10^{11}	$11.356 \pm 0.136 \pm 3.305\,\mu$b
$\phi(1020)$	1.379×10^{11}	$0.698 \pm 0.038 \pm 0.203\,\mu$b
$J/\psi(3097)$	1.017×10^{13}	$10.31 \pm 1.23 \pm 3.04$ nb
$\rho'(1600)_{\pi^+\pi^-}$	—	$30.48 \pm 15.91\,\mu$b
$a_2^{\pm}(1320)_{\rho\pi^\pm}$	—	8.45 ± 2.80 nb

where A_{Be} is the atomic number of beryllium.

Table 16 lists yields with the errors from the fits and the cross-sections per nucleon with statistical and systematic errors. The listed cross-sections are integrated over all energy and momenta. The cross-sections for the $\rho'(1600)$ and the $a_2(1320)$ are found from the ratio of acceptance corrected yields compared to the acceptance corrected yield of the $\rho(770)$ multiplied by the $\rho(770)$ cross-section.

The cross-section of the $a_2(1320)$ provides a test of pion mediated charge exchange. The $a_2(1320)$ may be compared to previous $a_2(1320)$ photoproduction cross-sections by examining the relationship between the interaction energy and the cross-section. OPE predicts an energy dependence of E_γ^{-n}, where n is between 1 and 2. The only other previous photoproduction measurements of direct $a_2(1320)$ production come from Eisenberg *et al.*[58] who find $\sigma_{a_2} = 2.6 \pm 0.6\,\mu$b at 4.8 GeV,

and from Condo *et al.*[18] who find $\sigma_{a_2} = 0.29 \pm 0.06\,\mu$b at 19.5 GeV. Comparing these data gives $n = 1.57 \pm 0.22$[18]. For this experiment we are unable to separate the reactions γp $\rightarrow$ n$a_2^+(1320)$ from γp $\rightarrow \Delta^- a_2^+(1320)$ so that the appropriate cross-section comparisons involve the sum of $a_2^{\pm}(1320)$ production with either nucleon or Δ recoil. This results in an increase in the 19.5 GeV $a_2(1320)$ cross-section to $0.63 \pm 0.08\,\mu$b[17]. For this experiment, correction for unseen decay modes increases the $a_2(1320)$ cross-section to $0.032 \pm 0.011\,\mu$b at 130.7 GeV. These results give an n dependence of 1.56 ± 0.26 which is quite consistent with an OPE hypothesis.

Chapter 7

Concluding Remarks

Diffractive Photoproduction

We have studied the photoproduction of the neutral vector mesons $\rho(770)$, $\rho'(1600)$, $\phi(1020)$ and $J/\psi(3097)$ through their decays into two charged particles. Aside from the $\rho'(1600)$ which was observed as an $\sim 3\sigma$ effect, the $\rho(770)$, $\phi(1020)$ and $J/\psi(3097)$ were all observed as $> 10\sigma$ signals. The latter states were all observed with a mass and width consistent with the values presented by the Particle Data Group. The mass of the $\rho'(1600)$ was found to be marginally less than previous determinations, albeit not sufficiently so as to warrant discussion. The production cross-sections were also found to be consistent with other measurements, although the large systematic errors associated with our detector do not permit great accuracy here.

Charge Exchange Photoproduction

The $\pi^+\pi^-\pi^\pm$ spectrum contained evidence, at the 5σ level, for the photoproduction of the $a_2^\pm(1320)$. The most interesting feature of this channel is the neutral dipion spectrum. The $\rho(770)$, $f_2(1270)$ and $\rho_3(1690)$ all appear as at least 4σ enhancements. Furthermore the data in the $\rho(770)$ region is well described by a fit employing a Breit-Wigner superimposed on a polynomial background. The

fact that such a description is possible (without resort to the Söding production mechanism) is a strong indication that these $\rho(770)$ mesons are the decay product of higher mass states. The presence of the $f_2(1270)$ is also suggestive of being the decay product of a higher mass meson. The $f_2(1270)$ has never been observed as a peripheral photoproduction product. Similarly, even though the $\rho_3(1690)$ could be photoproduced either diffractively or by OPE, none of the previous high energy experiments studying either of the reactions $\gamma p \rightarrow p\pi^+\pi^-$ or $\gamma p \rightarrow p\pi^+\pi^-\pi^+\pi^-$ has ever claimed an unequivocal $\rho_3(1690)$ signal. It is, therefore, likely that the $\rho(770)$, $f_2(1270)$ and $\rho_3(1690)$ seen in this channel are all the decay products of more massive states. While no $f_2(1270)\pi^\pm$ state could be clearly delineated, the $\rho(770)\pi^\pm$ spectrum revealed the $a_2(1320)$, and the $\rho_3(1690)\pi^\pm$ spectrum indicated the photoproduction of a state at 2.03 GeV - presumably the state previously named $a_3(2050)$.

The dipion spectrum discussed above also contained evidence for $J/\psi(3097)$ production. These events, which are really misidentified $\mu^+\mu^-$ decays of the $J/\psi(3097)$, cannot be explained by either a double peripheral process or by misidentified events which simulate $J/\psi(3097)\pi$ production. Close and Lipkin[11] have predicted an exotic four quark state that would decay into $J/\psi(3097)\pi$. The production of a $q\bar{q}$ meson that decays into $(J/\psi(3097) + \pi)$ requires the existence of an OZI forbidden transition. From the fact that no independent evidence exists for a $q\bar{q}$ state in this mass region and the expectation that if there were such a state, its decay would be dominated by OZI allowed transitions, we conclude that our data is strongly suggestive of the existence of a four quark state with a $c\bar{c}$ and a $(u\bar{u}, d\bar{d})$ mixture.

BIBLIOGRAPHY

Bibliography

[1] J. Chadwick . "Possible Existence of a Neutron." *Nature*, **129**, February 1932.

[2] C. Anderson. "The Positive Electron." *Phys. Rev*, **43**, 1933.

[3] E. Fermi. "Versuch einen Theorie der β-Strahlen I." *Z. Physik*, **88**, 1934.

[4] S.H. Neddermeyer and C.D. Anderson. "Note on the Nature of Cosmic Ray Particles." *Phys. Rev.*, **52**, 1937.

[5] J.C. Street and E.C. Stevenson. "New Evidence for the Existence of a Particle of Mass Intermediate Between the Proton and Electron." *Phys. Rev.*, **52**, 1937.

[6] E.D. Bloom, *et al.* "High Energy Inelastic e-p Scattering at 6° and 10°." *Phys. Rev. Lett.*, **23**(16), October 1969.

[7] M. Breidenbach, *et al.* "Observed Behavior of Highly Inelastic Electron-Proton Scattering." *Phys. Rev. Lett.*, **23**(16), October 1969.

[8] T. Eichten *et al.* "Measurement of the Neutrino-Nucleon and Antineutrino-Nucleon Total Cross Sections." *Phys. Letts.*, **46B**(2), September 1973.

[9] The Particle Data Group. "Review of Particle Properties." *Phys. Rev.*, **D45**(11), June 1992.

[10] T. Barnes. "(A Few) Open Questions in Hadron Spectroscopy." *Invited contribution to the workshop on "Future Directions in Particle and Nuclear Physics at Multi-GeV Hadron Beam Facilities,"* Brookhaven, March 1993.

[11] F.E. Close and Harry J. Lipkin. "$\phi\pi$ Production by Photons as a Signature for Four-Quark States." *Phys. Rev. Letts.*, **41**(19), November 1978.

[12] F.E. Close. *An Introduction to Quarks and Partons.* Academic Press, San Diego, CA., 1983.

[13] M.R. Pennington. "In Search of Hadrons Beyond the Quark Model." *University of Durham Centre for Particle Theory Preprint*, DTP-90/89, September 1990.

[14] J.J. Sakuri. "Theory of Strong Interactions." *Ann. Phys.*, **11**, 1960.

[15] F.E. Low. "Model of the Bare Pomeron." *Phys. Rev.*, **D12**(1), July 1975.

[16] T.H. Bauer, *et al.* "The hadronic properties of the photon in high-energy interactions." *Rev. Mod. Phys.*, **50**(2), April 1978.

[17] G.T. Condo, *et al.* "Charge-exchange photoproduction of the $a_2(1320)$ in association with Δ^{++} at 19.3 GeV/c." *Phys. Rev.*, **D41**(11), June 1990.

[18] G.T. Condo, *et al.* "Further Results from Charge Exchange Photoproduction." *To be published.*, 1993.

[19] A.P.T Palounek. *Photoproduction of Vector Mesons at 20 GeV.* PhD thesis, Duke University, 1984. N.K. Morgan. PhD thesis, Duke University, 1984.

[20] Marc Ross and Leo Stodolsky. "Photon Dissociation Model for Vector-Meson Photoproduction." *Phys. Rev.*, **149**(4), September 1966.

[21] P. Söding. "On the Apparent Shift of the Rho Meson Mass in Photoproduction." *Phys. Lett.*, **19**(8), January 1966.

[22] J. Babcock and J. Rosner. "Radiative transitions for low-lying positive-parity mesons." *Phys. Rev.*, **D14**(5), September 1976.

[23] J. Ballam, *et al.* "Vector-Meson Production by Polarized Photons at 2.8, 4.7, and 9.3 GeV." *Phys. Rev.*, **D11**(7), June 1973.

[24] D. Aston, *et al.* "Photoproduction of K^+K^- pairs on Hydrogen at Photon Energies of 20 to 36 GeV." *Nucl. Phys.*, **B172**(1), September 1980.

[25] R. Anderson, *et al.* "Neutral-Boson Photoproduction on Hydrogen at High Energies." *Phys. Rev.*, **D1**(1), January 1970.

[26] J. Busenitz, *et al.* "High-energy photoproduction of $\pi^+\pi^-\pi^\circ$, K^+K^-, and $p\bar{p}$." *Phys. Rev.*, **D40**(1), July 1989.

[27] H.J.Behrend, *et al.* "Photoproduction of 8 GeV Rho Mesons from Nuclei." *Phys. Rev Lett.*, **24**, 1970.

[28] R.M. Egloff, *et al.* "Measurements of the Elastic ρ- and ϕ- Meson Photoproduction Cross Sections on Protons from 30 to 180 GeV." *Phys. Rev. Lett.*, **43**, September 1979.

[29] Aachen-Berlin-Bonn-Hamburg-Heidelberg-Munchen Collaboration. "Photoproduction of Meson and Baryon Resonances at Energies up to 5.8 GeV." *Phys. Rev.*, **175**, November 1968.

[30] K. Abe, *et al.* "Study of the $\rho'(1600)$ Mass Region Using $\gamma p \rightarrow \pi^+\pi^-p$ at 20 GeV." *Phys. Rev. Lett.*, **53**(8), August 1984.

[31] D. Aston, *et al.* "Photoproduction of ρ° and ω on Hydrogen at Photon Energies of 20 to 70 GeV." *Nucl. Phys.*, **B209**, 1982.

[32] D. Aston, *et al.* "Observation of the $\rho'(1600)$ in the Channel $\gamma p \rightarrow \pi^+\pi^-p$." *Phys. Lett.*, **92B(1)**, May 1980.

[33] M.S. Atiya, *et al.* "High-Energy Photoproduction of $\rho'(1600)$." *Phys. Rev. Lett.*, **43**(23), December 1979.

[34] K. Abe, *et al.* "Test of s-channel helicity conservation in inelastic ρ° diffraction in 20-GeV photoproduction." *Phys. Rev.*, **D32**(9), November 1985.

[35] G.Wolf. "On Inelastic Diffractive Rho Photoproduction and Compton Scattering." *Nuc. Phys.*, **B26**, 1971.

[36] K. Schilling, P. Seyboth and G.Wolf. "On the Analysis of Vector-Meson Production by Polarized Photons." *Nuc. Phys.*, **B15**, 1970.

[37] The E687 Collaboration. "Description and Performance of the Fermilab E687 Spectrometer." *Nucl. Inst. Methods in Physics Research*, **A320**:519–547, 1992.

[38] Y.S. Tsai and Van Whitis. "Thick target Bremsstrahlung and Target Considerations for Secondary-Particle Production by electrons." *Phys. Rev.*, **149**, September 1966.

[39] W. Nelson, H.Hirayama, and D. Rogers. "The EGS4 Code System. SLAC-Report-265." *Fermi National Accelerator Laboratory Preprint*, PM0060, December 1985.

[40] T. Handler. Preliminary BCAL Results. *Private Communication*, 1991.

[41] G. Alimonti, *et al.* "Beam Tagging Performance." *Internal E687 Memo*, 1991.

[42] G. Alimonti, *et. al.* "A Momentum Tagging System for the Wide Band e^+/e^- Beam at FNAL." *Nucl. Inst. and Meth. in Physics Research*, **A314**:411–416, 1992.

[43] S. Shukla and Z. Wu. "Preliminary Results of BGM and CHC Calibration." *Internal E687 Memo*, 1990.

[44] R. Gardner. *A Study of the Decays $D^\circ \to K^\circ_s\pi^+\pi^-$ and $D^\circ \to K^\circ_s K^+K^-$ in High Energy Photoproduction.* PhD thesis, University of Notre Dame, April 1991.

[45] R. Yoshida. *High Energy Photoproduction of the J/Psi (J/Ψ).* PhD thesis, Northwestern University, June 1990.

[46] H. Méndez. *Measurement of the J/Ψ Photoproduction Cross Section.* PhD thesis, Centro de Investigacion y de Estudios Avanzados del IPN, April 1990.

[47] J. Wiss. "The Logic Cerenkov Algorithm." *Internal E687 Memo*, 1988.

[48] S. Park, *et al.* "Performance of the Hadron Calorimeter for FNAL Eperiment E687." *Nucl. Inst. Methods in Physics Research*, **A289**:496–503, 1990.

[49] W. Johns, *et al.* "New Central Hadron Calorimeter in E687." *Internal E687 Memo*, 1990.

[50] K. Lingel. *Photoproduction of $D^{\pm}$ Mesons.* PhD thesis, University of Illinois at Urbana-Champaign, 1990.

[51] S. Park. *Photoproduction Cross-Section of the $D^{*\pm}$.* PhD thesis, Northwestern University, June 1990.

[52] D. Claes. *Measurement of the $D^{*\pm}$ Photoproduction Cross Section.* PhD thesis, Northwestern University, June 1991.

[53] M. Fausey. "CPS and the Fermilab Farms." *Fermi National Accelerator Laboratory Preprint*, FERMILAB-Conf-92/163, June 1992.

[54] R. Yoshida. "A Monte Carlo procedure for Bethe-Heitler production of dileptons with high invariant mass." *Nuc. Inst. and Meth. in Physics Research*, **A302**, 1990.

[55] A. Donnachie and H. Mirzai. "Evidence for Two $\rho'(1600)$ Resonances." *Z. Phys. C*, **33**:407–417, 1987.

[56] D. Aston, *et al.* "The Reaction $\gamma p \rightarrow p\pi^+\pi^-\pi^+\pi^-$ for Photon Energies from 25 to 75 GeV." *Nucl. Phys.*, **B189**(15), October 1981.

[57] M.D. Sokoloff, *et al.* "Experimental Study of the A Dependence of J/ψ Photoproduction." *Phys. Rev. Lett.*, **57**(24), December 1986.

[58] Y. Eisenberg, *et al.* "Study of High-Energy Photoproduction with Positron-Annihilation Radiation." *Phys. Rev.*, **D5**(1), 1972.

Vita

GAVIN REED BLACKETT was born in Knoxville, Tennessee.
At the age of six months, his family moved to Columbus, Ohio and ten years later moved again to Philadelphia, Pennsylvania. One more move placed him in Orinda, California for his high school education, where he graduated from Miramonte High School in June of 1982. He then entered into the School of Engineering at the University of California, Berkeley. Three years later he attended San Jose State University for a year in preparation to re-enter Cal as a physics major. While at Cal he was president of his fraternity ($\Delta\Upsilon$) and a member of the Skull and Keys Honor Society. He graduated from Cal in December of 1987 with an BA in Physics. In January of 1988 he began study toward his Ph.D. at the University of Tennessee, Knoxville, starting as a teaching assistant. In the fall of 1991 he began full time work on his dissertation as a research assistant for the High Energy group at the University.

Mr. Blackett is listed in *Who's Who of American Scientists and Engineers* and is a member of the American Physical Society (APS), the APS Division of Particles and Fields (DPF) and the Southeastern Section of the American Physical Society (SESAPS).